

USB LED LIGHTING TUBE

(TIUB LAMPU LED USB)

**HISAJI NODA
MUHAMMAD IKRAM MOHD RASHID
ROSMADI BIN ABDULLAH
SAIFUDIN BIN RAZALI**

**RESEARCH VOTE NO:
UIC171002**

UMP

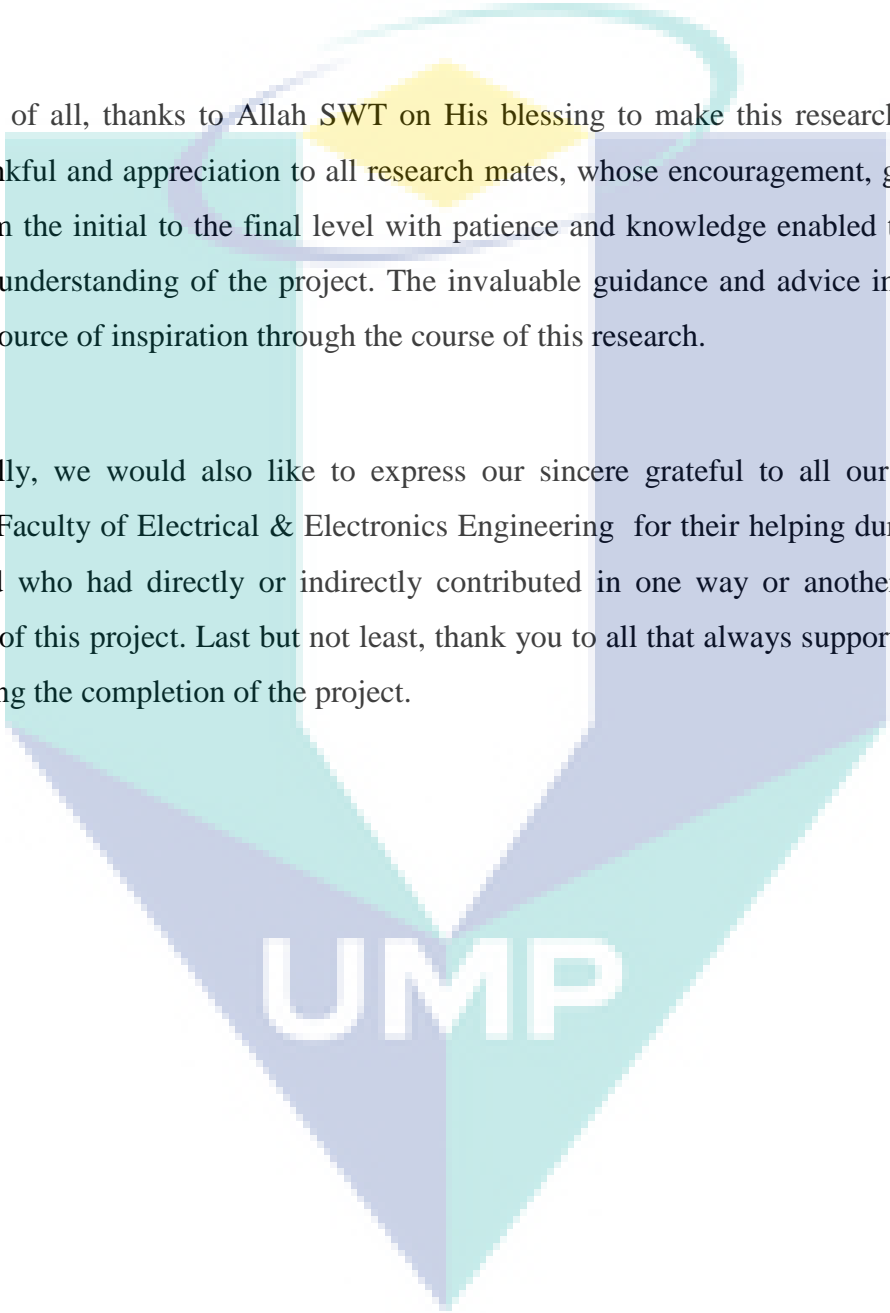
**Fakulti Kejuruteraan Elektrik & Elektronik
Universiti Malaysia Pahang**

2019

ACKNOWLEDGEMENT

First of all, thanks to Allah SWT on His blessing to make this research successful. Million thankful and appreciation to all research mates, whose encouragement, guidance and support from the initial to the final level with patience and knowledge enabled this group to develop an understanding of the project. The invaluable guidance and advice in this project has been a source of inspiration through the course of this research.

Finally, we would also like to express our sincere grateful to all our friends and students of Faculty of Electrical & Electronics Engineering for their helping during the time in need and who had directly or indirectly contributed in one way or another towards to accomplish of this project. Last but not least, thank you to all that always supported us in any respect during the completion of the project.

The logo of Ump (Universiti Malaysia Perlis) is a large, stylized shield shape. It is divided into four quadrants by a white vertical line and a white horizontal line that meet at the center. The top-left and bottom-right quadrants are light blue, while the top-right and bottom-left quadrants are light green. At the top center, there is a yellow diamond shape with a white outline. The letters 'UMP' are written in white, bold, sans-serif font across the bottom of the shield.

UMP

ABSTRACT

USB LED LIGHTING TUBE

(Keywords: LED, PWM, efficiency)

This project entails development of a power electronic controller for a LED lighting system as the low consumption lighting system. Many of today's portable electronics require backlight LED-driver solutions with the following features: direct control of current, high efficiency, PWM dimming, overvoltage protection, load disconnect, small size, and ease of use. This article discusses each of these features and how they are achieved, and conclude with a typical circuit that implements each of these features. Many portable LED applications require dimming. In applications such as LCD backlighting, dimming provides brightness and contrast adjustment. Two types of dimming are available: analog and PWM. With analog dimming, 50% brightness is achieved by applying 50% of the maximum current to the LED. Drawbacks to this method include LED color shift and the need for an analog control signal, which is not usually readily available. PWM dimming is achieved by applying full current to the LED at a reduced duty cycle. For 50% brightness, full current is applied at a 50% duty cycle. The frequency of the PWM signal must be above 100 Hz to ensure that the PWM pulsing is not visible to the human eye. The maximum PWM frequency depends upon the power-supply startup and response times. To provide the most flexibility and ease of integration, the LED driver should be able to accept PWM frequencies as high as 50 kHz.

Key researchers : Hisaji Noda, Muhammad Ikram Mohd Rashid, Rosmadi bin Abdullah,
Saifudin bin Razali

E-mail : mikram@ump.edu.my
Tel. No. : **094246063**
Vote No. : **RDU171002**

ABSTRAK

REKAAN BARU UNTUK SISTEM LAMPU LED YANG BERKECEKAPAN TINGGI

(Kata Kunci: LED, PWM, kecekapan)

Projek ini melibatkan pembangunan pengawal kuasa elektronik untuk sistem lampu LED yang menggunakan kuasa yang rendah. Kebanyakan elektronik mudah alih hari ini menggunakan lampu LED berdasarkan ciri-ciri berikut: Arus yang dapat dikawal terus, kecekapan tinggi, PWM 'dimming', perlindungan voltan, beban memutuskan sambungan, saiz kecil, dan kemudahan penggunaan. Artikel ini membincangkan setiap ciri-ciri ini dan bagaimana ia dicapai, dan membuat kesimpulan dengan litar khas yang digunakan. Banyak aplikasi mudah alih LED memerlukan 'dimming. Dalam aplikasi seperti LCD 'backlighting', 'dimming' menyediakan kecerahan dan kontras pelarasan. Dua jenis 'dimming' boleh didapati: analog dan PWM. Dengan 'dimming' analog, 50% kecerahan dicapai dengan menggunakan 50% daripada arus maksimum kepada LED. Kelemahan kaedah ini adalah kesukaran untuk membuat bacaan nilai perubahan warna LED dan keperluan untuk isyarat kawalan analog. PWM 'dimming' dicapai dengan menggunakan arus penuh kepada LED dengan mengurangkan kadar kitaran. Untuk kecerahan 50%, arus penuh digunakan pada kitaran 50%. Kekerapan isyarat PWM mestilah melebihi 100 Hz untuk memastikan detik PWM tidak boleh dilihat dengan mata. Kekerapan PWM maksimum bergantung kepada permulaan kuasa-bekalan dan tindak balas masa. Memberi fleksibiliti yang paling dan memudahkan integrasi, pemandu LED akan dapat menerima frekuensi PWM setinggi 50 kHz.

Key researchers : Muhammad Ikram Mohd Rashid, Suliana binti Ab Ghani,

PM Dr. Kamarul Hawari bin Ghazali

E-mail : mikram@ump.edu.my

Tel. No. : 094246063

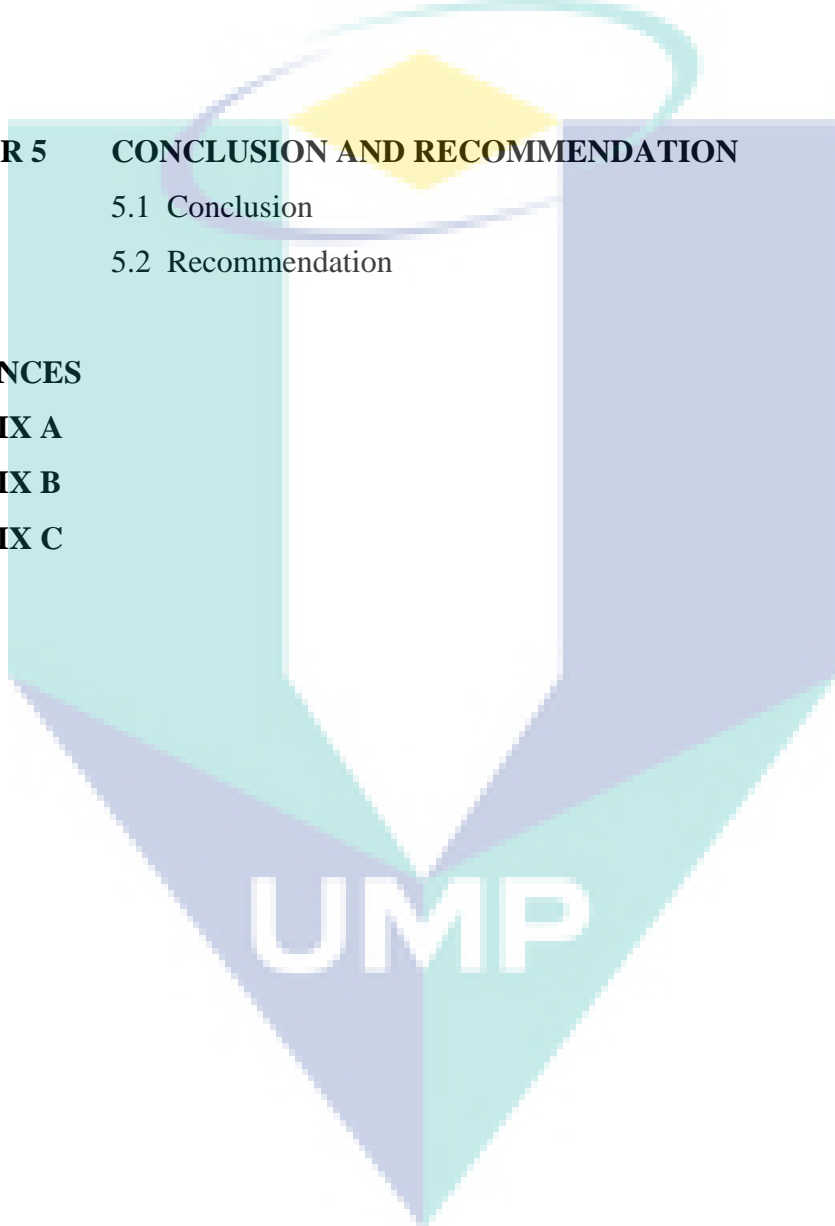
Vote No. : RDU110348

TABLE OF CONTENTS

CHAPTER	TITLE	Page
	TITLE PAGE	i
	ACKNOWLEDGEMENT	ii
	ABSTRACT	iii
	ABSTRAK	iv
	TABLE OF CONTENTS	v
	LIST OF TABLES	viii
	LIST OF FIGURES	ix
	LIST OF APPENDICES	xi
CHAPTER 1	INTRODUCTION	1
	1.1 Overview	1
	1.2 Problem Statement	2
	1.3 Objective	2
	1.4 Scope of Project	3
CHAPTER 2	LITERATURE REVIEW	4
	2.1 Light Emitting Diode	4
	2.1.1 Types of LED	5
	2.1.2 Advantages of using LED	7
	2.2 LED Driver	8

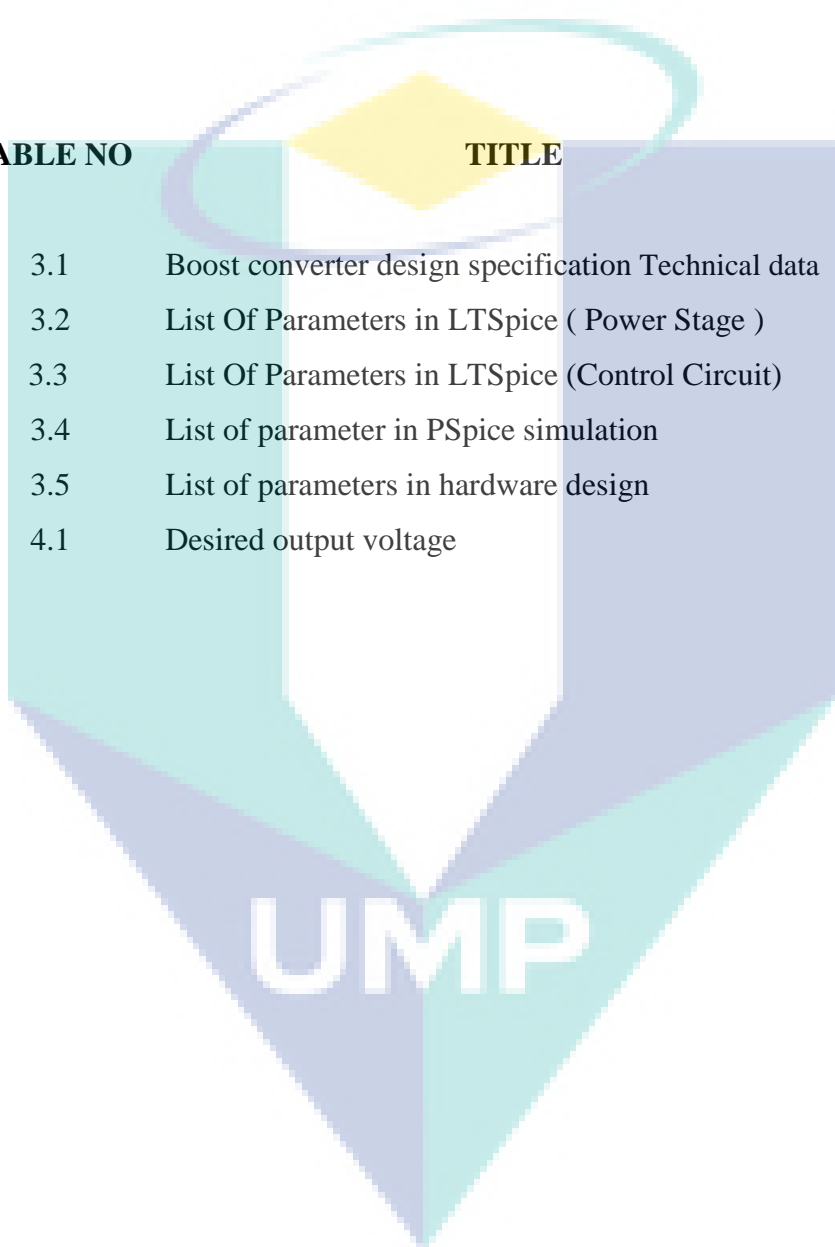
2.3	Boost Converter Circuit	8
2.3.1	Introduction of Boost Converter Circuit	8
2.3.2	The Boost Converter Topology	9
2.3.3	The Boost Converter Theoretical	11
2.4	Current Mode PWM Controller	13
CHAPTER 3	METHODOLOGY	14
3.1	Introduction	14
3.2	Flowchart of the Project	15
3.3	Software Part	16
3.3.1	Printed Circuit Board (PCB) Design Layout by Using EAGLE Software	18
3.4	Design Specification	18
3.5	Circuit Components	21
3.5.1	Inductor	21
3.5.2	Resistor	22
3.5.3	Diode	22
3.5.4	Capacitor	22
3.5.5	MOSFET	23
3.5.6	Light Emitting Diode (LED)	23
3.5.7	LTC 3683 Current Mode PWM Controller	24
3.5.8	Features of LTC 3783	25
CHAPTER 4	RESULT AND ANALYSIS	26
4.1	LTspice Simulation Result	26
4.2	Analysis and Result	26
4.3	Experimental Result	29

4.4	Discussion	32
4.5	PSpice Simulation Result	32
4.6	Hardware Result	34
4.6.1	Result from Oscilloscope	34
4.6.2	Result from Multimeter	36
CHAPTER 5	CONCLUSION AND RECOMMENDATION	38
5.1	Conclusion	38
5.2	Recommendation	39
REFERENCES		40
APPENDIX A		42
APPENDIX B		50
APPENDIX C		55



LIST OF TABLES

TABLE NO	TITLE	PAGE
3.1	Boost converter design specification Technical data	19
3.2	List Of Parameters in LTSpice (Power Stage)	19
3.3	List Of Parameters in LTSpice (Control Circuit)	19
3.4	List of parameter in PSpice simulation	20
3.5	List of parameters in hardware design	20
4.1	Desired output voltage	32

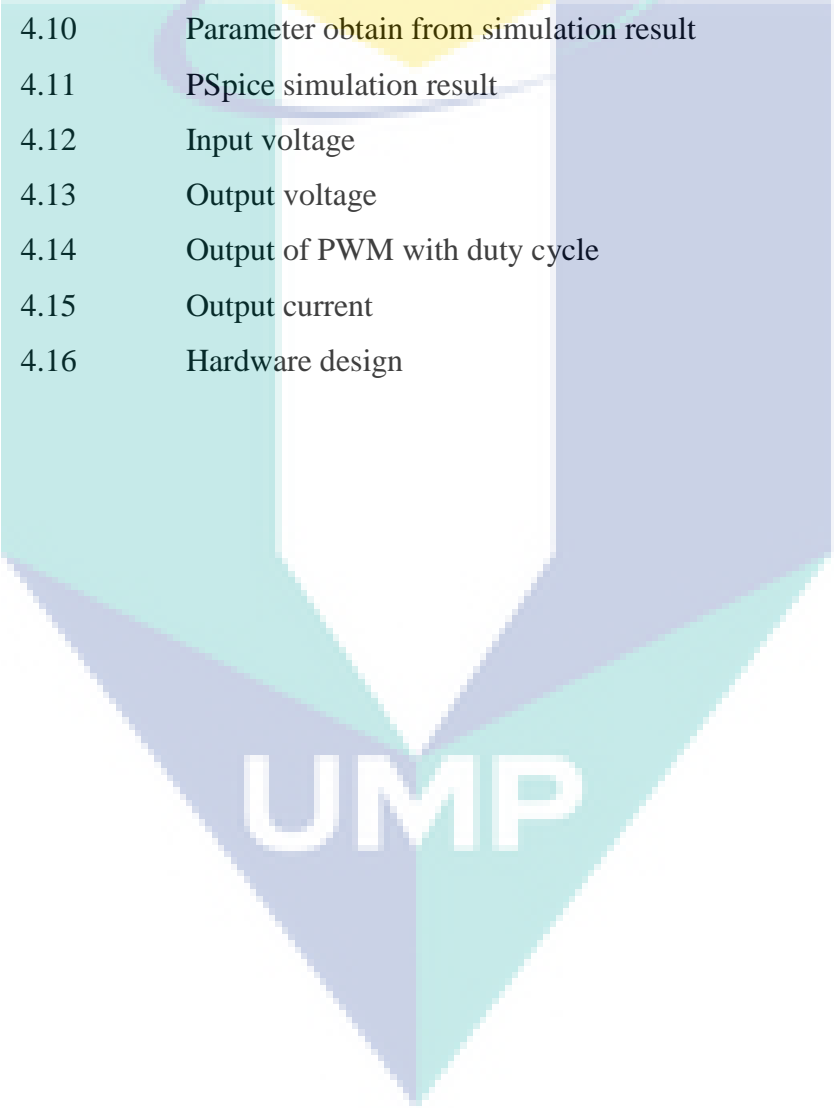
The logo for UMP (Universiti Malaysia Perlis) is a large, downward-pointing arrow shape. It is composed of four quadrants: top-left is light blue, top-right is light purple, bottom-left is light purple, and bottom-right is light blue. The letters 'UMP' are written in white, bold, sans-serif font across the center of the arrow.

UMP

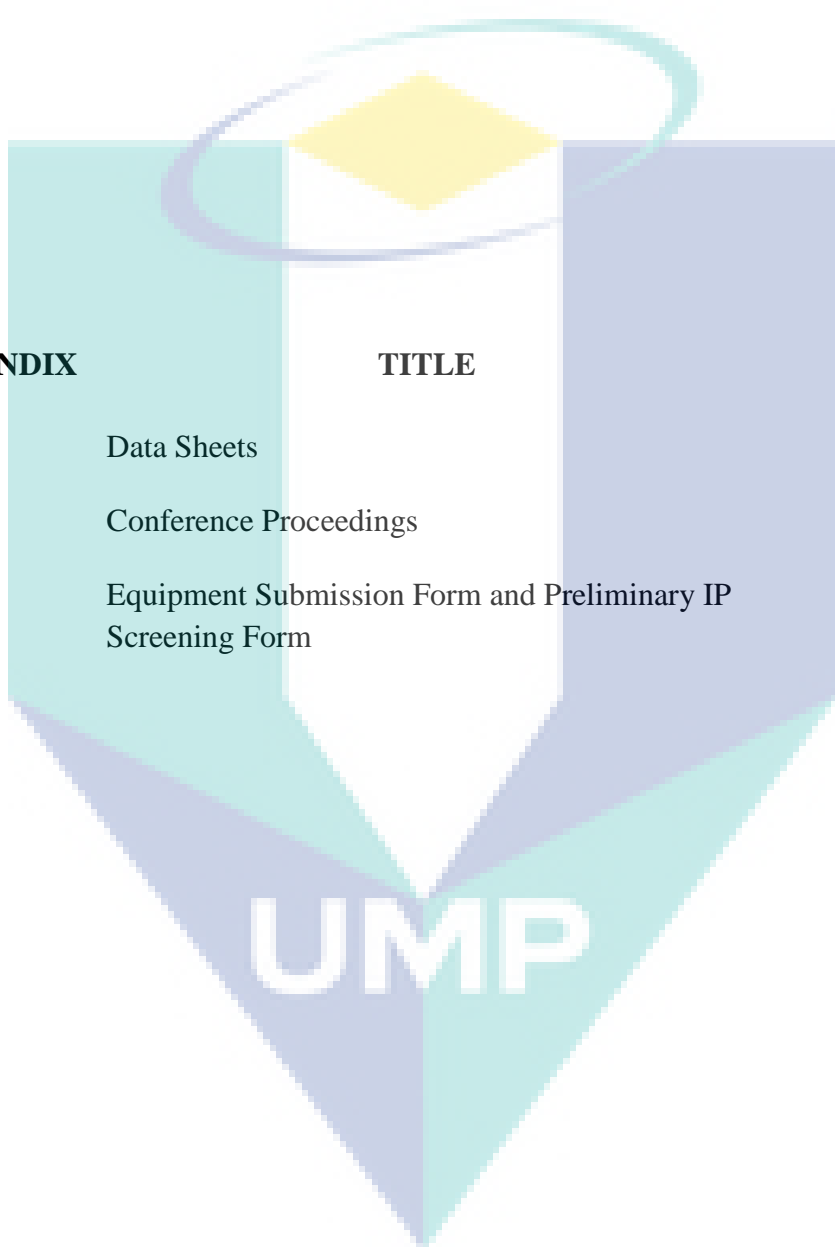
LIST OF FIGURES

FIGURE NO	TITLE	PAGE
2.1	PN junction image	4
2.2	Structure of power LED package	5
2.3	Low Power LED	6
2.4	High Power LED	6
2.5	Basic schematic of boost converter	9
2.6	Positive Signal at Gate MOSFET	10
2.7	Negative Signal at Gate MOSFET	10
2.8	Inductor Voltage and Inductor Current	12
2.9	Current mode control and the waveform	13
3.1	Flowchart diagram	15
3.2	PSpice simulation circuit	17
3.3	LTSpice simulation circuit	17
3.4	Circuit design by EAGLE	18
3.5	Inductor	21
3.6	Resistor	22
3.7	Diode	22
3.8	Capacitor	23
3.9	MOSFET configuration	23
3.10	Power LED	24
3.11	LTC 3783	24
3.12	Pin configuration	25
4.1	Waveform of input voltage and output voltage	27
4.2	Waveform of output current	27

4.3	Waveform of current sense	28
4.4	Waveform of duty cycle	28
4.5	Input voltage to the drive driver circuit	29
4.6	Output voltage to the drive the LED string	30
4.7	Pulse Width Modulation at 0.01 duty cycle	30
4.8	Supply 12V to the PWM Pulse Width Modulation	31
4.9	Output voltage and current to the drive the LED string	31
4.10	Parameter obtain from simulation result	33
4.11	PSpice simulation result	33
4.12	Input voltage	35
4.13	Output voltage	35
4.14	Output of PWM with duty cycle	36
4.15	Output current	36
4.16	Hardware design	37

The logo for UMP (Universiti Malaysia Perlis) is a large, downward-pointing arrow shape. It is composed of four triangular sections meeting at a central point. The top-left and bottom-right sections are light blue, the top-right and bottom-left sections are light green, and the central point is white. The letters 'UMP' are written in a bold, white, sans-serif font across the center of the arrow.

UMP

LIST OF APPENDICES

APPENDIX	TITLE	PAGE
A	Data Sheets	42
B	Conference Proceedings	50
C	Equipment Submission Form and Preliminary IP Screening Form	55

CHAPTER I

INTRODUCTION

1.1 Overview

Currently, the advancement in the high-power LED are increasingly finding new application in emergency light, street lighting, traffic lights, automobiles, cars, flashlight and general purpose lighting. Because of their superior longevity, low maintenance requirement, improved luminance, there is no mercury inside the devices. Therefore, they perform an extremely long operating life [1].

Typical LED control circuits are designed around a buck, boost or flyback topology, and they are used to generate a constant DC current through a string of a given number of LEDs. Each of these topologies has advantages and disadvantages depending on the input voltage range, the number of LEDs being driven in series, the number of parallel LED strings, the LED output current, if isolation is required, if dimming is required, efficiency, size and cost. For this reason, many circuit variations exist to satisfy the many different LED applications. The new circuit is a resonant mode circuit that has been slightly modified from dimming fluorescent applications. It is for non-isolated, off-line applications, and can drive one or many LEDs in series, can be easily scaled for different LED current levels, and utilizes soft-switching for good efficiency [2].

LED lighting system consists of three major parts. The three major parts is power source, lighting controller, and LEDs module. LED's in series or parallel connection must be driven with a source of constant current. Most of LED's have a specified current level that will achieve the maximum brightness for high efficient level. This brings about the need for high-power LED driver that can deliver and regulate LED current in a power-efficient manner. Normally for high power LED module will produce heat after several times. It is difficult to control LED due to its electrical characteristics of nonlinearity and temperature sensitivity. This project is about constructing a controller circuit by using a current mode PWM controller as driver for LED module.

1.2 Problem Statement

The old lighting system have many disadvantages such as high energy consumption, low efficiency, less brightness and short lifetime compare with LED lighting system. A lot of devices today used LED because of it have advantages over old lighting system. But, the LED brightness is strongly dependent on its current, not depend to voltage. Besides that, current mode control can increase the LED efficiency compared to the voltage mode control. Therefore, a driver for current mode control is required to control and stabilize the high power LED circuit in addition to improve the efficiency of LED system.

1.3 Objective

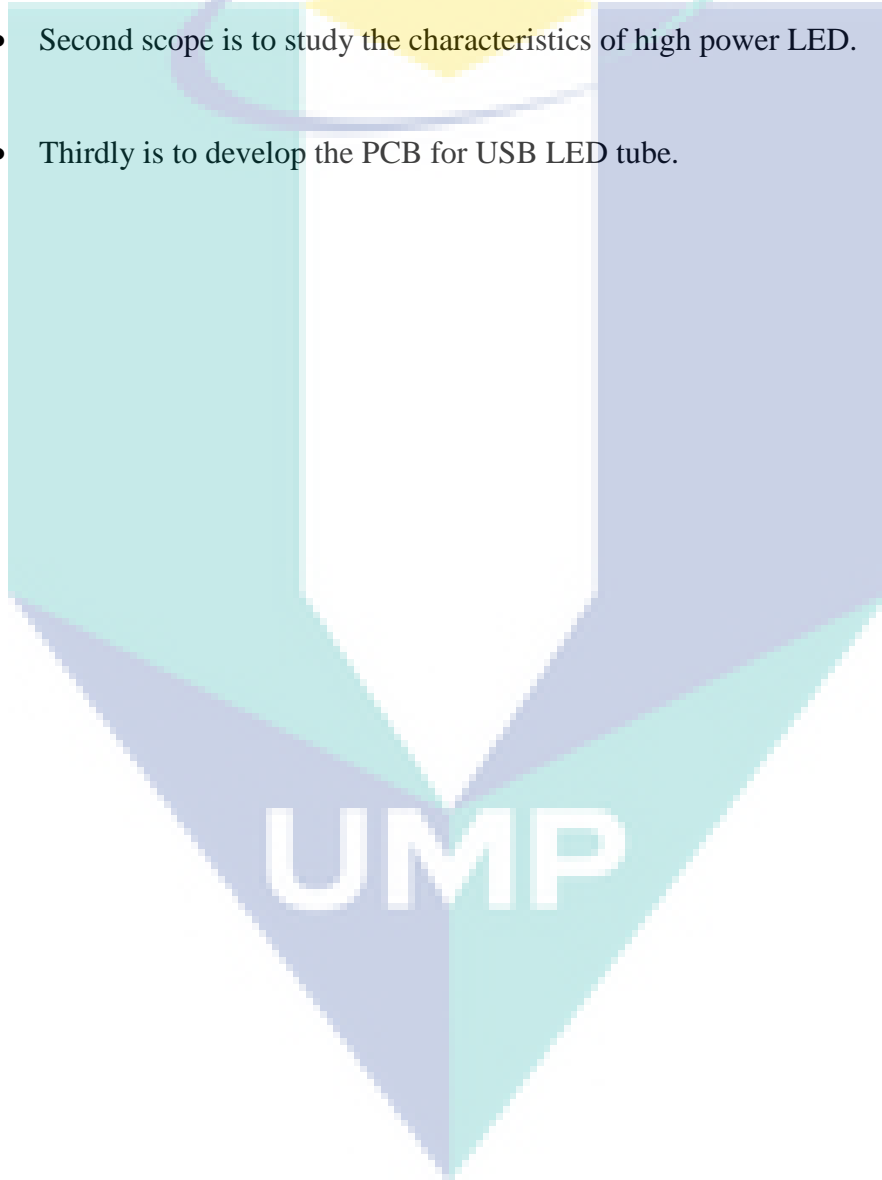
The objectives of this project are:

1. To develop high efficiency LED lighting system.
2. To develop driver circuit for LED.
3. To develop USB LED Tube.

1.4 Scope of Project

In this project, there are several scopes that were proposed. These scopes are important to achieve the objective at the end of this project. The scopes are:

- Firstly, understand the operation and characteristics of boost converter topology. The boost converter is a main converter for this project
- Second scope is to study the characteristics of high power LED.
- Thirdly is to develop the PCB for USB LED tube.



CHAPTER II

LITERATURE REVIEW

2.1 Light Emitting Diode

The new generation of high-power LED modules represents a significant advancement in LED design. Ranging from 1 watt to 10 watts, current high-power LED modules are capable of delivering between 10 and 50 Lumens/watt of light output. This level of light output is comparable to most incandescent lamps and even halogen bulbs in single-color applications. In addition, high-power LEDs are available in a variety of colors from multiple manufacturers, in discrete or pre-built modules [3].

An LED, on the other hand, is a semiconductor diode, a device that allows current to flow in only one direction. It's made of a chip of semiconducting material reacted to create a structure called a p-n (positive-negative) junction. The positive side contains excess positive charge ("holes," indicating the absence of electrons) while the negative side contains excess negative charge (electrons) [4]. Figure 2.1 shows the inner working in semiconductor of LED.

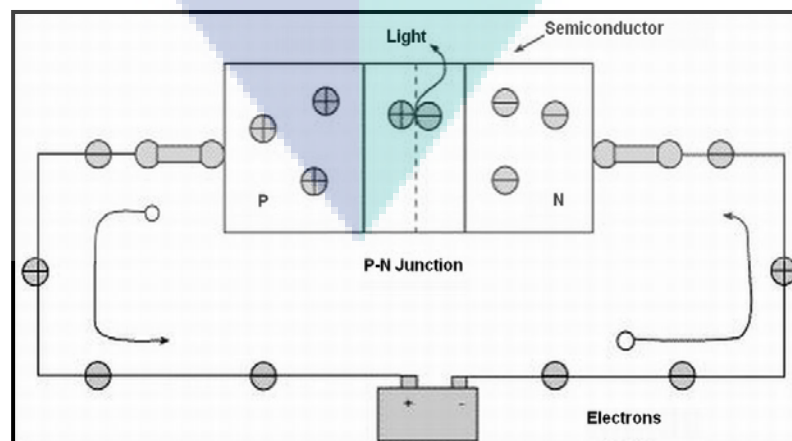


Figure 2.1: PN junction image [9]

When current is applied, the negatively-charged electrons move toward the positive side, and the positively-charged “holes” move toward the negative side. At the junction, the electrons and holes combine. As this occurs, energy is released in the form of light that is emitted by the LED.

Depending on the alloy used to make the semiconductor, the light emitted by the LED can range through the colors of the rainbow: red, orange, yellow, green, and blue. “White” light is created by combining the light from red, green, and blue (RGB) LEDs, or by coating a blue LED with yellow phosphor [4]. Figure 2.2 illustrates the construction for power LED package.

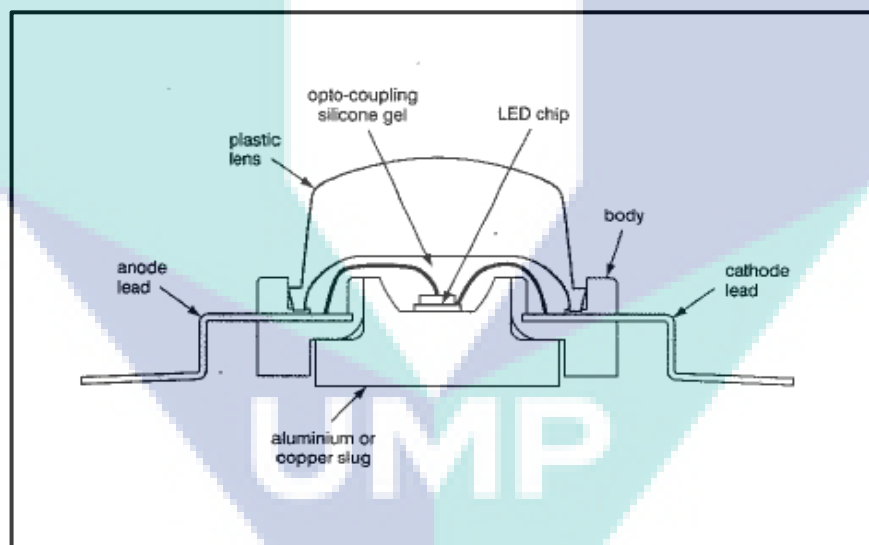


Figure 2.2: Structure of power LED package [8]

2.1.1 Types of LED

LED technology divide into two categories which is Low Power LED as shown in Figure 2.3 and High Power LED as depicted in Figure 2.4. Low power LEDs commonly operate at low current ($\sim 20\text{mA}$) and low voltage (3.2 volt DC). Low power LED only can produce a small amount of lumen per watt. For high power LEDs, it commonly comes in 1-10

watt packages. The construction of this LED can drive at much higher current, typically up to 1500mA. High power LED technology can produce 40- 80 lumens per watt. High power LED also come in many different shapes and sizes.

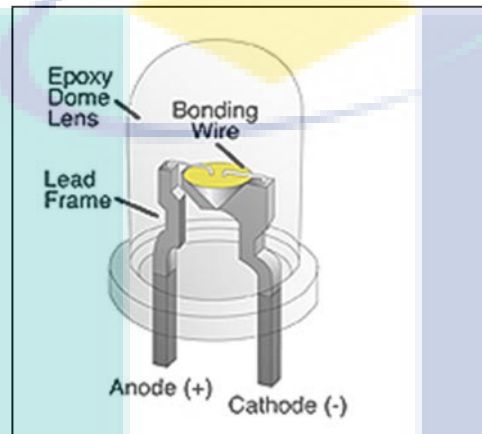


Figure 2.3: Low Power LED

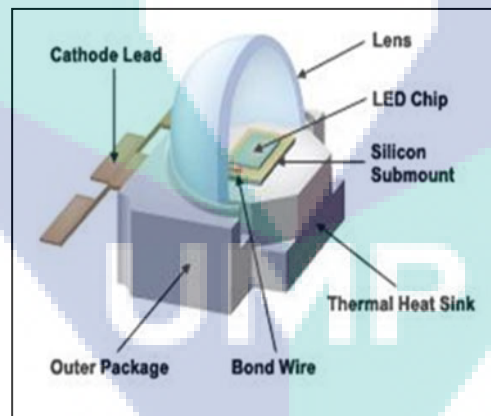


Figure 2.4: High Power LED

2.1.2 Advantages of using LED

High power LED have a few advantages compare to old lighting source. Traditional lighting manufacturers have formed partnerships with semiconductor manufacturers to develop next-generation lighting technology based on semiconductors. The new lighting technology offers some benefits in many industrial applications, including public and commercial signs, signaling, lighting and the automotive sector. The advantages of LED include:

- Long life - When the lighting assembly is correctly designed, a design life of 50 000 to 100 000 hours is realistic. As a result, maintenance requirements are drastically reduced, leading to a fundamental change in design methodologies. Life expectancy is unaffected by switching cycles and 100% output occurs within 10 nanoseconds.
- Defined colors - By their nature. LEDs produce very well defined colors without the need for colors filters. In a traditional red traffic signal using an incandescent source and colors filter, 90% of the light output is wasted.
- Physically robust - With no delicate glass or filaments, LEDs can withstand severe shock and vibration-a common cause of premature failure with traditional light sources.
- Environmentally friendly - LEDs, unlike fluorescent and other discharge tubes, do not contain mercury They are thus safer to manufacture and are free from end-of-life problems. Disposing of a fluorescent tube properly now costs more than buying a new tube.
- Cool and safe - The light output from LEDs can he free of infra-red or ultra-violet radiation. making them ideal for safety critical applications and situations where it may be necessary to the touch the lighting fixture [8].

2.2 LED Driver

Conventional lighting system use linear regulator as a switching controller. Linear regulator usually work quite well in the lighting system where the forward current is kept at a low level, whereas the efficiency drops as forward current rises. The operation for High Power LED is depending on current controlled devices rather than voltage. So, the current control mode must be used to increase the efficiency.

To operate LEDs correctly a constant current source must be used. With low-power devices in indicator applications a simple resistive current element is used to limit the maximum current flow to typically 10-30 mA through each LED. The move to higher-powered LEDs with forward currents in the region of 350-700mA necessitates the use of an active current control approach. Simple resistive elements would become inefficient and cannot control the forward current with the variation of LED forward voltage, which changes with respect to temperature. The driver circuits required tend to use switched-mode power conversion to attain a high total efficiency and cool running, and to maximize LED reliability [8]. In this project, boost converter is focused. The boost converter is applied because the load voltage is always higher than the supply, with a reasonable margin, the converter used must be the Boost topology. Otherwise, the Buck-Boost converter is preferred [9]. Pulse width modulation (PWM) technique is to be used to control the density of the LED light in the switching converters.

2.3 Boost Converter Circuit

2.3.1 Introduction of Boost Converter Circuit

The ideal boost converter has the five basic components. The basic component is a power MOSFET, diode, inductor, capacitor and PWM controller. The essential control mechanism of the circuit is turning the MOSFET will on and off at the gate (signal from PWM circuit). The output voltage of the boost converter is larger than the input. The input current for a boost converter is continuous, or non-pulsating, because the input current is the

same as the inductor current. However, the output current is discontinuous, or pulsing, because the output diode conducts only during a portion of the switching cycle. The capacitor supplies the entire load current for the rest of the switching cycle. The basic circuit of the boost converter is shown in Figure 2.5.

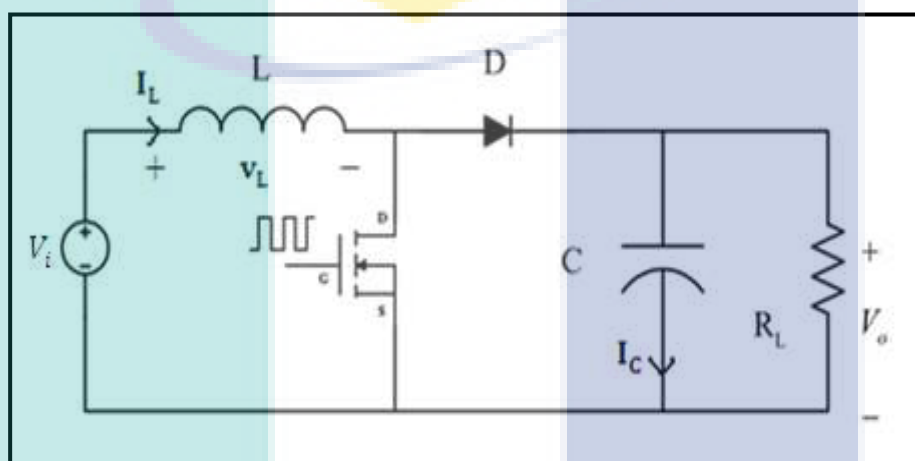


Figure 2.5: Basic schematic of boost converter

2.3.2 The Boost Converter Topology

The boost converter which can step-up the power supplies can also be known as a switching mode regulator. The main concept of the boost converter is by rapidly opening and closing the condition of the switch in order to control the flow of current through the inductor to the load.

When a positive signal is applied to the gate of the MOSFET, the current through the inductor increases and the energy stored in the inductor builds up. When the switch is off, the current through the inductor continues to flow via the diode D, the RC network, and back to the source. The inductor is discharging its energy and the polarity of the inductor voltage is such that its terminal connected to the diode is positive with respect to its other terminal connected to the source. It can be seen then that the capacitor voltage has to be higher than the source voltage and hence this

converter is known as the boost converter. It can be seen that the inductor acts like a pump, receiving energy when the switch is closed and transferring it to the RC network when the switch is open [5]. The diode stops to conduct when the negative signal will give at gate MOSFET and the capacitor sustains the output voltage. The circuit can divide into two parts, The Figure 2.6 shows for positive cycle and in Figure 2.7 shows for negative cycle.

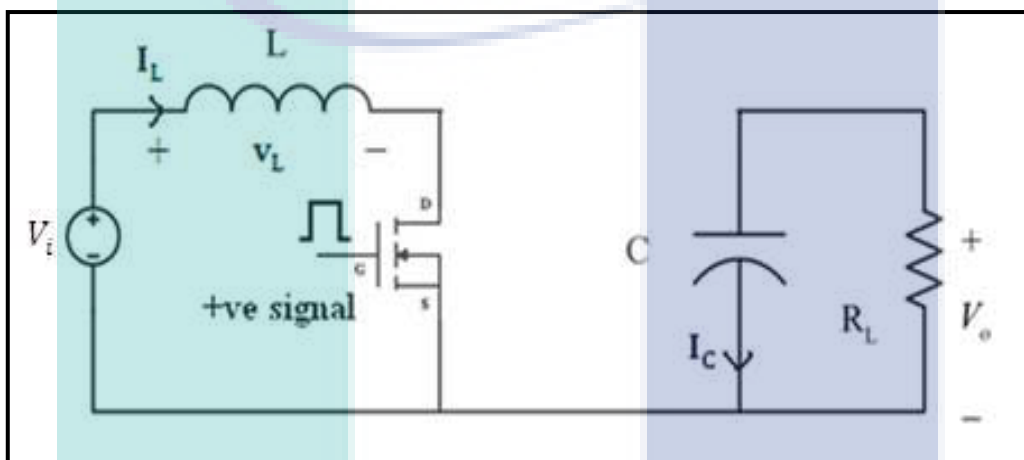


Figure 2.6: Positive Signal at Gate MOSFET

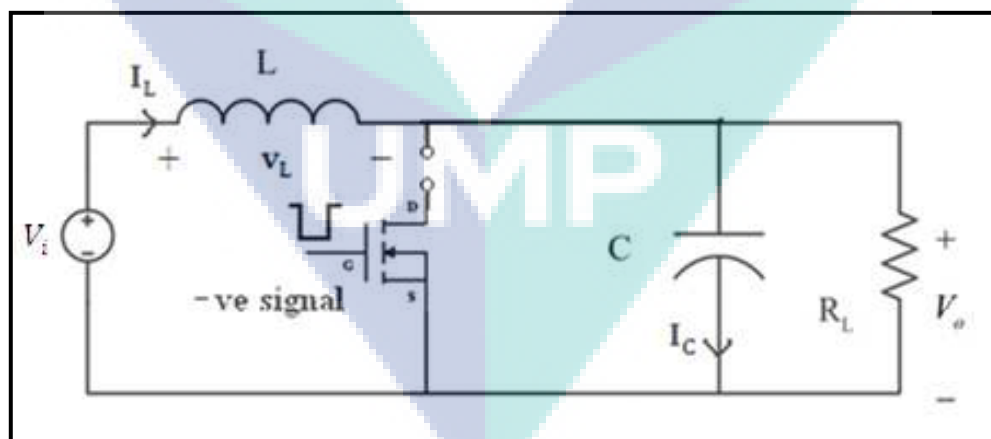


Figure 2.7: Negative Signal at Gate MOSFET

2.3.3 The Boost Converter Theoretical

The output to input relationship of boost converter is:

$$\frac{V_o}{V_i} = \frac{\eta}{(1-D)} \quad (2-1)$$

Where:

- V_o is the steady-state output voltage
- V_i is the supply voltage
- D is duty cycle
- η is the efficiency of the boost converter.

The inductor current is:

$$I_L = \frac{V_i}{(1-D)^2 R} \quad (2-2)$$

Where: R is the load of the boost converter.

The inductor in the boost converter can be determined by using the following expression:

$$L_{min} = \frac{D(1-D)^2 R}{2f} = \frac{V_i}{\Delta i_L} \cdot D \cdot T \quad (2.3)$$

Where:

- Δi_L is the ripple current in the inductor.
- T is the switching period.

The output voltage ripple, $\frac{\Delta V_o}{V_o}$ of boost converter is :

$$\frac{\Delta V_o}{V_o} = \frac{D}{RCf} \quad (2.4)$$

Where

- C is output capacitor value of boost converter.

The waveforms of inductor voltage and inductor current are shown in Figure 2.8. These waveforms are drawn assuming that both the output and the source voltage remain steady. These waveforms illustrate how the inductor voltage is related to its current. The minimum inductor can be seen equation (2.3) and maximum load can be seen equation (2.10).

$$R_{max} = \frac{2fL}{(1-D)^2} \quad (2.10)$$

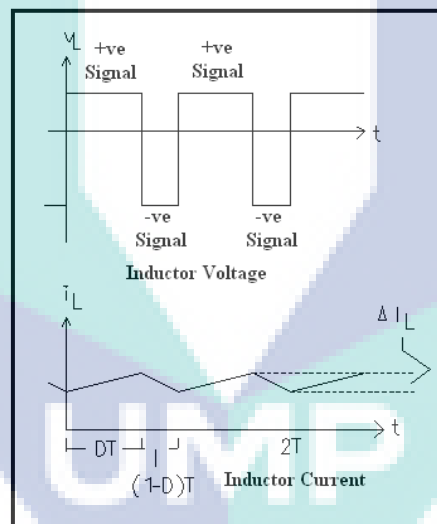


Figure 2.8: Inductor Voltage and Inductor Current

When the switch in the boost converter is in the ON state (close), there is no current flow through the load. When the switch is in the OFF state (open), the current flows towards the load. Hence, the waveform in the load is a pulse train with a high peak value in order to obtain the desired mean value. So, it needs a PWM controller to control the load current.

2.4 Current Mode PWM Controller

In this project, Current Mode Control (CMC) has been applied to control the output voltage. CMC has two connections from circuit that called inner loop and outer loop. Current mode control is a two-loop system. The switching power supply inductor is “hidden” within the inner current control loop. This simplifies the design of the outer voltage control loop and improves power supply performance in many ways, including better dynamics. The objective of this inner loop is to control the state-space averaged inductor current, but in practice the instantaneous peak inductor current is the basis for control. If the inductor ripple current is small, peak inductor current control is nearly equivalent to average inductor current control [6]. Figure 2.9 shows the graphical presentation of the current mode control.

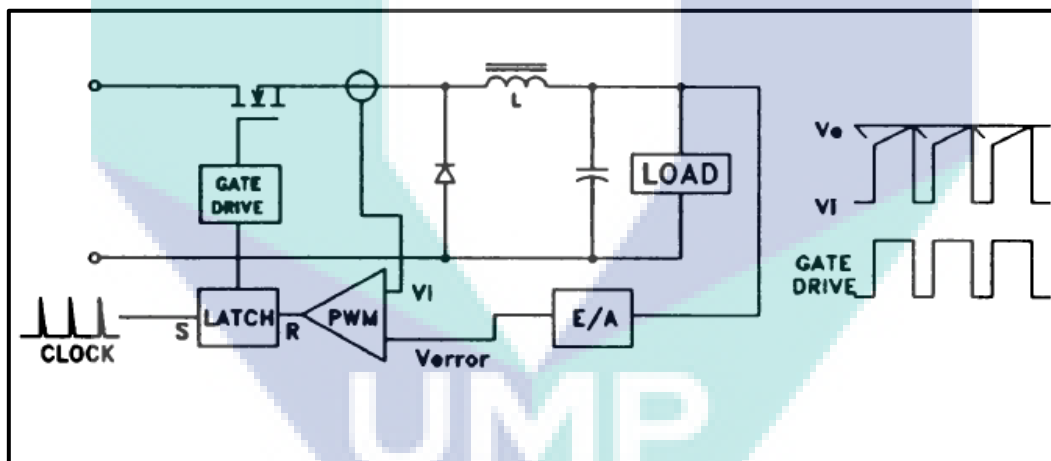


Figure 2.9: Current mode control and the waveform [6]

The operation of the current mode controller has advantages over a voltage mode controller. The first is that the inductor current is a direct function of the error voltage, so for small signal analysis the inductor can be replaced by a voltage controlled current source. This removes one order from the transfer function. The control loop is easier to compensate than a voltage mode circuit. Another advantage is that input line voltage changes are removed from the compensation problem. The peak current through the inductor is a function of the voltage across current to rise to the required value and for the comparator to shut off the switch [7].

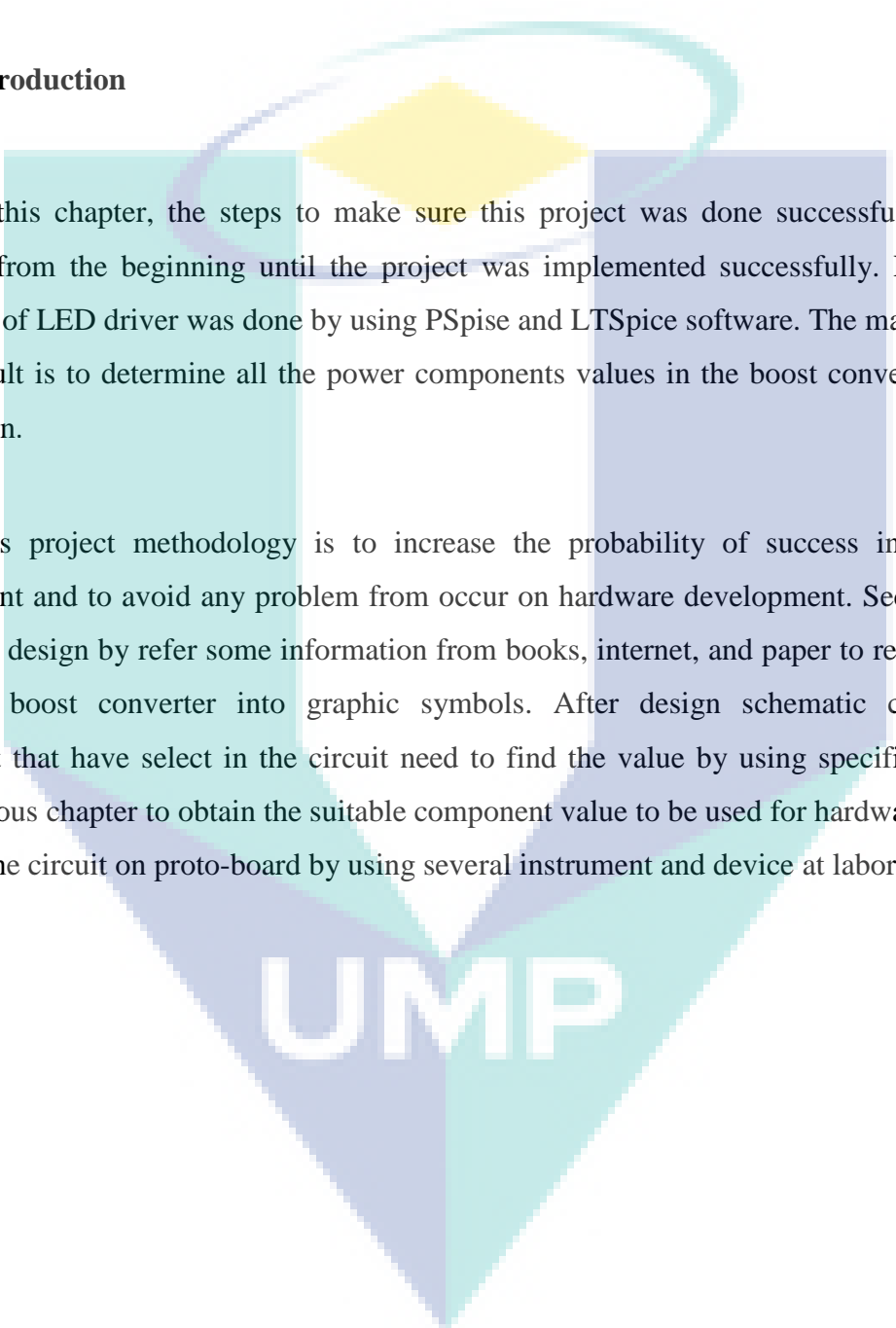
CHAPTER III

METHODOLOGY

3.1 Introduction

In this chapter, the steps to make sure this project was done successfully will be discussed from the beginning until the project was implemented successfully. Firstly, the simulation of LED driver was done by using PSpice and LTSpice software. The main purpose of this result is to determine all the power components values in the boost converter power stage design.

This project methodology is to increase the probability of success in hardware development and to avoid any problem from occur on hardware development. Secondly, the schematics design by refer some information from books, internet, and paper to represent the circuit of boost converter into graphic symbols. After design schematic circuit, the component that have select in the circuit need to find the value by using specific equation from previous chapter to obtain the suitable component value to be used for hardware. Finally is testing the circuit on proto-board by using several instrument and device at laboratory.



UMP

3.2 Flowchart of the Project

Figure 3.1 depicts the flow of this project. Basically the step that has been taken was divided into several parts.

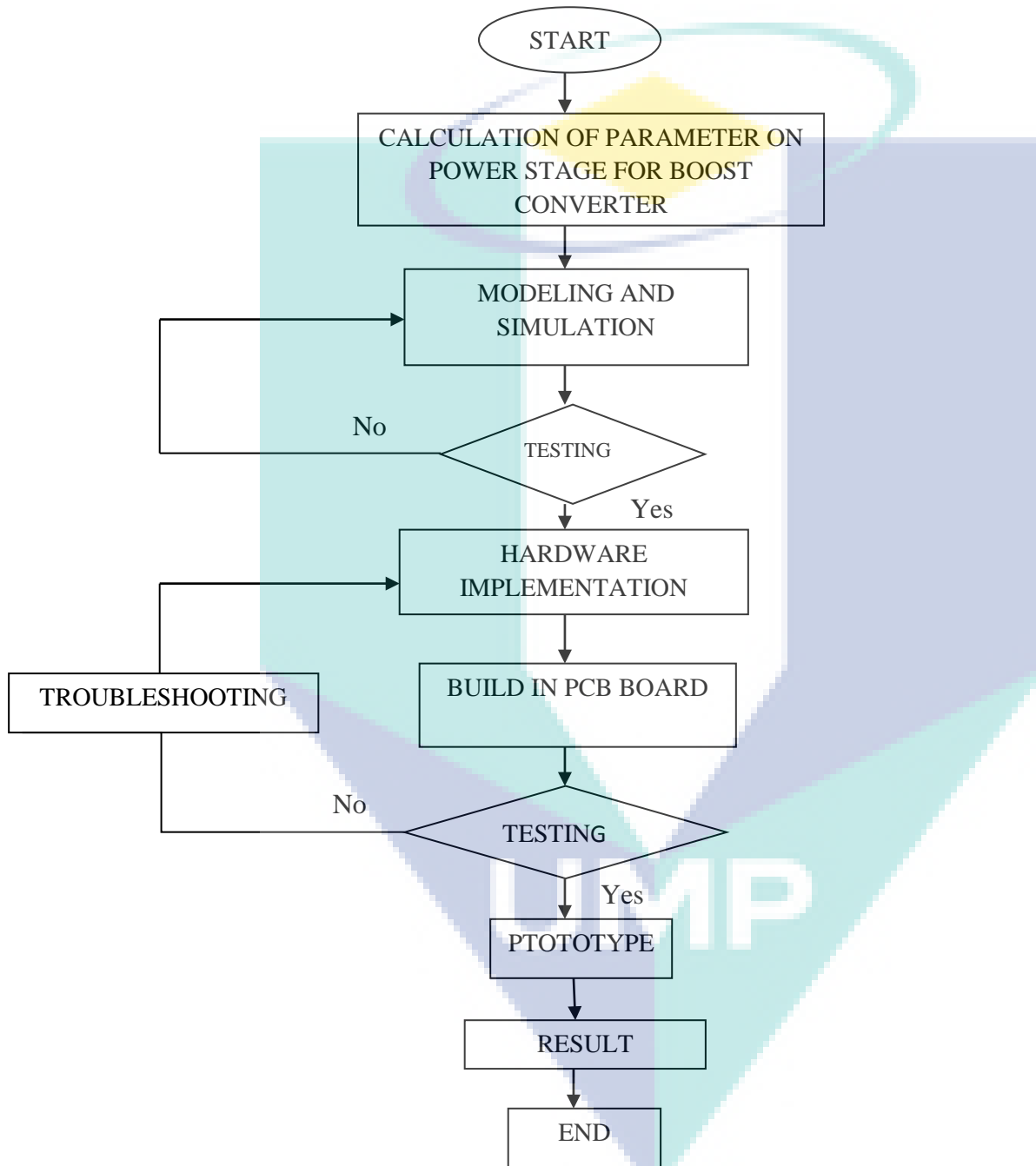


Figure 3.1: Flowchart diagram

3.3 Software Part

Before doing the hardware, the simulation part should be running in order to make sure that the circuit can operate correctly and achieve the purpose of the project. This part is important because by doing simulation, the fault on the circuit can be safely determine without use the real components. If any failure of the circuit operation occurs, the cause of the failure can be traced by this simulation. If the prototype is developed without doing the simulation, any failure of the circuit will cause the damage on the components. So, more budgets needed to buy the new components. By doing this simulation, the budget of the project can be minimized and components damage can be avoided.

For this project, the software that has been used:

- a) PSpice - for simulation
- b) LTspice – for simulation
- c) Eagle – for design PCB board

After done design the PSpice simulation in Figure 3.2, this project continues with the LTspice simulation in Figure 3.3 to make sure that the circuit will operate well. For this project, it used LTC 3783 current mode PWM controller as a main controller. The result of the LTspice simulation will almost same with the PSpice simulation which by regulating the input of supply in voltage and will get the fixed of output voltage. Before plot a board, the eagle software in Figure 3.4 used and convert to gerber file before import the file to circuit cam to design a PCB layout by using FR4 board. This board plotted by LPKF machine in version S103. The board is plotted in single layer.

3.3.1 Printed Circuit Board (PCB) Design Layout by Using EAGLE Software

EAGLE (Easily Applicable Graphical Layout Editor) by Cadsoft is a flexible and expandable schematic capture, PCB layout, auto router and CAM program. By using the Eagle Software the each component from testing on the breadboard will be solder at the PCB board. The arrangement has to be made carefully in order to prevent the short circuit at the board. The driver circuits are arranged very well as shown in Figure 3.4.

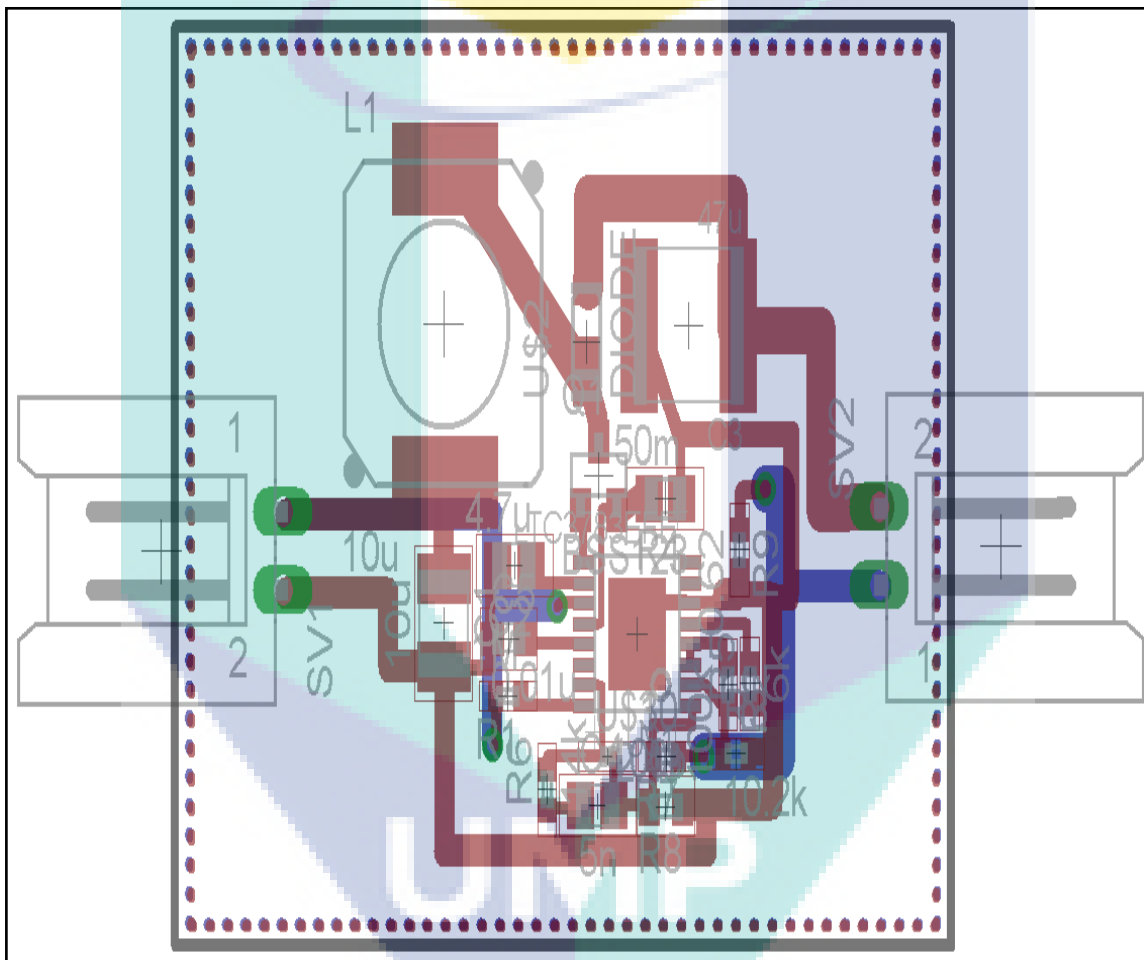


Figure 3.4: Circuit design by EAGLE

3.4 Design Specification

For hardware implementation part, the value of all components parameter must be design first. The value of the component will get by using all formula in Chapter 2. The specifications design for boost converter, simulators and hardware for this project is revealed in the following tables:

Table 3.1: Boost converter design specification

Specification	Value
Input Voltage	12V
Output Voltage	24V
Switching frequency	1MHz
Duty cycle	0.5
Maximum load	400 Ω
Inductor	10 μ H

Table 3.2: List Of Parameters in LTSpice (Power Stage)

Component	Value
Inductor,L1	10 μ H
Resistor,R1	1M Ω
Resistor,R3	0.65 Ω
Capacitor,C1	10 μ F
Capacitor,C3	47 μ F
Power Mosfet	S12308BDS
Diode	2.0A

Table 3.3: List Of Parameters in LTSpice (Control Circuit)

Component	Value
Capacitor,C4	4.7nF
Capacitor,C5	100pF
Capacitor,C6	0.01 μ F
Resistor,R2	0.05 Ω
Resistor,R4	6.04k Ω
Resistor,R5	10 Ω
Resistor,R6	2.49 Ω
Resistor,R7	14k Ω
Resistor,R8	10.2k Ω
Resistor,R9	100k Ω
PWM IC	LTC3783

Table 3.4: List of parameter in PSpice simulation

Component	Value
Inductor, L	30 μ H
Resistor,R1	0.1 Ω
Resistor,R2	100 Ω
Resistor,R3	50 Ω
Resistor,R4	50 Ω
Resistor,R5	39.2 Ω
Resistor,R6	2k Ω
Resistor,R7	1k Ω
Capacitor,C1	33 μ F
Capacitor,C2	8.2nF
Capacitor,C3	1.5 μ F

Table 3.5: List of parameters in hardware design

Component	Value
Inductor,L1	10 μ H
Resistor,R1	1M Ω
Resistor,R2	0.05 Ω
Resistor,R3	0.62 Ω
Resistor,R4	6.04k Ω
Resistor,R5	10 Ω
Resistor,R6	2.49 Ω
Resistor,R7	14k Ω
Resistor,R8	3.83k Ω
Resistor,R9	100k Ω
Capacitor,C1	10 μ F
Capacitor,C2	4.7 μ F
Capacitor,C3	47 μ F
Capacitor,C4	4.7nF
Capacitor,C5	100pF
Capacitor,C6	0.01 μ F

3.5 Circuit Components

This LED driver circuit consists of various types of electronic components such as inductor, resistor, capacitor, and diode, MOSFET, LED and PWM as a main controller. Basic information about the component used in this circuit will be described. The component that used is an electronic device so made is called a surface-mount device (SMD). Surface mount devices (SMDs) are used in a growing number of commercial and industrial products. Due to their small size, prototype manufacturing, rework, and repair can be difficult and are best performed using specialized techniques specific to this technology. Learning these techniques will help you succeed when working with these small components. SMDs have improved performance over through-hole components due to their smaller size, shorter internal leads, and smaller board layouts. These factors reduce the circuit's parasitic inductance and capacitance. SMDs can also be more cost effective than traditional through-hole components due to the smaller board size, fewer board layers, and fewer holes. SMDs can also be easier to replace than through-hole components on multilayer boards. This is because it is very difficult to heat the long hole on a multilayer board, but much easier to heat just the pad and component terminal of an SMD on the surface of a board.

3.5.1 Inductor

Inductors as depicted in Figure 3.5. are one of the basic components used in electronics where current and voltage change with time, due to the ability of inductors to delay and reshape alternating currents.



Figure 3.5: Inductor

3.5.2 Resistor

This component was used to limit the current flow in the circuit, reducing the voltage and divide the voltage in Figure 3.6.



Figure 3.6: Resistor

3.5.3 Diode

Diode as illustrated in Figure 3.7 is mostly used for many purpose in electronic circuits. Diode is used to allow current flow in one direction only as mention by the arrow in the symbol which acts as an open circuit in the opposite direction.

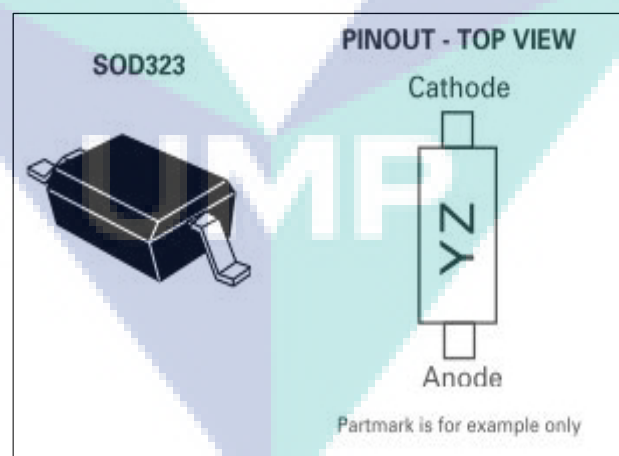


Figure 3.7: Diode

3.5.4 Capacitor

Capacitor in Figure 3.8 is commonly used as a storage and removal charges. It is usually used with the inductor to act as a filter to the circuit.



Figure 3.8: Capacitor

3.5.5 MOSFET

MOSFET is widely used in electronics. The MOSFET is used as an amplifier and also as a switch. It consists of three legs which is base, collector and emitter. MOSFET is a voltage-controlled device and is relatively simple to turn on and off. Typically, to turn a power MOSFET on, the gate terminal must be set to a voltage at least 10 V greater than the source terminal. This is comfortably above the V_{gs} parameter. In this project, the Si2308BDS is selected. The high operating voltage range of the output stage provides the drive voltages required by gate controlled devices. Figure 3.9 shows the configuration of Si2308BDS.

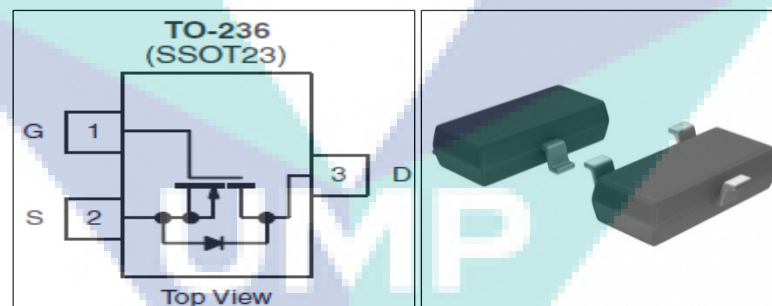


Figure 3.9: MOSFET configuration

3.5.6 Light Emitting Diode (LED)

A light emitting diode (LED) in Figure 3.10 is essentially a PN junction semiconductor diode that emits light when current is applied. It is solid-state device that control current without heated filaments and is therefore very reliable. LED performance is based on a few primary characteristics which are color, light, intensity, visibility, and operating life.

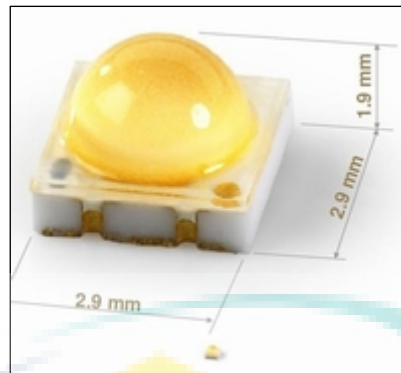


Figure 3.10: Power LED

3.5.7 LTC 3783 Current Mode PWM Controller

After designing of the power stage and loop compensator, the next procedure is the hardware implementation. In this chapter, the PWM controller will be focused. A chip LTC 3783 current mode PWM controller will be used as the main controller.

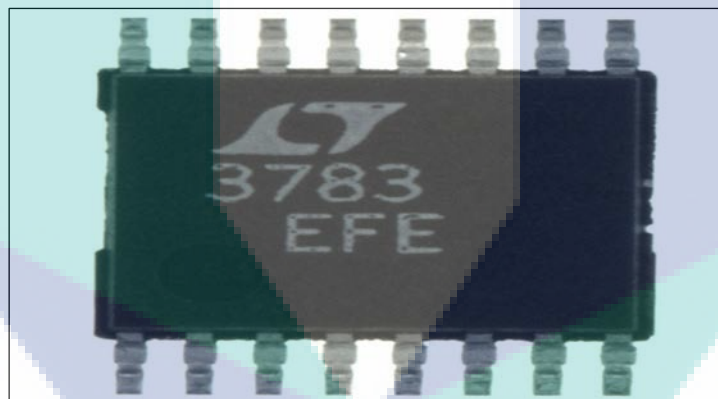


Figure 3.11: LTC 3783

The LTC 3783 is the high performance of programmable operating frequency with 20 kHz to 1MHz. The LTC3783 is a constant frequency, current mode controller for PWM LED with dc-dc boost converter.

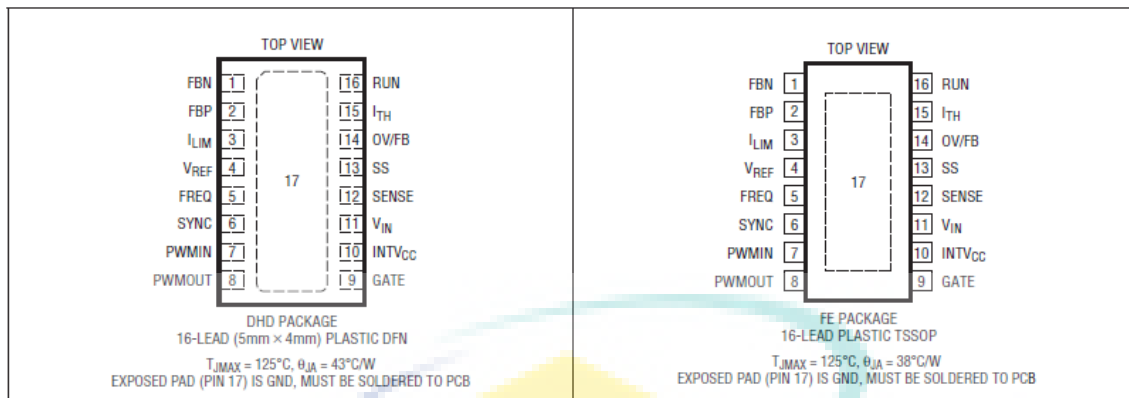


Figure 3.12: Pin configuration

3.5.8 Features of LTC 3783

- i. Fully integrated load FET driver for PWM dimming control of high power LEDs
- ii. Wide FB voltage range : 0V to 1.23V
- iii. Constant current or Constant voltage regulation
- iv. 1% 1.23 internal voltage regulation
- v. 2% RUN pin threshold with 100mV hysteresis
- vi. Programmable operating frequency : 20kHz to 1MHz
- vii. Internal 7V low dropout voltage regulator
- viii. Programmable output overvoltage protection
- ix. Programmable soft start

UMP

CHAPTER IV

RESULT AND ANALYSIS

4.1 LTspice Simulation Result

The main purpose of LTspice simulation result is to predict the result of the current mode control for boost converter. This result can use in hardware development. The main target to do the simulation is to obtain the value of the parameter of the component that will be implemented to the hardware. The output voltage, waveform of the current sense which represents the inductor current and also gate voltage also should be notified.

4.2 Analysis and Result

By fixed 12V as input supply, the output voltage will get 20.6V and the current 920mA. This output rating is suitable to drive LED string because this value is under typical rating for each High Power LED. The PWM IC will represent the waveform of the inductor current and gate voltage in the same time. The duty cycle is 0.01. The switching frequency use is 1MHz. Figure 4.1 shows the input voltage and output voltage. Figure 4.2 depicts the waveform of output current. The Figure 4.3 demonstrates the waveform of inductor current (current sense) and Figure 4.4 depicts the waveform at gate MOSFET (duty cycle).

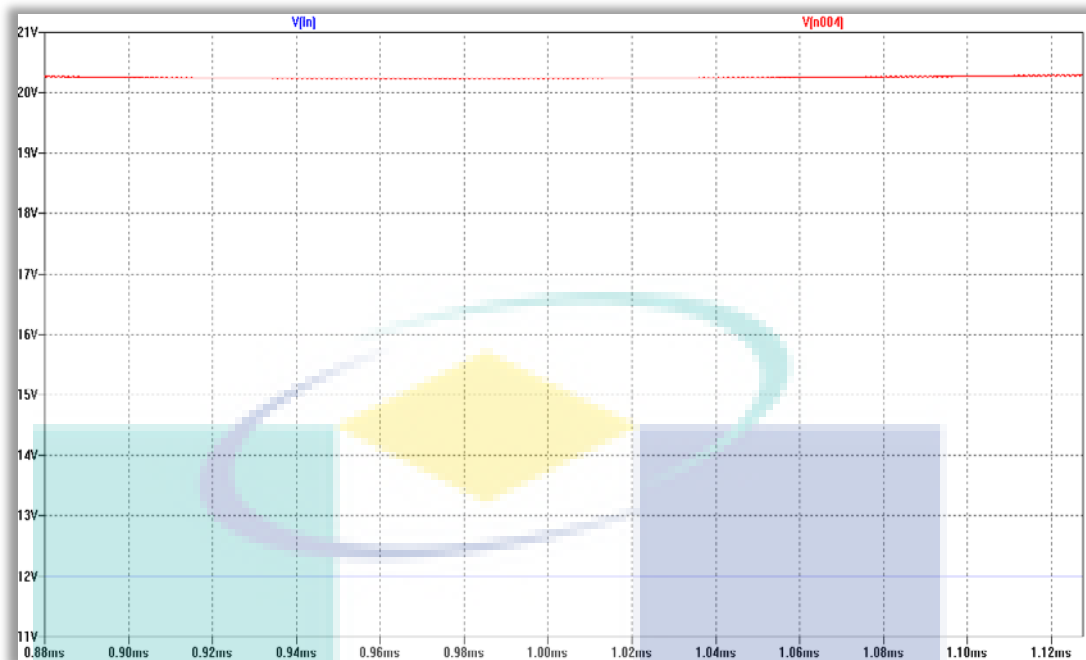


Figure 4.1: Waveform of input voltage and output voltage

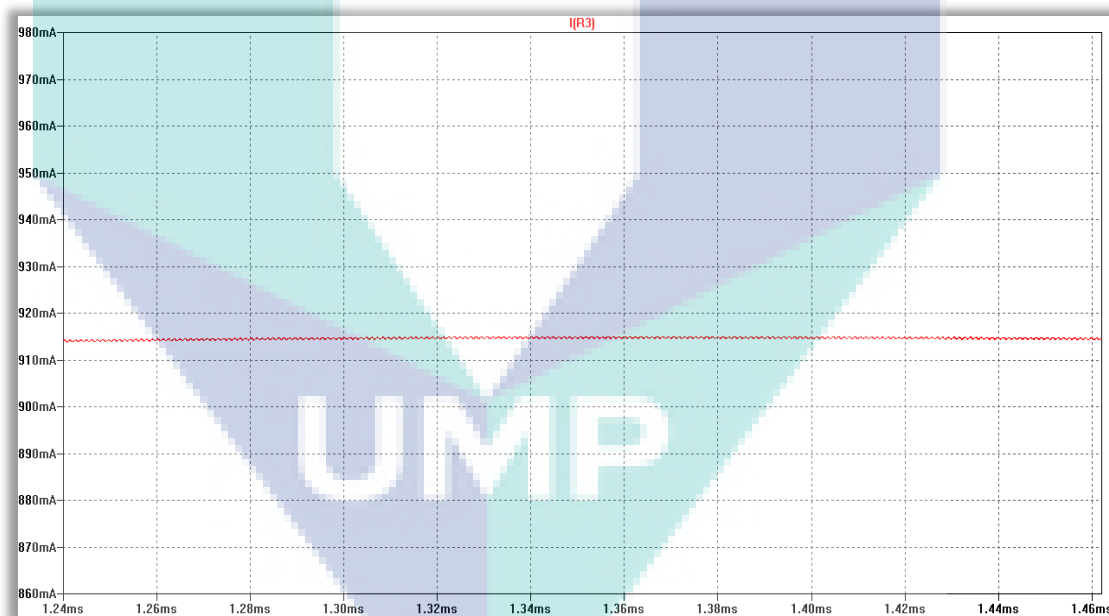


Figure 4.2: Waveform of output current

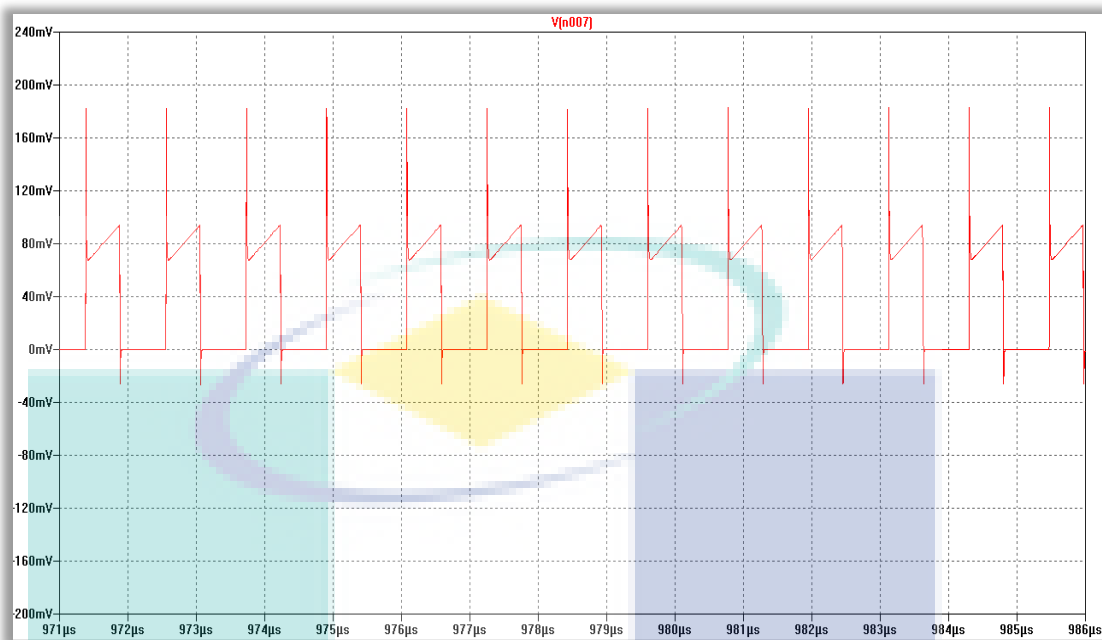


Figure 4.3: Waveform of current sense

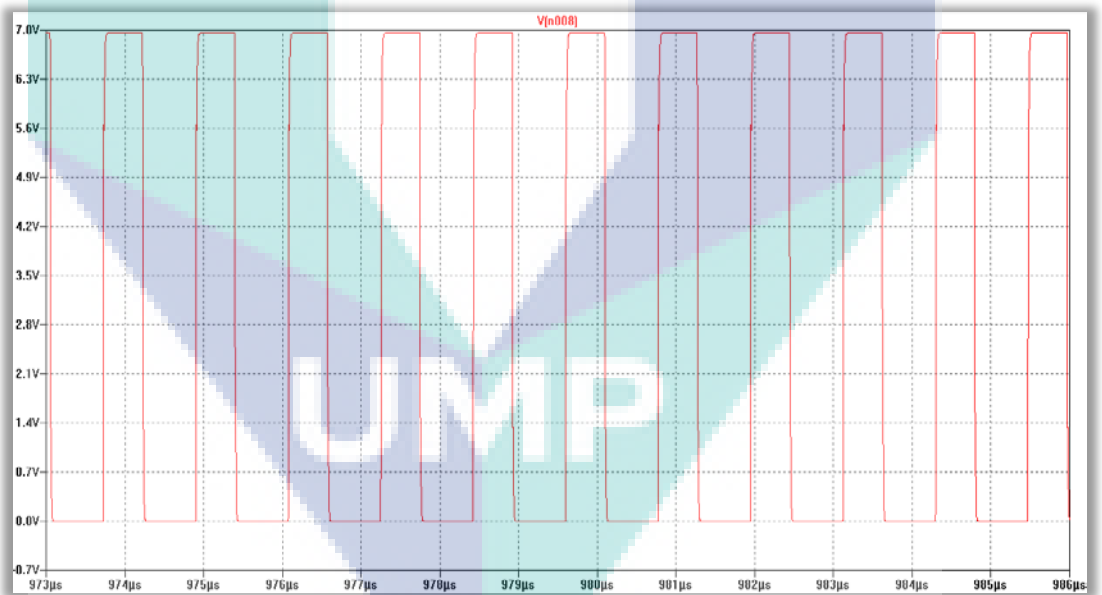


Figure 4.4: Waveform of duty cycle

Figure 4.4 shows that the result of PWM waveform for boost converter. The duty cycle of 0.01 show that this PWM waveform. The error amplifier generates is comparing an output voltage and the voltage at voltage reference to controlling the output voltage. It generated from the internal oscillator by connecting the timing

resistor at frequency pin. At this time, the actual frequency 1MHz also can be proof. It will produce the PWM output which is a square wave (Figure 4.3 and 4.4).

4.3 Experimental Result

Oscilloscope is used for analysis after done the hardware implementation. Firstly, the analysis had done on the PWM control IC which is use the LTC3783 to get square waveform. This waveform are represent the gate driver signal to drive get MOSFET. Lastly, analysis at power stage is done to get the output voltage and current to drive the LED string as a load. The following figures show the result that get in hardware implementation.

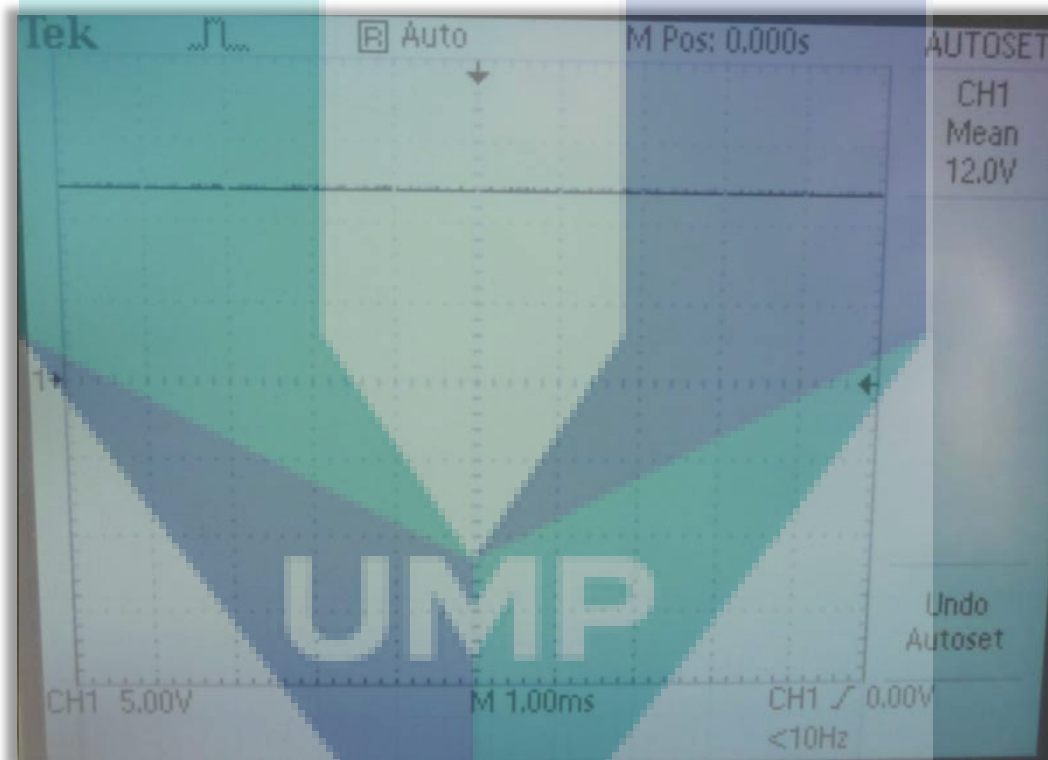


Figure 4.5: Input voltage to the drive driver circuit

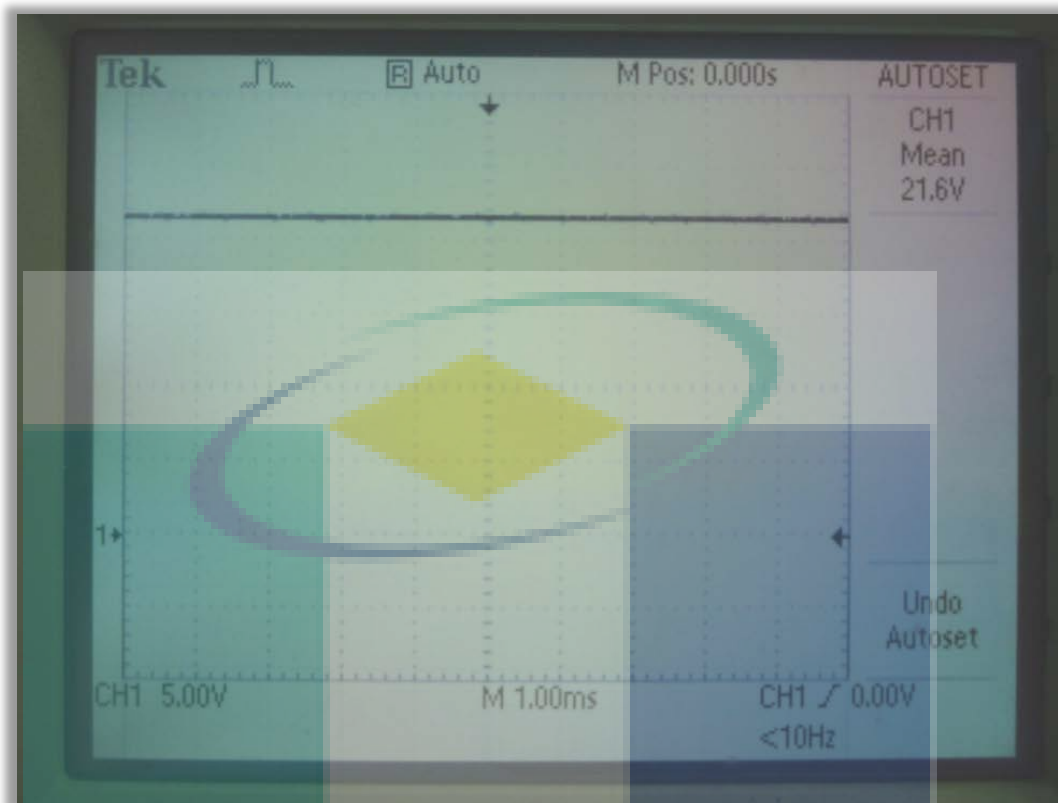


Figure 4.6: Output voltage to the drive the LED string

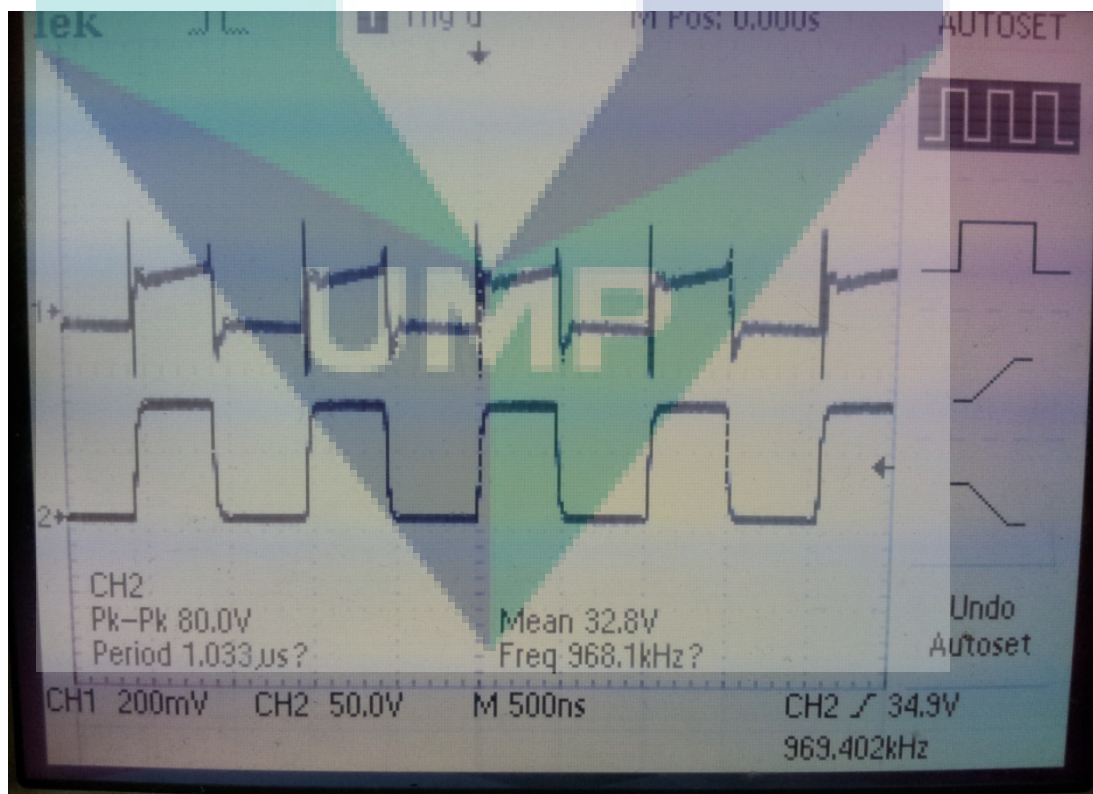


Figure 4.7: Pulse Width Modulation at 0.01 duty cycle

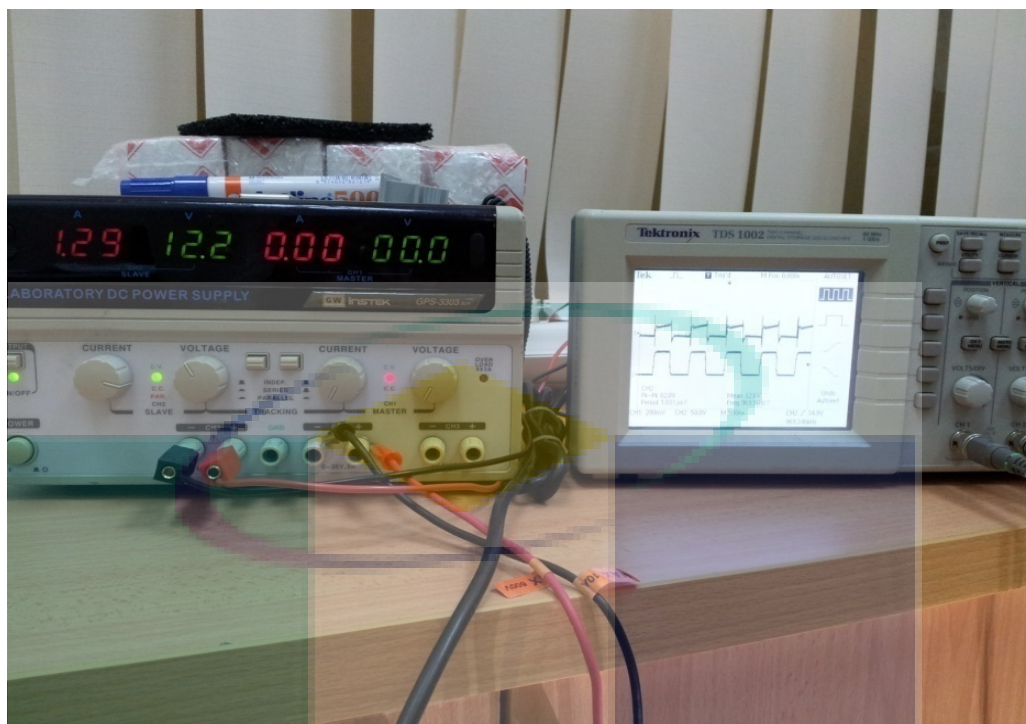


Figure 4.8: Supply 12V to the PWM Pulse Width Modulation



Figure 4.9: Output voltage and current to the drive the LED string

Figure 4.7 depicts that the result of PWM waveform for boost converter. The duty cycle of 0.01 show that this PWM waveform. The error amplifier generates is comparing an output voltage and the voltage at voltage reference to controlling the output voltage. It generated from the internal oscillator by connecting the timing

resistor at frequency pin. At this time, the actual frequency 1MHz also can be proof. It will produce the PWM output which is a square wave (Figure 4.7).

4.4 Discussion

The voltage output cannot reach to higher limit cause of the component condition. The simulation and hardware implementation can show that the current is really to control to achieve the output range. The capacitor also can be used at the output and the soft start pin to smoothen the transition. The waveform obtained is not smooth and stable cause of component heat after several times. It may happen cause of noises came from the circuit and can bring losses in the circuit. So it can affect the efficiency of the driver.

4.5 PSpice Simulation Result

At the end of this project, the Pspice simulation will be completed and the current mode control for boost converter will be design into hardware to ensure the stability where the power converter will return to the desired operating point after some disturbances are applied. Table 4.1 shows the expected result when the input voltage is varying.

Table 4.1: Desired output voltage

Input Voltage	Desired Output Voltage
12V	24 V
15 V	24 V

The simulation must be done before starting the hardware implementation since this simulation result determines input and output voltage. Duty cycle and switching frequency must be changed to 0.5 and 500 kHz. Figure 4.11 show results for Pspice simulation which the input voltage is varying from 12V to 15V and output voltage is 24V and there is some ripple voltage at the output voltage. The Figure 4.10 shows the parameter value that obtain from the simulation

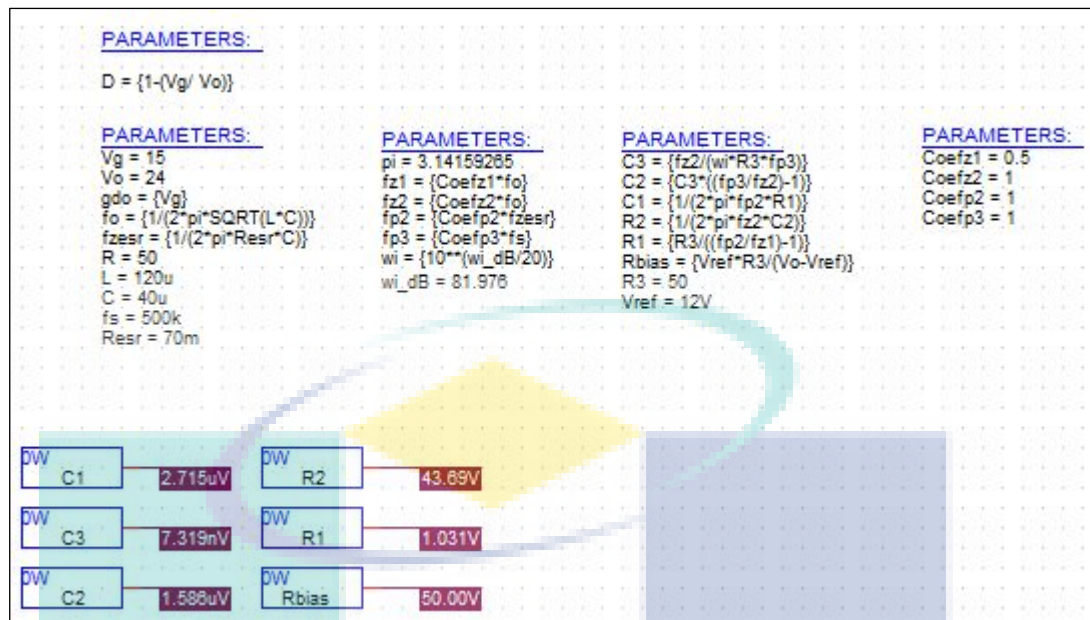


Figure 4.10: Parameter obtain from simulation result

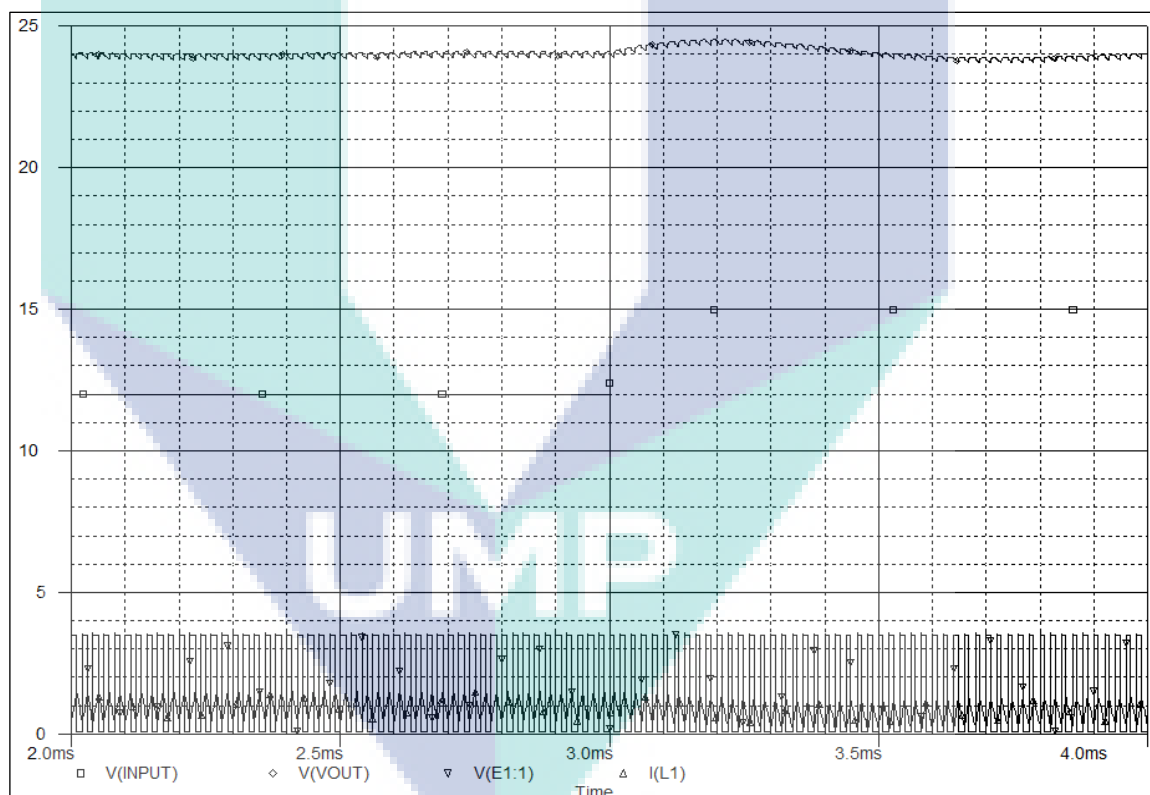


Figure 4.11: PSpice simulation result

The simulation part should be running in order to make sure that the circuit can operate correctly and achieve the purpose of the project. This part is important because by doing simulation, the fault on the circuit can be safely determine without use the real components. If any failure of the circuit operation occurs, the cause of

the failure can be traced by this simulation. If the prototype is developed without doing the simulation, any failure of the circuit will cause the damage on the components. So, more budgets needed to buy the new components. By doing this simulation, the budget of the project can be minimized and components damage can be avoided. For a power LEDs driver, it consists of two main circuits of power stage and PWM controller. In the current mode PWM controller, the loop compensator is the important path in the PWM controller design and overall boost converter design. The loop compensator will stabilize the system when some of the parameters in the design circuit are changed.

The simulation result by LTspice is determined. The parameter that have used in this simulation is used to implement into hardware. From the result that have done, we get the output current is 0.4 A and the output voltage is 19.5 V. LTspice simulation done and the real parameter implemented into hardware.

4.6 Hardware Result

4.6.1 Result from Oscilloscope

The hardware circuit is used to measure the efficiency and power loss on the circuit. The value of frequency in the PWM circuit is 965.3 kHz and the duty cycle is 0.5 as the value in calculation to obtain the equal output voltage which is 24V. Figure 4.12 shows the input voltage is equal to 8V and Figure 4.13 displays the output voltage is equal to 19.5 V and output current is equal to 0.4A.

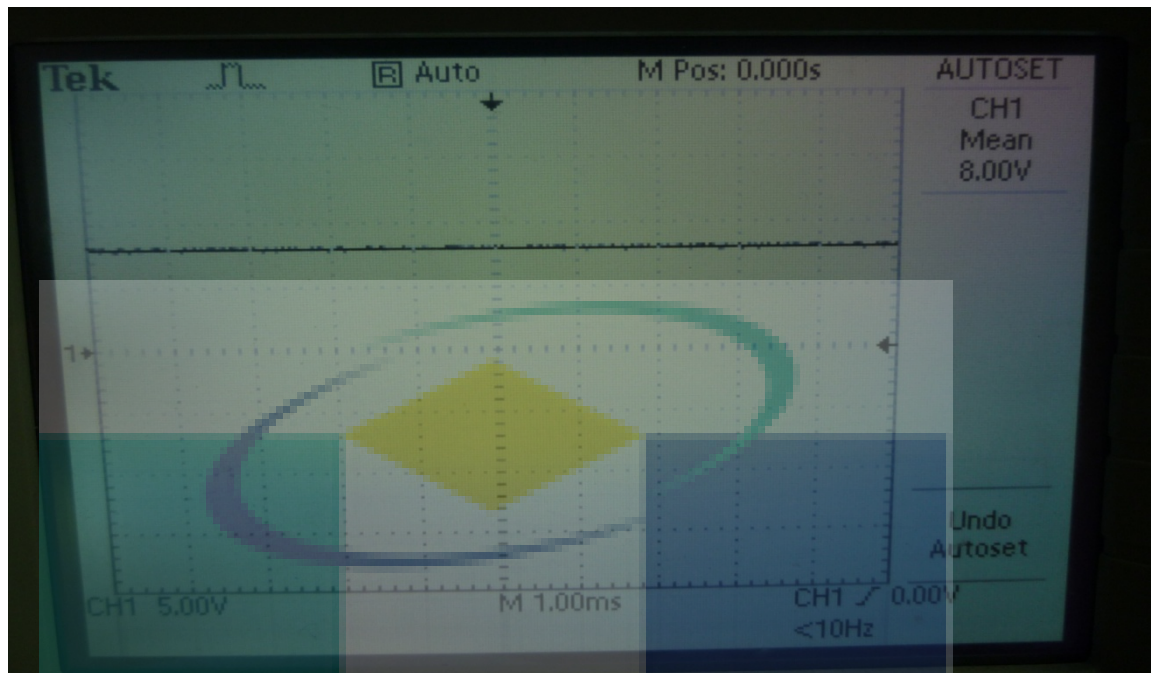


Figure 4.12: Input voltage



Figure 4.13: Output voltage

By using oscilloscope, Figure 4.13 shows duty cycle waveform, frequency is remain constant between 965 kHz to 966 kHz. Figure 4.14 demonstrates the output of PWM with duty cycle is equal to 0.5, input voltage is 8V, the output voltage is 19.5V and the frequency is 965.3 kHz.

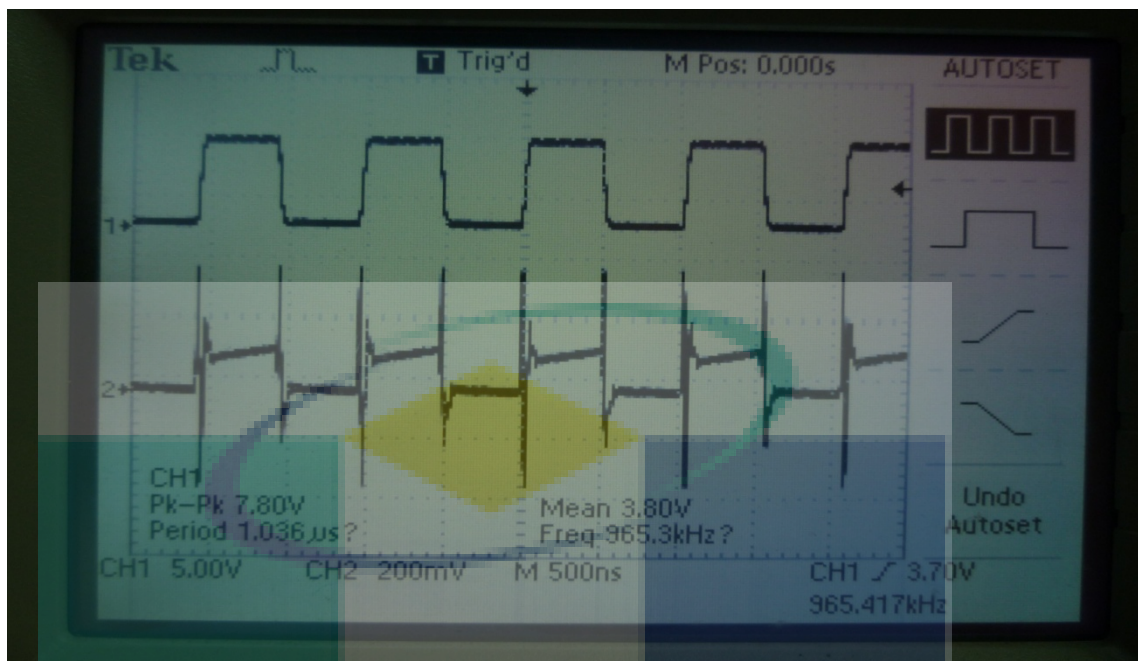


Figure 4.14: Output of PWM with duty cycle

4.6.2 Result from Multimeter

The output voltage is 19.5V from the 8V input voltage and the output current that have measured by multimeter is 0.4 A. There are some losses occur during troubleshooting. The required current that should drive a power LED is about 0.4A which is 0.2 for each series. The typical current is selected for make sure that the temperature is suitable for making a long life service. The output current and hardware design are show in Figure 4.15 and Figure 4.16.

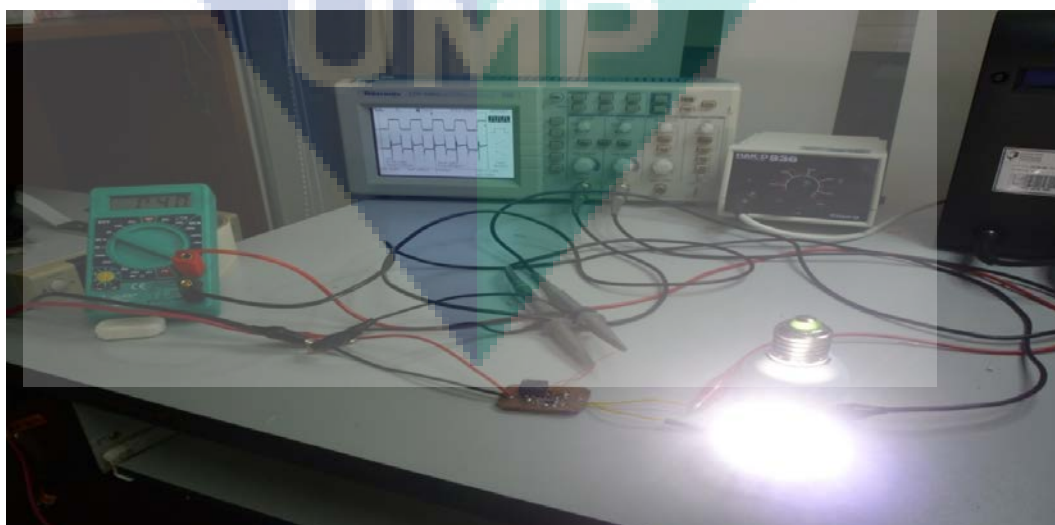
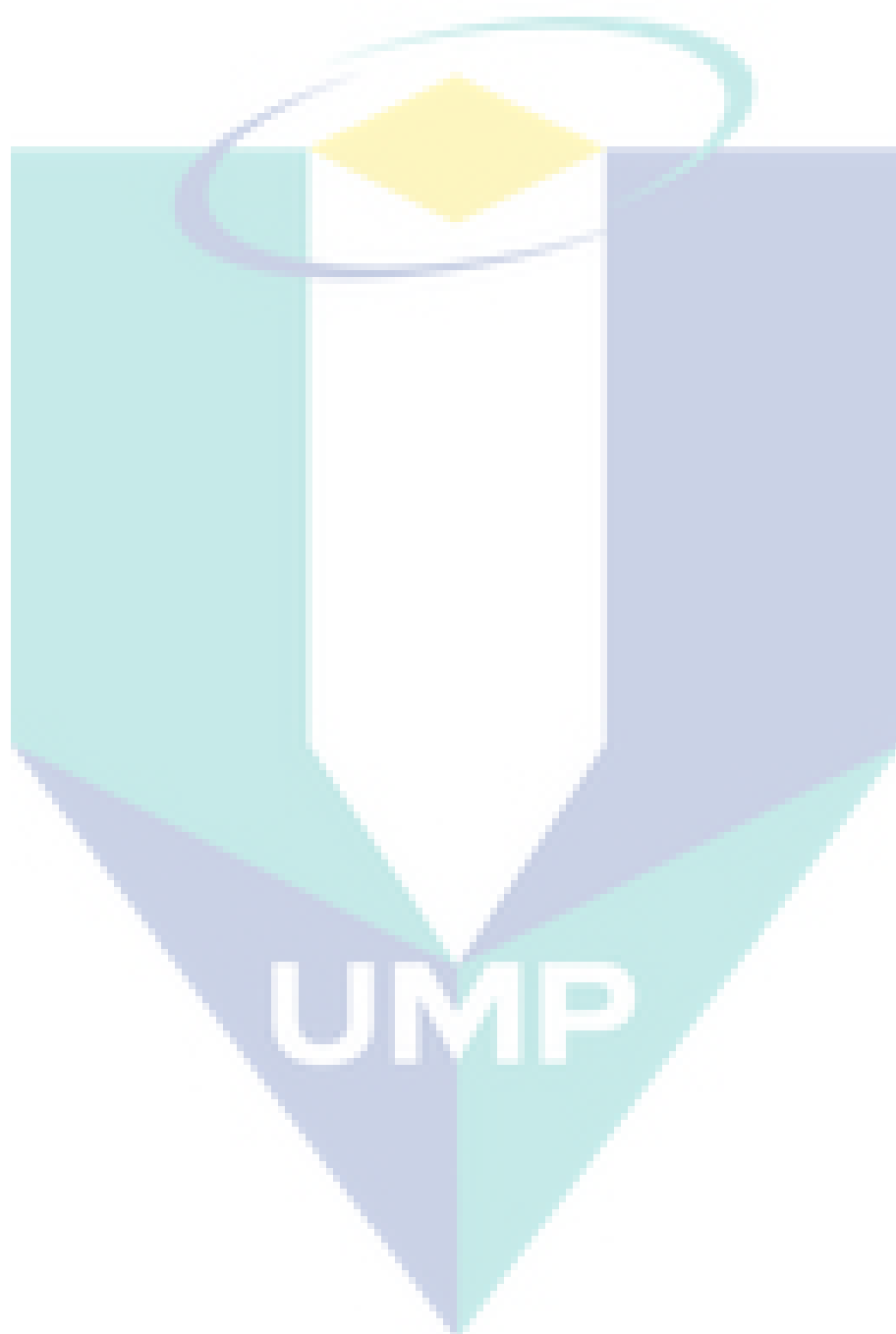
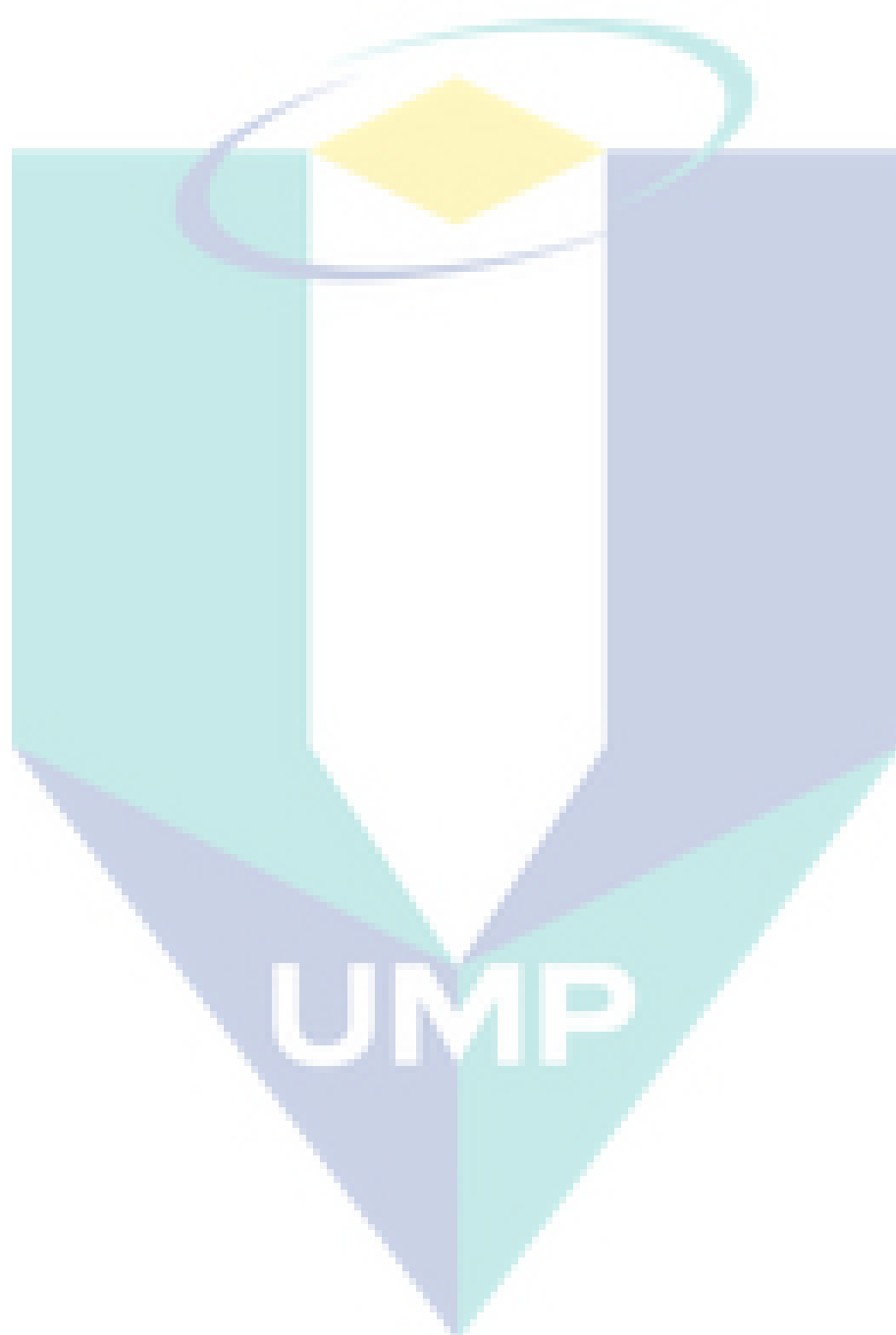
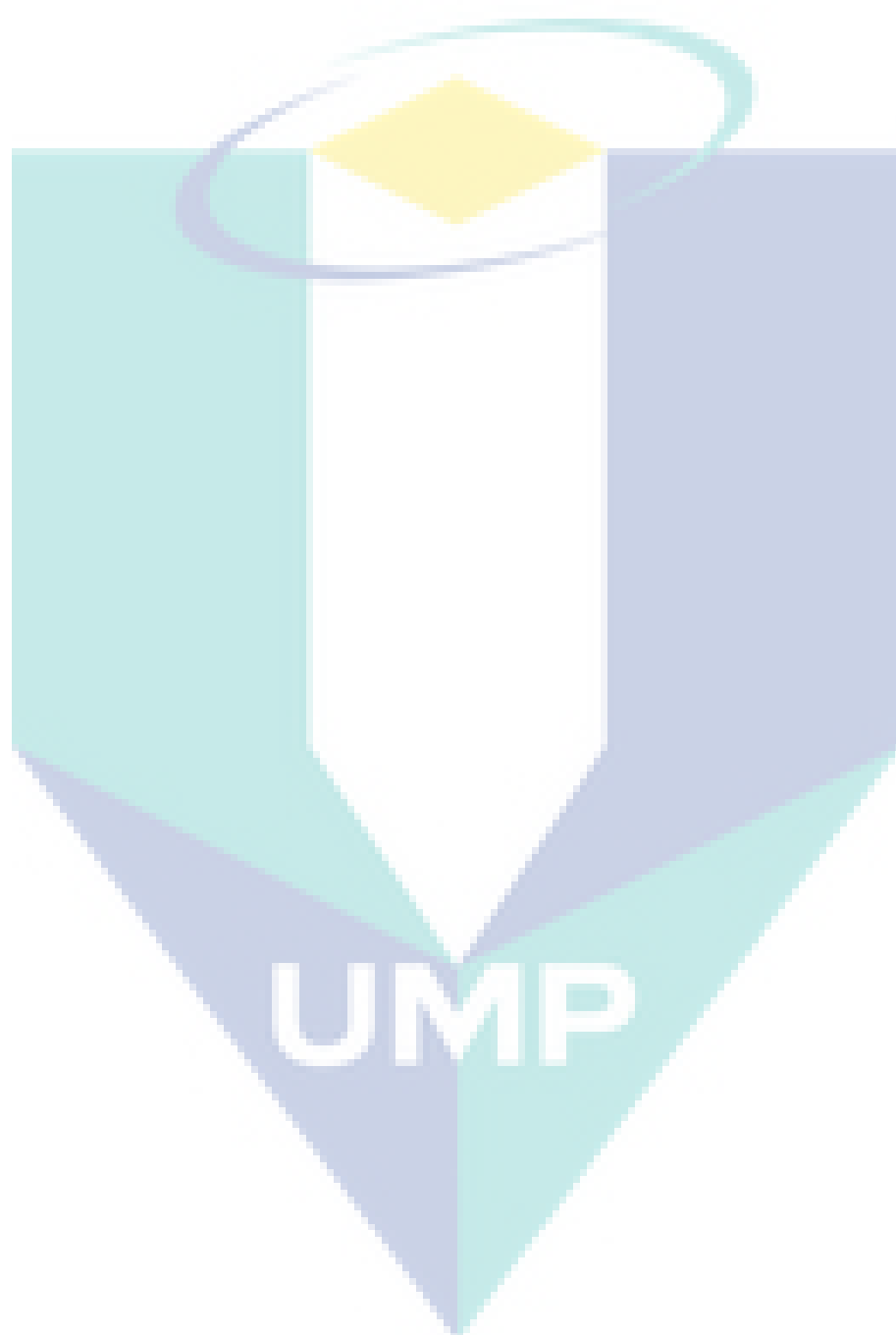


Figure 4.15: Output current







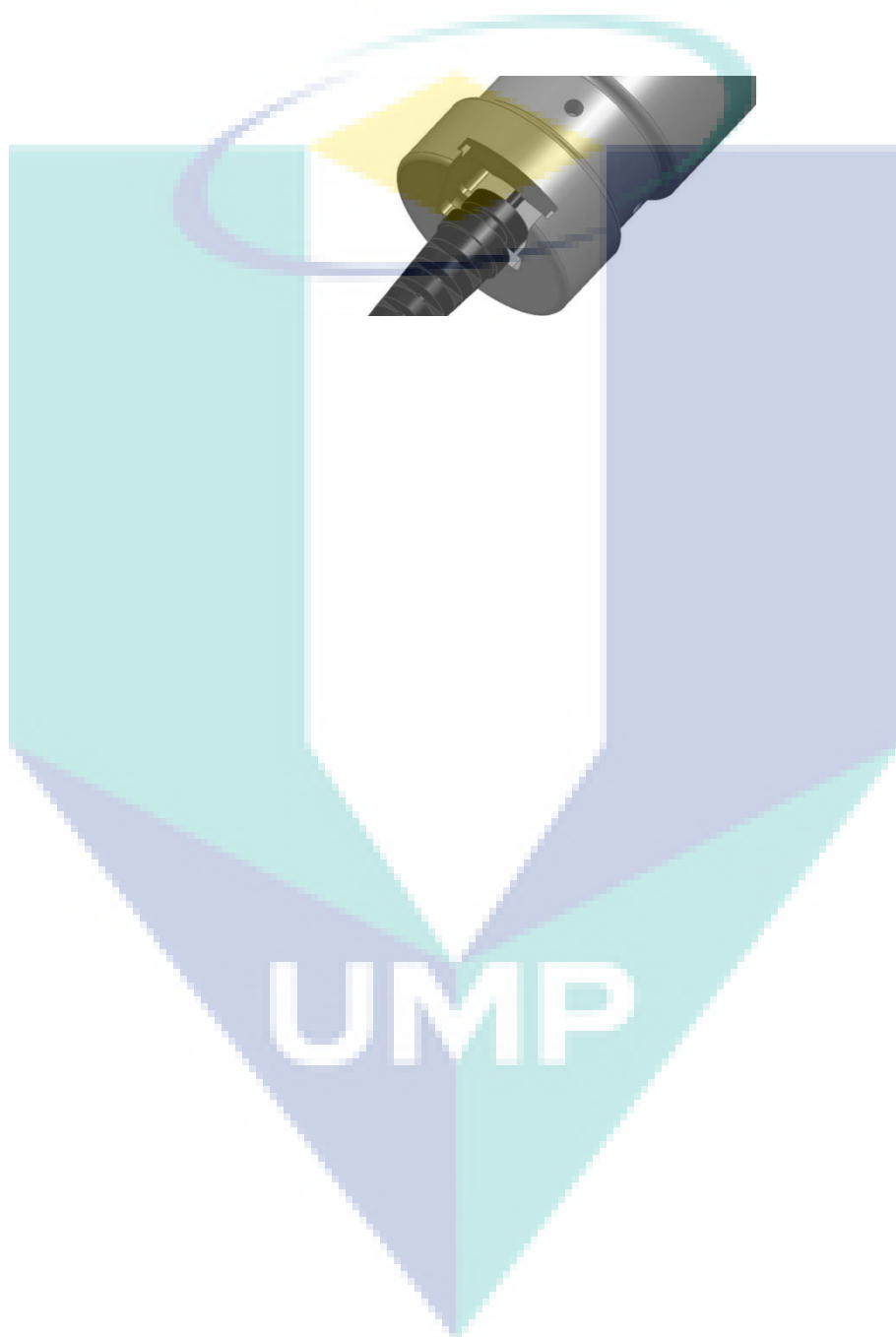




Figure 4.16: Hardware design

Figure 4.16: Design of USB LED Tube

CHAPTER 5

CONCLUSION AND RECOMMENDATION

5.1 Conclusion

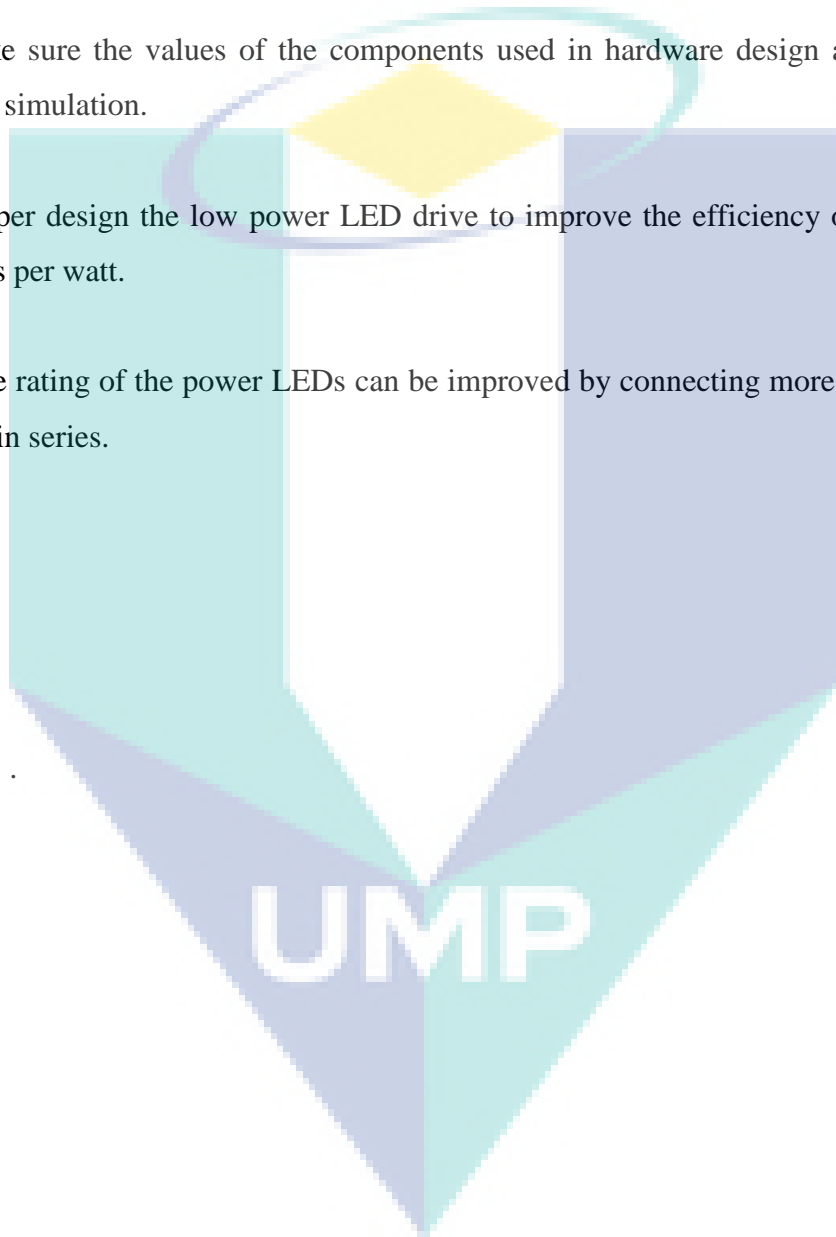
As conclusion, many things that have learned in order to complete this research and the skills of software of PSpice and LTspice have been explored well. PSpice and LTspice software are used widely in investigating and design project for boost converter in order to determine if the circuit meets the design criteria. In the current mode PWM controller, the loop compensator is the important path in the PWM controller design and overall boost converter design. The loop compensator will stabilize the system when some of the parameters in the design circuit are changed. Since the simulation of Current Mode Control for Boost Converter well done by using PSpice and LTspice during this project.

In this project, a current mode PWM controlled boost converter is made for the power LEDs application. The design example can be used as a guide in order to build a real hardware design. For a power LEDs driver, it consists of two main circuits which are power stage and PWM controller. For the low voltage application, the boost topology is selected as the driver. There are two modes of control in the PWM controller. Voltage mode control and Current mode control. Due to the more advantages of the current mode control, a current mode PWM controller is designed by using LTC 3783.

5.2 Recommendation

In the chapter, it was discussed about the limitations of the design. There are recommendation can be used to improve the design circuit:-

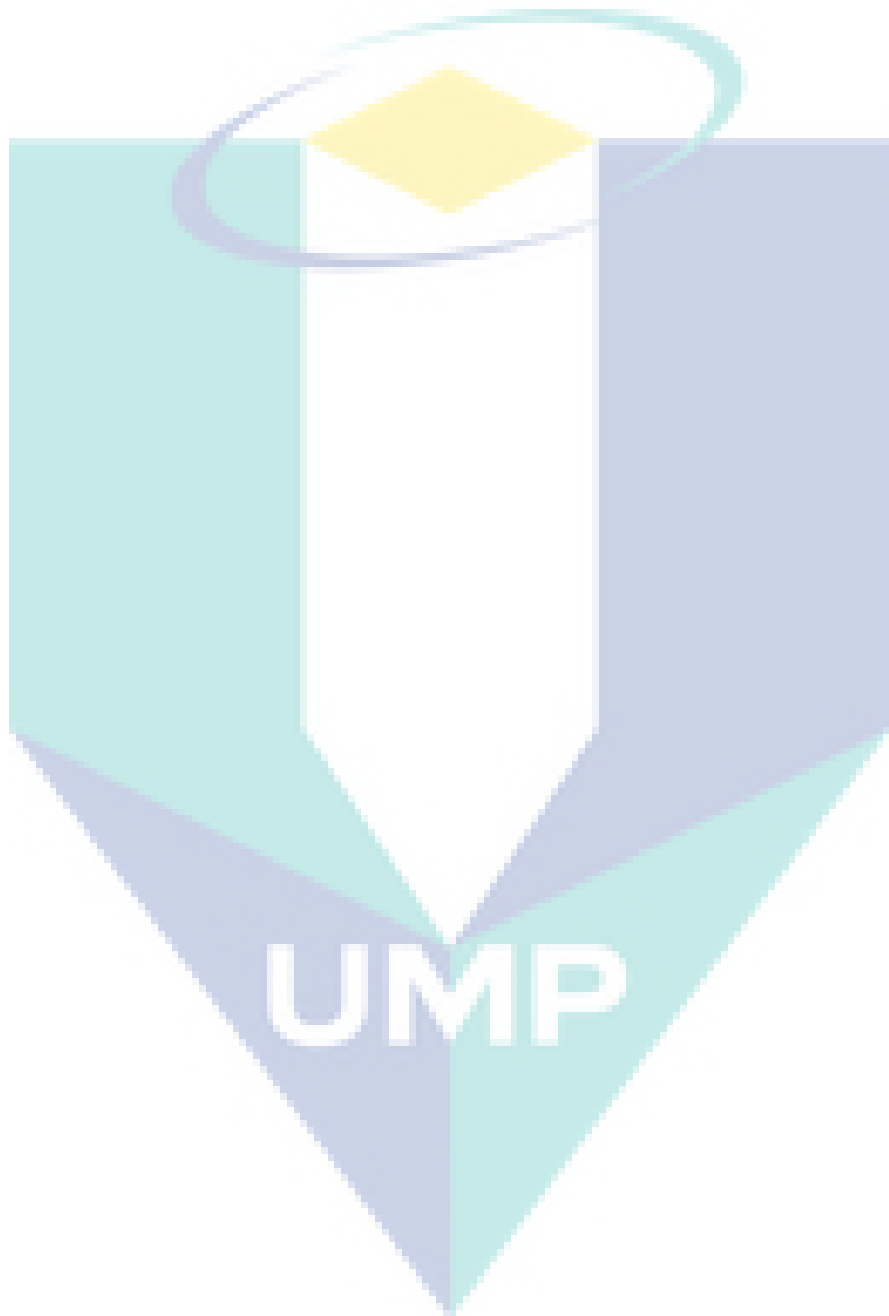
- i. Make sure the values of the components used in hardware design are closed to the design simulation.
- ii. Proper design the low power LED drive to improve the efficiency of LED driver in lumens per watt.
- iii. The rating of the power LEDs can be improved by connecting more strings of power LEDs in series.

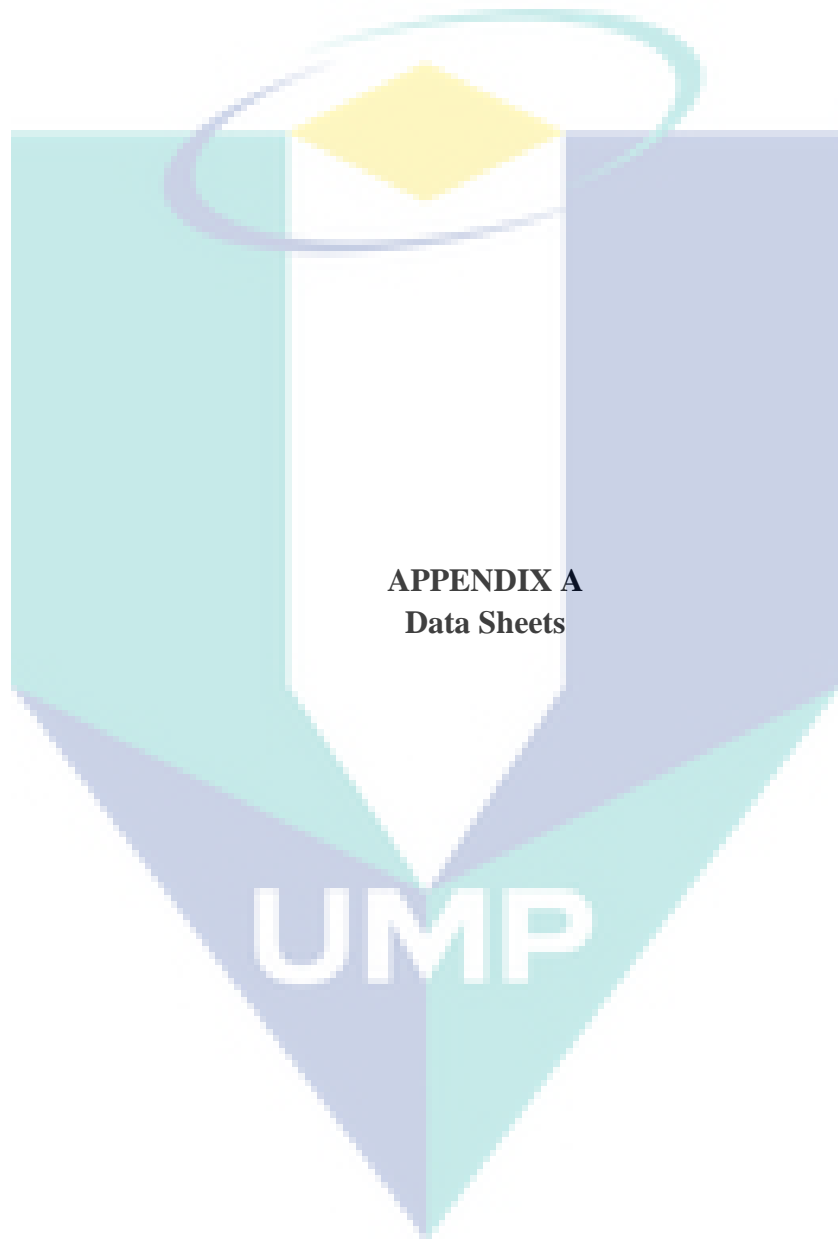


REFERENCES

- [1] Pakpoom Chansri, Nongnuch Noicharoen And Kritsada Phetphoi. “*A High Power LED Driver With Class D ZVS Series Resonant Converter*”. International Conference On Electrical, Control And Computer Engineering. Pahang, Malaysia. June 21-22, 2011
- [2] Tom Ribarich. “*LED professional Review*”. Jan/Feb 2009 ;www.led-professional.com
- [3] Keith Curti. “*Buck Configuration High-Power LED Driver*”. Microchip Technology Inc. 2006
- [4] Barbara Haldeman, Wendell A. Porter, Kathleen C. Ruppert, And Randall A. Cantrell. “*Energy Efficient Homes: Introduction To LED Lighting*”. University Of Florida, Gainesville
- [5] Abdul Ghafar Bin Mat Husin, “*Solar Street Light Using Led Lighting*” 27 April 2010
- [6] Lloyd Dixon. “*Average Current Mode Control of Switching Power Supplies*”. www.ti.com/lit/an/slva079/slva079.pdf
- [7] Yap Kian Guan.” *Current Mode Pwm Controlled Boost Converter For Power Leds Application*”. 21 April 2010
- [8] Gordon Routledge.”*Lighting The Way To A Low-Energy Future*” Iee Review September 2002

- [9] D. Gacio, A.J. Calleja, J. García, J. Ribas And M. Rico-Secades.” *Suitable Switching Converter Topologies For Automotive Signal Lamps And Headlamps Using Power Leds*”. Electrical Engineering Department Universidad De Oviedo.Gijon, Spain. Ieee 2008
- [10] NLPIP Lighting Answers, Vol. 7, Issue 3, May 2003
<http://www.lrc.rpi.edu/programs/nlpip/lightingAnswers/led/whatIsAnLED.asp>
- [11] Muhammad H. Rashid, “*Power Electronics Handbook* ”2001
- [12] Rongfeng Guen, Dalei Tian,Xing Wang. “*Design and Implementation of LED Daylight Lamp Lighting System*”. Journal of International Conferenceon Electronic Packaging Technology & High Density Packaging.2008
- [13] S.W. Ricky Lee, Rong Zhang, Wai Lok Leung. “*Solid State Light Tube with Periodic Units of Lateral-Emitting LEDs*”. Journal of Electronic Components and Technology Conference, 673-678.2008
- [14] D. W. Hart, “*Introduction To Power Electronics*”, Prentice Hall International
- [15] Robert W. Erickson, “*DC-DC Power Converters*”, Article in Wiley Encyclopedia of Electrical and Electronics Engineering
- [16] LU Jiaying and WU Xiaobo, “*A Novel Multiple Modes PWM Controller for LEDs*”,Zhejiang University, 2009.
- [17] Bengt Johansson “*Improved Models for DC-DC Converters*” Lund University, Department of Industrial Electrical Engineering and Automation.
- [18] Dr. Ray Ridley, “*A More Accurate Current-Mode Control Mode*”, Ridley Engineering, Inc.





APPENDIX A
Data Sheets

UMP



LTC3783

PWM LED Driver and Boost,
Flyback and SEPIC Controller

FEATURES

- True Color PWM™ Delivers Constant Color with 3000:1 Dimming Ratio
- Fully Integrated Load FET Driver for PWM Dimming Control of High Power LEDs
- 100:1 Dimming from Analog Inputs
- Wide FB Voltage Range: 0V to 1.23V
- Constant Current or Constant Voltage Regulation
- Low Shutdown Current: $I_Q = 20\mu A$
- 1% 1.23V Internal Voltage Reference
- 2% RUN Pin Threshold with 100mV Hysteresis
- Programmable Operating Frequency (20kHz to 1MHz) with One External Resistor
- Synchronizable to an External Clock Up to $1.3f_{OSC}$
- Internal 7V Low Dropout Voltage Regulator
- Programmable Output Overvoltage Protection
- Programmable Soft-Start
- Can be Used in a No R_{SENSE} ™ Mode for $V_{DS} < 36V$
- 16-Lead DFN and TSSOP Packages

APPLICATIONS

- High Voltage LED Arrays
- Telecom Power Supplies
- 42V Automotive Systems
- 24V Industrial Controls
- IP Phone Power Supplies

LT, LTC and LTM are registered trademarks of Linear Technology Corporation. True Color PWM and No R_{SENSE} are trademarks of Linear Technology Corporation. All other trademarks are the property of their respective owners.

DESCRIPTION

The LTC®3783 is a current mode LED driver and boost, flyback and SEPIC controller that drives both an N-channel power MOSFET and an N-channel load PWM switch. When using an external load switch, the PWMIN input not only drives PWMOUT, but also enables controller GATE switching and error amplifier operation, allowing the controller to store load current information while PWMIN is low. This feature (patent pending) provides extremely fast, true PWM load switching with no transient overvoltage or undervoltage issues; LED dimming ratios of 3000:1 can be achieved digitally, avoiding the color shift normally associated with LED current dimming. The FBP pin allows analog dimming of load current, further increasing the effective dimming ratio by 100:1 over PWM alone.

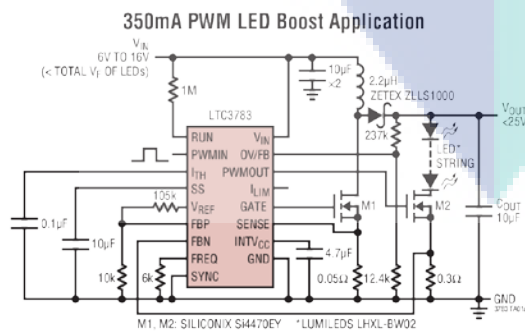
In applications where output load current must be returned to V_{IN} , optional constant current/constant voltage regulation controls either output (or input) current or output voltage and provides a limit for the other. I_{LIM} provides a 10:1 analog dimming ratio.

For low- to medium-power applications, No R_{SENSE} mode can utilize the power MOSFET's on-resistance to eliminate the current-sense resistor, thereby maximizing efficiency.

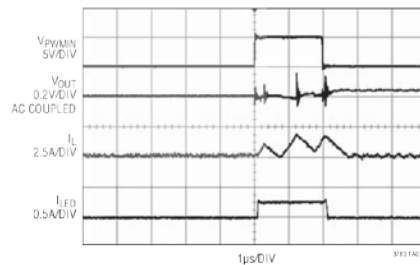
The IC's operating frequency can be set with an external resistor over a 20kHz to 1MHz range and can be synchronized to an external clock using the SYNC pin.

The LTC3783 is available in the 16-lead DFN and TSSOP packages.

TYPICAL APPLICATION



Typical Waveforms

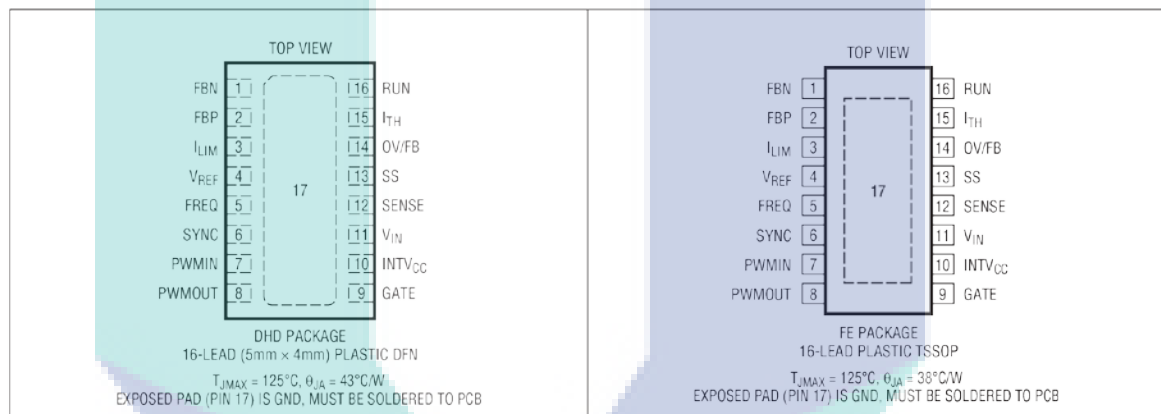


LTC3783

ABSOLUTE MAXIMUM RATINGS (Note 1)

V_{IN} , SENSE, FBP, FBN Voltages	-0.3V to 42V
INTV _{CC} Voltage	-0.3V to 9V
INTV _{CC} Output Current	75mA
GATE Output Current	50mA (RMS)
PWMOUT Output Current	25mA (RMS)
V_{REF} Output Current	1mA
GATE, PWMOUT Voltages	-0.3V to ($V_{INTVCC} + 0.3V$)
I_{TH} , I_{LIM} , SS Voltages	-0.3V to 2.7V
RUN, SYNC, PWMIN Voltages	-0.3V to 7V
FREQ, V_{REF} , OV/FB Voltages	-0.3V to 1.5V

Operating Temperature Range (Note 2)	
LTC3783E	-40°C to 85°C
LTC3783I	-40°C to 125°C
Junction Temperature (Note 3)	-40°C to 125°C
Storage Temperature Range	
DFN Package	-65°C to 125°C
TSSOP Package	-65°C to 150°C
Lead Temperature (Soldering, 10sec)	
TSSOP Package	300°C

PIN CONFIGURATION**ORDER INFORMATION**

LEAD FREE FINISH	TAPE AND REEL	PART MARKING*	PACKAGE DESCRIPTION	TEMPERATURE RANGE
LTC3783EDHD#PBF	LTC3783EDHD#TRPBF	3783	16-Lead (5mm × 4mm) Plastic DFN	-40°C to 85°C
LTC3783IDHD#PBF	LTC3783IDHD#TRPBF	3783	16-Lead (5mm × 4mm) Plastic DFN	-40°C to 125°C
LTC3783EFE#PBF	LTC3783EFE#TRPBF	3783EFE	16-Lead Plastic TSSOP	-40°C to 85°C
LTC3783IFE#PBF	LTC3783IFE#TRPBF	3783IFE	16-Lead Plastic TSSOP	-40°C to 125°C
LEAD BASED FINISH	TAPE AND REEL	PART MARKING*	PACKAGE DESCRIPTION	TEMPERATURE RANGE
LTC3783EDHD	LTC3783EDHD#TR	3783	16-Lead (5mm × 4mm) Plastic DFN	-40°C to 85°C
LTC3783IDHD	LTC3783IDHD#TR	3783	16-Lead (5mm × 4mm) Plastic DFN	-40°C to 125°C
LTC3783EFE	LTC3783EFE#TR	3783IFE	16-Lead Plastic TSSOP	-40°C to 85°C
LTC3783IFE	LTC3783IFE#TR	3783IFE	16-Lead Plastic TSSOP	-40°C to 125°C

Consult LTC Marketing for parts specified with wider operating temperature ranges. *The temperature grade is identified by a label on the shipping container.

For more information on lead free part marking, go to: <http://www.linear.com/leadfree/>

For more information on tape and reel specifications, go to: <http://www.linear.com/tapeandree/>

ELECTRICAL CHARACTERISTICS

The ● denotes the specifications which apply over the full operating temperature range, otherwise specifications are $T_A = 25^\circ\text{C}$. $V_{IN} = 12\text{V}$, $V_{RUN} = 1.5\text{V}$, $V_{SYNC} = 0\text{V}$, $V_{FBP} = V_{REF}$, $R_T = 20\text{k}$, unless otherwise specified.

SYMBOL	PARAMETER	CONDITIONS	MIN	TYP	MAX	UNITS
Main Control Loop/Whole System						
V_{IN}	Input Voltage Range		3		36	V
I_Q	Input Voltage Supply Current	(Note 4)				
	Continuous Mode	$V_{OV/FB} = 1.5\text{V}$, $V_{ITH} = 0.75\text{V}$		1.5		mA
	Shutdown Mode	$V_{RUN} = 0\text{V}$		20		μA
V_{RUN}^+	Rising RUN Input Threshold Voltage			1.348		V
V_{RUN}^-	Falling RUN Input Threshold Voltage		1.223	1.248	1.273	V
$V_{RUN(HYST)}$	RUN Pin Input Threshold Hysteresis			100		mV
I_{RUN}	RUN Pin Input Current			5		nA
$V_{SENSE(MAX)}$	Maximum Current Sense Threshold		125	150	180	mV
$I_{SENSE(ON)}$	SENSE Pin Current (GATE High)	$V_{SENSE} = 0\text{V}$		70		μA
$I_{SENSE(OFF)}$	SENSE Pin Current (GATE Low)	$V_{SENSE} = 36\text{V}$		0.2		μA
I_{SS}	Soft-Start Pin Output Current	$V_{SS} = 0\text{V}$		-50		μA
Voltage/Temperature Reference						
V_{REF}	Reference Voltage		● 1.218 1.212	1.230	1.242 1.248	V V
I_{REF}	Max Reference Pin Output Current		0.5			mA
$\Delta V_{REF}/\Delta V_{IN}$	Reference Voltage Line Regulation	$3\text{V} \leq V_{IN} \leq 36\text{V}$		0.002	0.02	%/V
$\Delta V_{REF}/\Delta I_{REF}$	Reference Voltage Load Regulation	$0\text{mA} \leq I_{REF} \leq 0.5\text{mA}$		0.2	1.0	%/mA
T_{MAX}	Overtemperature SD Threshold Rising			165		$^\circ\text{C}$
T_{HYST}	Overtemperature Hysteresis			25		$^\circ\text{C}$
Error Amplifier						
$I_{OV/FB}$	OV/FB Pin Input Current			18	60	nA
$\Delta V_{OV/FB(OV)}$	OV/FB Overvoltage Lockout Threshold	$V_{OV/FB(OV)} - V_{OV/FB(NOM)}$ in % , $V_{FBP} \leq V_{REF}$		7		%
$V_{OV/FB(FB)}$	OV/FB Pin Regulation Voltage	$2.5\text{V} < V_{FBP} < 36\text{V}$	1.212	1.230	1.248	V
I_{FBP} , I_{FBN}	Error Amplifier Input Current	$0\text{V} \leq V_{FBP} \leq V_{REF}$ $2.5\text{V} < V_{FBP} < 36\text{V}$		-0.4 50		μA μA
$V_{FBP} - V_{FBN}$	Error Amplifier Offset Voltage (Note 5)	$0\text{V} \leq V_{FBP} \leq V_{REF}$ $2.5\text{V} < V_{FBP} \leq 36\text{V}$ ($V_{ILIM} = V_{REF}$) $2.5\text{V} < V_{FBP} \leq 36\text{V}$ ($V_{ILIM} = 0.123\text{V}$)	-3	100 10	3	mV mV mV
g_m	Error Amplifier Transconductance	$V_{FBP} \leq V_{REF}$ $2.5\text{V} < V_{FBP} < 36\text{V}$		1.7 14		mmho mmho
A_{VOL}	Error Amplifier Open-Loop Gain		500			V/V
Oscillator						
f_{OSC}	Oscillator Frequency	$R_{FREQ} = 20\text{k}\Omega$	250	300	350	kHz
	Oscillator Frequency Range		20		1000	kHz
D_{MAX}	Maximum Duty Cycle		85	90	97	%
f_{SYNC}/f_{OSC}	Recommended Max SYNC Freq Ratio	$f_{OSC} = 300\text{kHz}$ (Note 6)		1.25	1.3	
$t_{SYNC(MIN)}$	SYNC Minimum Input Pulse Width	$V_{SYNC} = 0\text{V}$ to 5V		25		ns
$t_{SYNC(MAX)}$	SYNC Maximum Input Pulse Width	$V_{SYNC} = 0\text{V}$ to 5V		$0.8/f_{OSC}$		ns
$V_{IH(SYNC)}$	SYNC Input Voltage High Level		1.2			V
$V_{HYST(SYNC)}$	SYNC Input Voltage Hysteresis			0.5		V



New Product

Si2308BDS

Vishay Siliconix

N-Channel 60-V (D-S) MOSFET

PRODUCT SUMMARY			
V _{DS} (V)	R _{DS(on)} (Ω)	I _D (A) ^a	Q _g (Typ.)
60	0.156 at V _{GS} = 10 V	2.3	2.3 nC
	0.192 at V _{GS} = 4.5 V	2.1	

FEATURES

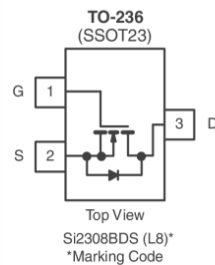
- Halogen-free According to IEC 61249-2-21 Available
- TrenchFET[®] Power MOSFET
- 100 % R_g Tested
- 100 % UIS Tested



RoHS
COMPLIANT
HALOGEN
FREE
Available

APPLICATIONS

- Battery Switch
- DC/DC Converter



Ordering Information: Si2308BDS-T1-E3 (Lead (Pb)-free)
Si2308BDS-T1-GE3 (Lead (Pb)-free and Halogen-free)

ABSOLUTE MAXIMUM RATINGS T _A = 25 °C, unless otherwise noted			
Parameter	Symbol	Limit	Unit
Drain-Source Voltage	V _{DS}	60	V
Gate-Source Voltage	V _{GS}	± 20	
Continuous Drain Current (T _J = 150 °C)	T _C = 25 °C	2.3	A
	T _C = 70 °C	1.8	
	T _A = 25 °C	1.9 ^{b, c}	
	T _A = 70 °C	1.5 ^{b, c}	
Pulsed Drain Current	I _{DM}	8	
Continuous Source-Drain Diode Current	T _C = 25 °C	1.39	
	T _A = 25 °C	0.91 ^{b, c}	
Avalanche Current	I _{AS}	6	
Single-Pulse Avalanche Energy	E _{AS}	1.8	mJ
Maximum Power Dissipation	T _C = 25 °C	1.66	W
	T _C = 70 °C	1.06	
	T _A = 25 °C	1.09 ^{b, c}	
	T _A = 70 °C	0.7 ^{b, c}	
Operating Junction and Storage Temperature Range	T _J , T _{stg}	- 55 to 150	°C

THERMAL RESISTANCE RATINGS

Parameter	Symbol	Typical	Maximum	Unit
Maximum Junction-to-Ambient ^{b, d}	R _{thJA}	90	115	°C/W
Maximum Junction-to-Foot (Drain)	R _{thJF}	60	75	

Notes:

- Based on T_C = 25 °C.
- Surface Mounted on 1" x 1" FR4 board.
- t = 5 s.
- Maximum under Steady State conditions is 130 °C/W.

New Product

Si2308BDS

Vishay Siliconix



MOSFET SPECIFICATIONS $T_J = 25\text{ }^\circ\text{C}$, unless otherwise noted						
Parameter	Symbol	Test Conditions	Min.	Typ.	Max.	Unit
Static						
Drain-Source Breakdown Voltage	V_{DS}	$V_{DS} = 0\text{ V}, I_D = 250\text{ }\mu\text{A}$	60			V
V_{DS} Temperature Coefficient	$\Delta V_{DS}/T_J$	$I_D = 250\text{ }\mu\text{A}$		55		mV/ $^\circ\text{C}$
$V_{GS(th)}$ Temperature Coefficient	$\Delta V_{GS(th)}/T_J$			-5		
Gate-Source Threshold Voltage	$V_{GS(th)}$	$V_{DS} = V_{GS}, I_D = 250\text{ }\mu\text{A}$	1		3	V
Gate-Source Leakage	I_{GSS}	$V_{DS} = 0\text{ V}, V_{GS} = \pm 20\text{ V}$			± 100	nA
Zero Gate Voltage Drain Current	I_{DSS}	$V_{DS} = 60\text{ V}, V_{GS} = 0\text{ V}$			1	μA
		$V_{DS} = 60\text{ V}, V_{GS} = 0\text{ V}, T_J = 55\text{ }^\circ\text{C}$			10	
On-State Drain Current ^a	$I_{D(on)}$	$V_{DS} \geq 5\text{ V}, V_{GS} = 10\text{ V}$	8			A
Drain-Source On-State Resistance ^a	$R_{DS(on)}$	$V_{GS} = 10\text{ V}, I_D = 1.9\text{ A}$		0.130	0.156	Ω
		$V_{GS} = 4.5\text{ V}, I_D = 1.7\text{ A}$		0.160	0.192	
Forward Transconductance ^a	g_{fs}	$V_{DS} = 15\text{ V}, I_D = 1.9\text{ A}$		5		S
Dynamic^b						
Input Capacitance	C_{iss}	$V_{DS} = 30\text{ V}, V_{GS} = 0\text{ V}, f = 1\text{ MHz}$		190		pF
Output Capacitance	C_{oss}			26		
Reverse Transfer Capacitance	C_{riss}			15		
Total Gate Charge	Q_g	$V_{DS} = 30\text{ V}, V_{GS} = 10\text{ V}, I_D = 1.9\text{ A}$		4.5	6.8	nC
				2.3	3.5	
Gate-Source Charge	Q_{gs}	$V_{DS} = 30\text{ V}, V_{GS} = 4.5\text{ V}, I_D = 1.9\text{ A}$		0.8		
Gate-Drain Charge	Q_{gd}			1		
Gate Resistance	R_g	$f = 1\text{ MHz}$	0.6	2.8	5.6	Ω
Turn-On Delay Time	$t_{d(on)}$	$V_{DD} = 30\text{ V}, R_L = 20\text{ }\Omega$ $I_D = 1.5\text{ A}, V_{GEN} = 10\text{ V}, R_G = 1\text{ }\Omega$		4	6	ns
Rise Time	t_r			10	15	
Turn-Off Delay Time	$t_{d(off)}$			10	15	
Fall Time	t_f			7	10.5	
Turn-On Delay Time	$t_{d(on)}$	$V_{DD} = 30\text{ V}, R_L = 20\text{ }\Omega$ $I_D = 1.5\text{ A}, V_{GEN} = 4.5\text{ V}, R_G = 1\text{ }\Omega$		15	23	ns
Rise Time	t_r			16	24	
Turn-Off Delay Time	$t_{d(off)}$			11	17	
Fall Time	t_f			11	17	
Drain-Source Body Diode Characteristics						
Continuous Source-Drain Diode Current	I_S	$T_C = 25\text{ }^\circ\text{C}$			1.39	A
Pulse Diode Forward Current ^a	I_{SM}				8	
Body Diode Voltage	V_{SD}	$I_S = 1.5\text{ A}$		0.8	1.2	V
Body Diode Reverse Recovery Time	t_{rr}	$I_F = 1.5\text{ A}, di/dt = 100\text{ A}/\mu\text{s}, T_J = 25\text{ }^\circ\text{C}$		15	23	ns
Body Diode Reverse Recovery Charge	Q_{rr}			10	15	nC
Reverse Recovery Fall Time	t_a			12		ns
Reverse Recovery Rise Time	t_b			3		

Notes:

- a. Pulse test; pulse width $< 300\text{ }\mu\text{s}$, duty cycle $< 2\%$.
b. Guaranteed by design, not subject to production testing.

Stresses beyond those listed under "Absolute Maximum Ratings" may cause permanent damage to the device. These are stress ratings only, and functional operation of the device at these or any other conditions beyond those indicated in the operational sections of the specifications is not implied. Exposure to absolute maximum rating conditions for extended periods may affect device reliability.



Features

- Available in E12 values
- Inductance as low as 1.0 µH
- Current rating to 9.4 amps
- Lead free
- RoHS compliant*

Applications

- Input/output of DC/DC converters
- Power supplies for:
 - Portable communication equipment
 - Camcorders
 - LCD TVs
 - Car radios

SRR1260 Series - Shielded SMD Power Inductors

Electrical Specifications

Bourns Part No.	Inductance 100 kHz		Q Typ.	Test Frequency (MHz)	SRF Typ. (MHz)	RDC Max. (m.)	I rms Max. (A)	I sat Typ. (A)
	(µH)	Tol. %						
SRR1260-1R0Y	1.0	± 30	26	7.96	100.00	7.8	9.40	10.00
SRR1260-1R2Y	1.2	± 30	18	7.96	91.10	8.0	9.20	9.80
SRR1260-1R5Y	1.5	± 30	24	7.96	86.00	9.5	8.80	9.90
SRR1260-2R2Y	2.2	± 30	22	7.96	70.00	10.5	8.20	8.50
SRR1260-2R4Y	2.4	± 30	18	7.96	63.80	11.5	7.80	8.00
SRR1260-3R3Y	3.3	± 30	20	7.96	40.00	12.0	7.60	7.80
SRR1260-3R5Y	3.5	± 30	22	7.96	37.60	13.0	7.50	7.60
SRR1260-4R7Y	4.7	± 30	19	7.96	36.70	15.5	6.80	7.00
SRR1260-5R6Y	5.6	± 30	19	7.96	33.00	16.2	6.70	6.90
SRR1260-6R1Y	6.1	± 30	21	7.96	29.80	17.0	6.60	6.80
SRR1260-6R8Y	6.8	± 30	20	7.96	28.20	18.0	6.30	6.50
SRR1260-7R6Y	7.6	± 30	16	7.96	27.90	19.0	6.00	6.20
SRR1260-8R2Y	8.2	± 30	18	7.96	24.00	19.5	5.70	5.80
SRR1260-100M	10.0	± 20	32	2.52	21.00	20.0	5.50	5.50
SRR1260-120M	12.0	± 20	27	2.52	19.40	23.0	5.20	5.00
SRR1260-150M	15.0	± 20	25	2.52	17.60	27.0	5.00	4.60
SRR1260-180M	18.0	± 20	28	2.52	15.50	36.0	4.20	3.90
SRR1260-220M	22.0	± 20	29	2.52	13.40	43.0	4.00	3.70
SRR1260-270M	27.0	± 20	26	2.52	12.70	45.0	3.60	3.30
SRR1260-330M	33.0	± 20	27	2.52	9.97	60.0	3.00	2.80
SRR1260-390M	39.0	± 20	22	2.52	10.40	70.0	2.80	2.70
SRR1260-470M	47.0	± 20	22	2.52	7.63	86.0	2.60	2.50
SRR1260-560M	56.0	± 20	24	2.52	7.92	100.0	2.30	2.20
SRR1260-680M	68.0	± 20	22	2.52	7.43	110.0	2.10	2.10
SRR1260-820M	82.0	± 20	25	2.52	6.85	145.0	1.95	1.90
SRR1260-101M	100.0	± 20	26	0.796	6.07	180.0	1.70	1.70
SRR1260-121K	120.0	± 10	26	0.796	5.50	210.0	1.65	1.65
SRR1260-151K	150.0	± 10	20	0.796	5.00	260.0	1.55	1.55
SRR1260-181K	180.0	± 10	26	0.796	4.50	320.0	1.40	1.40
SRR1260-221K	220.0	± 10	22	0.796	4.20	380.0	1.38	1.30
SRR1260-271K	270.0	± 10	20	0.796	3.60	450.0	1.30	1.20
SRR1260-331K	330.0	± 10	22	0.796	3.20	580.0	1.15	1.10
SRR1260-391K	390.0	± 10	20	0.796	2.80	700.0	1.08	1.00
SRR1260-471K	470.0	± 10	18	0.796	2.60	820.0	0.95	0.90
SRR1260-561K	560.0	± 10	22	0.796	2.40	1000.0	0.88	0.80
SRR1260-681K	680.0	± 10	18	0.796	2.20	1150.0	0.80	0.75
SRR1260-821K	820.0	± 10	20	0.796	2.00	1500.0	0.73	0.68
SRR1260-102K	1000.0	± 10	30	0.252	1.80	1700.0	0.68	0.60

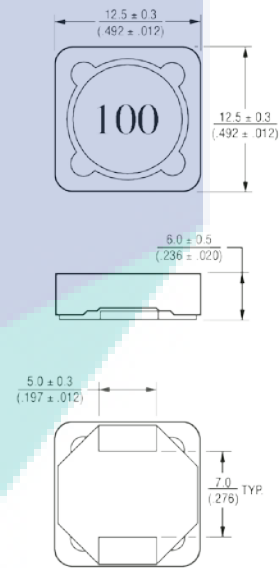
General Specifications

Test Voltage0.1 V
 Reflow Soldering ...230 °C, 50 sec. max.
 Operating Temperature ...-40 °C to +125 °C
 (Temperature rise included)
 Storage Temperature ...-40 °C to +125 °C
 Resistance to Soldering Heat
260 °C for 10 sec.

Materials

CoreFerrite DR and RI
 WireEnameled copper wire 130
 Terminal.....Cu/Ni/Sn
 Rated Current
Ind. drop 25 % typ. at Isat
 Temperature Rise40 °C max.
 at rated Irms
 Packaging600 pcs. per reel

Product Dimensions

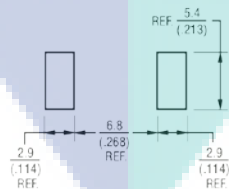


DIMENSIONS: MM (INCHES)

Electrical Schematic



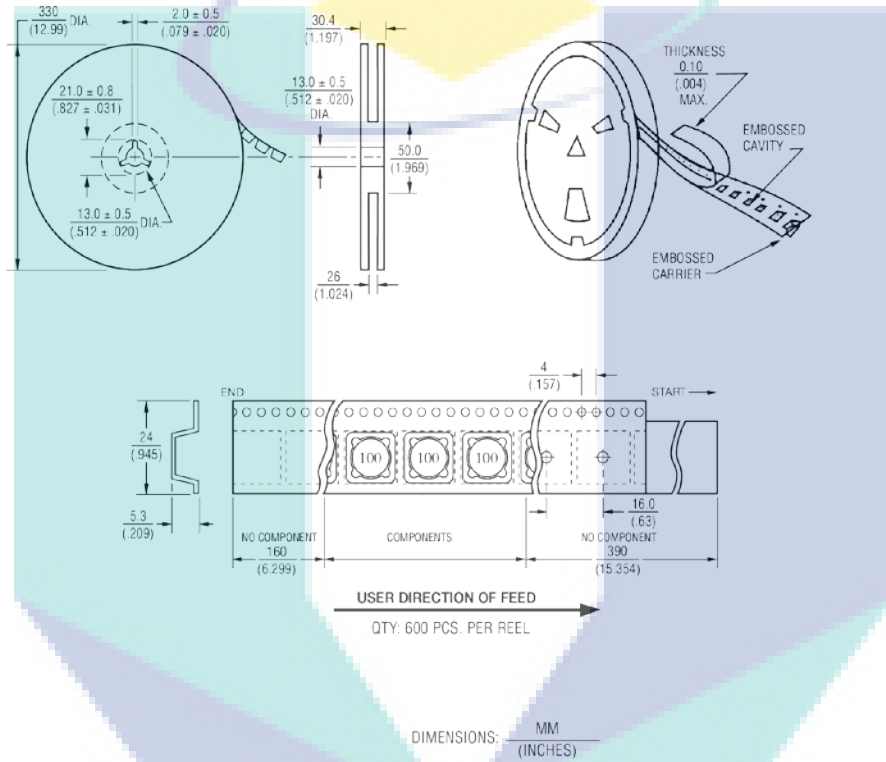
Recommended Layout



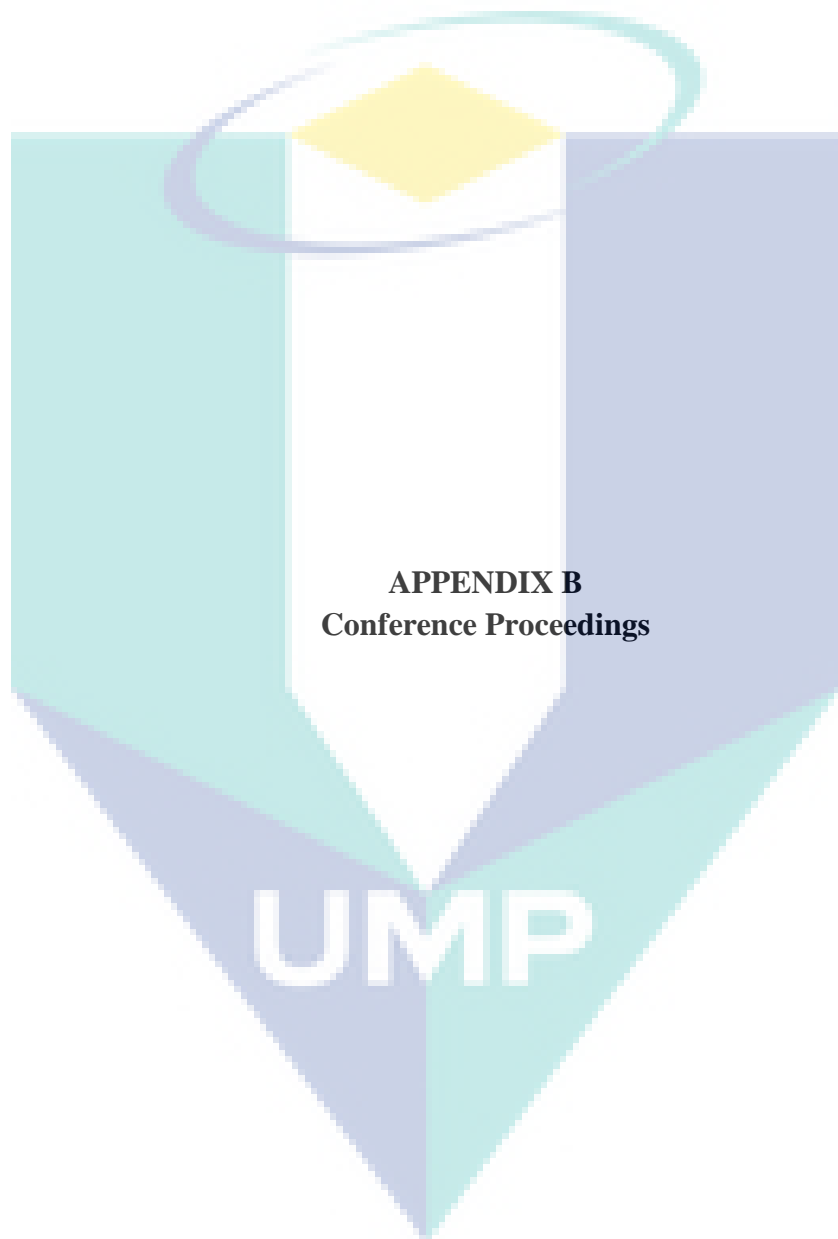
*RoHS Directive 2002/95/EC Jan 27 2003 including Annex
 Specifications are subject to change without notice.
 Customers should verify actual device performance in their specific applications.

SRR1260 Series - Shielded SMD Power Inductors **BOURNS®**

Packaging Specifications



REV. 01/07
 Specifications are subject to change without notice.
 Customers should verify actual device performance in their specific applications.



APPENDIX B
Conference Proceedings

UMP



David Publishing Company

From Knowledge to Wisdom

JOURNAL OF ELECTRICAL ENGINEERING

ISSN 2328-2223

Volume 1, Number 1, December 2013

Journal of Electrical Engineering

Volume 1, Number 1, December 2013 (Serial Number 1)

UMP



David Publishing Company
www.davidpublishing.com

Publication Information:

Journal of Electrical Engineering is published monthly in hard copy (ISSN 2328-2223) by David Publishing Company located at 3592 Rosemead Blvd #220, Rosemead, CA 91770, USA.

Aims and Scope:

Journal of Electrical Engineering, a monthly professional academic journal, covers all sorts of researches on electronics and microelectronics, power engineering, electromagnetism, signal processing, communications and networking, automatic control system, optoelectronics, bioelectrical engineering and other relevant fields.

Editorial Board Members:

Anjan Biswas (USA), Nader Shehata (Egypt), M.G. Vijaya (India), Roumiana Tsankova (Bulgaria), Gurevich Yuri Genriyovich (Mexico), Rainer Dohle (Germany), Radian G. Belu (USA), Ivan Yukhymovych Protsenko (Ukraine), Virginijus Radziukynas (Lithuania), Hoang Van Xiem (Portugal), Yang Gao (China), Waqas Ahmed Imtiaz (Pakistan), Oguzhan Kizilbey (Turkey), Walid Hassan (Lebanon), Vladimir A. Levchenko (Russia)

Manuscripts and correspondence are invited for publication. You can submit your papers via web submission, or E-mail to electrical@davidpublishing.com. Submission guidelines and web submission system are available at <http://www.davidpublishing.com>.

Editorial Office:

3592 Rosemead Blvd #220, Rosemead, CA 91770, USA
Tel: 1-323-984-7526, 323-410-1082; Fax: 1-323-984-7374, 323-908-0457.
E-mail: electrical@davidpublishing.com

Copyright©2013 by David Publishing Company and individual contributors. All rights reserved. David Publishing Company holds the exclusive copyright of all the contents of this journal. In accordance with the international convention, no part of this journal may be reproduced or transmitted by any media or publishing organs (including various websites) without the written permission of the copyright holder. Otherwise, any conduct would be considered as the violation of the copyright. The contents of this journal are available for any citation. However, all the citations should be clearly indicated with the title of this journal, serial number and the name of the author.

Abstracted / Indexed in:

Database of EBSCO, Massachusetts, USA
Cambridge Science Abstracts (CSA)
Chinese Database of CEPS, American Federal Computer Library Center (OCLC), USA
Summon Serials Solutions, USA
China National Knowledge Infrastructure (CNKI), China
Ulrich's Periodicals Directory

Subscription Information:

Price (per year): Print \$520; Online \$320; Print and Online \$600.

David Publishing Company
3592 Rosemead Blvd #220, Rosemead, CA 91770, USA
Tel: 1-323-984-7526, 323-410-1082; Fax: 1-323-984-7374, 323-908-0457.
E-mail: order@davidpublishing.com



David Publishing Company
www.davidpublishing.com

Journal of Electrical Engineering

Volume 1, Number 1, December 2013 (Serial Number 1)

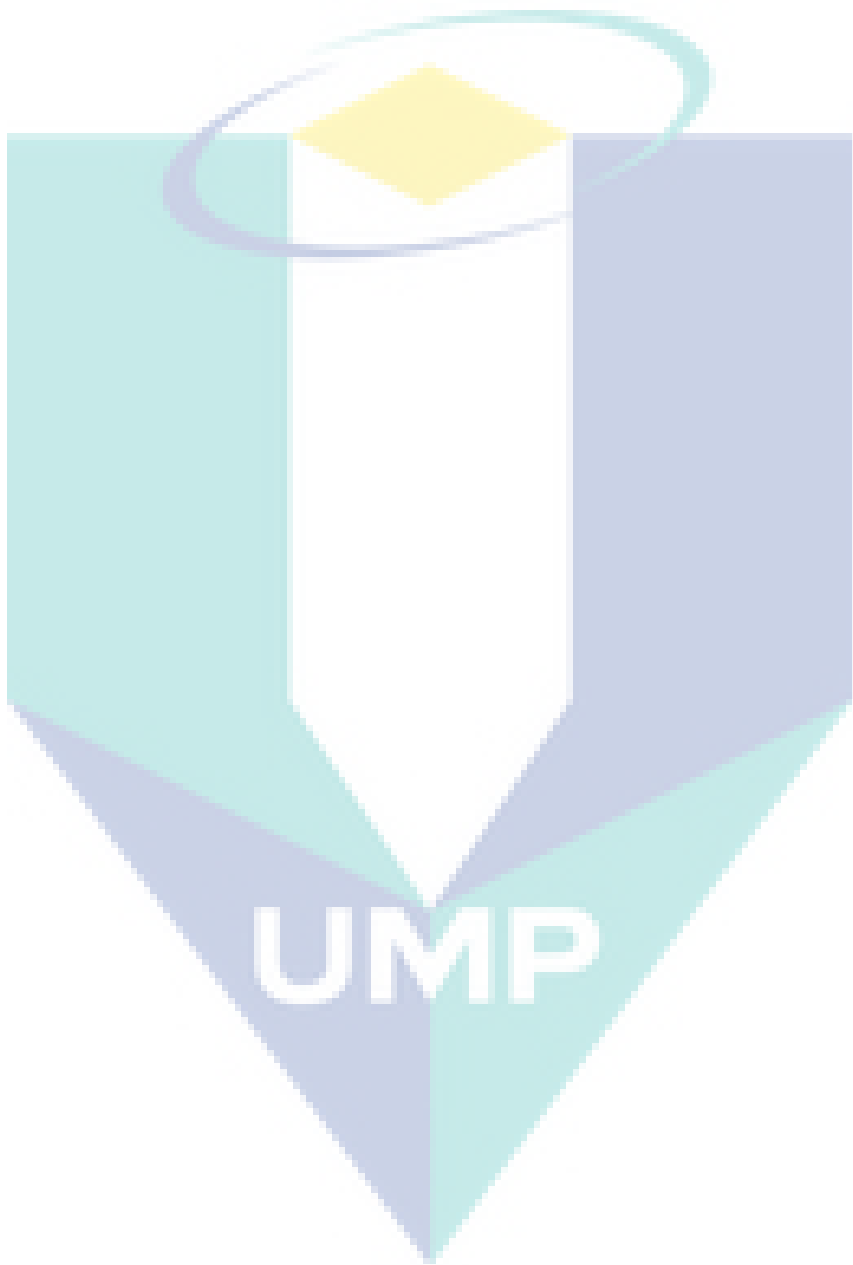
Contents

Techniques and Methods

- 1 **Development of an Accelerated High Resolution Simulation Code for X-Ray Fluorescence Tomography**
Lara Hamawy, Walid Hassan, Stéphane Barre and Samuel Legoupil
- 11 **Discussion on New Metrology Issues of Electricity Energy in Power Line**
Zuliang Lu
- 16 **Development of Low Power LED Driver Using LTSpice Software**
Muhammad Ikram Mohd Rashid, Aim Izzuddin Hakimi Mohamad Bekri, Suliana Ab Ghani, Mudathir Funsho Akorede and Mohd Herwan Sulaiman
- 25 **Fire Detection in Video Sequences Based on Static and Dynamic Features**
Rykhard Bohush, Nadeja Brouka and Sergey Ablameyko

Investigation and Analysis

- 34 **Conductivity and Thermal Properties of PAN Based Polymer Electrolytes for Possible Application in Photo Electrochemical Solar Cells**
Warakawe Jayasundara Mudiyansele Jayabahugedara Saumya Rajinie Jayasundara, Tennakoon Mudiyansele Wijendra Jayalath Bandara, Pierisge Sadeesha Leonard Fernando, Hewage Dhanushka Naleen Sampath Fernando, Malavi Achchi Kankanamge Lakshman Dissanayake, Lekam Ralalage Anura Kalinga Bandara and Bengt-Erik Mellander
- 40 **The Use of EKF to Estimate the Transient Thermal Behaviour of Induction Motor Drive**
Mellah Hacene and Hemsas Kamel Eddine



Development of an Accelerated High Resolution Simulation Code for X-Ray Fluorescence Tomography

Lara Hamawy^{1,2}, Walid Hassan², St éphane Barre¹ and Samuel Legoupil³

1. Geophysical and Industrial Flow Laboratory, Doctoral School of Engineering-Materials Mechanical Energetic Environment Processes Production, Grenoble University, Grenoble 3800, France

2. Department of Biomedical Engineering, School of Engineering, Lebanese International University, Beirut 146404, Lebanon

3. Systems & Technology Integration Laboratory, Atomic Energy Commission, Saclay 91400, France

Received: August 10, 2013 / Accepted: November 19, 2013 / Published: December 25, 2013.

Abstract: X-ray fluorescence tomography is a non-invasive imaging technique based on the acquisition of projections resulting from fluorescent photon emission. Through image reconstruction a slice image is obtained from a series of data collected around the sample. It is really necessary to develop an accelerated high resolution simulation code scheme for X-ray fluorescence tomography. The simulation methods presented in this article are designed to achieve an image reconstruction algorithm. The code, written in C++ and MATALB languages, provides a complete set of tools to perform optimization for the acquisition of fluorescence data. Then, the system is developed and tested to define how an image is reconstructed. A sinogram and a system matrix are established and validated in order to be implemented based on values measured by the detector. Data from various samples of different size, shape and under different conditions can be scanned and derived. Therefore, the carried out simulation code is accurate and offers an important conception of parameter estimation.

Key words: X-ray fluorescence, simulation code, optimization system, image reconstruction, sinogram, probability matrix.

1. Introduction

X-ray fluorescence tomography detects and quantifies the elemental composition of a sample based on the fluorescence data emission (Fig. 1). For better acquisition, optimization of the parameters and settings is needed. This is done first by simulating the technique itself, and then by elaborating a reconstruction system that takes into account the geometrical set-up of the experiment, the probabilities of fluorescence emission and detection, and many physical parameters such as attenuation, scattering and collimation response.

In that context, many research programs are initiated. A simulation code of X-ray imaging techniques was elaborated by Duvauchelle et al. [1]. The geometry of the system to be investigated is defined in StL “Sterio

Lithography: CAD (computer aided design)” format. An initiation file contains data about the object material type, the X-ray source position and spectra and the detector position, size, orientation and resolution [1].

At the same period, an X-ray fluorescence analysis, accomplished by Dietzel, is applied on industrial processes and environmental monitoring. In this study, all factors affecting the fluorescence are considered. The limitation of this technique is that the detector is fixed, there is no rotation then the measurement zone is reduced [2].

In 2007, Loudos established an efficient analytical calculation of probability matrix in two dimension used in SPECT (single photon emission computed tomography) [3].

This article represents a simplified approach of image reconstruction tools and the accomplished work

Corresponding author: Lara Hamawy, Ph.D., research fields: clinical engineering, image processing and signal processing. E-mail: hamawy.lara@gmail.com.

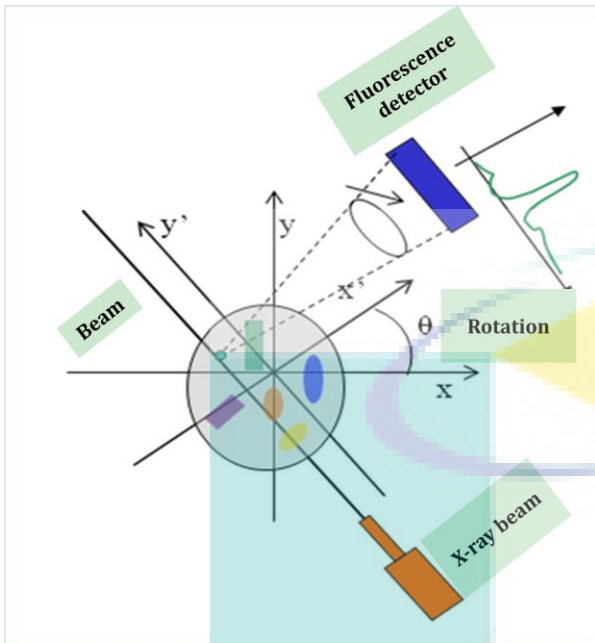


Fig. 1 X-ray fluorescence tomography.

is considered as a fast and deterministic technique. The adopted simulation technique is realized using programming languages along with specific 3-D triangle-mesh modeling editor. This enables complex 3D objects to be drawn and generated in a short time and automatic tomography (rotation, translation) can be performed. First, an imaging technique in which the interaction of X-rays with a complex geometrical object, is simulated in order to optimize the system for better fluorescence acquisition. In addition, the fluorescence quantitative analysis is established to relate the intensity of the emitted fluorescence to the concentration and distribution of the elements inside the sample. The simulation is based on the “ray-tracing technique” and can determine the technical parameters of the measurement system. Then an accurate implementation of the sinogram and the transition matrix, used in X-ray fluorescence tomography, is elaborated.

The proposed simulation code determines the technical parameters of the measurement system in order to perform the data optimization phase and apply an image reconstruction technique. This simulation is not only restricted on identifying the sample. In fact, the physical phenomena of X-ray interaction with

matter in addition to many geometrical and statistical factors are considered and the image reconstruction algorithm is established.

Starting by a background for the system, section 2 describes the physical basics for X-ray fluorescence tomography and image reconstruction elements. The simulation code structure, as a technique and as implementation, is addressed in section 3. Section 4 comprises an experimental validation with the results of the image reconstruction algorithm validation. The last section presents the derived conclusions.

2. Methods

2.1 Attenuation

The attenuation correction is done before and after the fluorescence point. Thus, it depends on the incident energy or wavelength between source-object and on the emitted fluorescence energy between object-object and object-detector.

The absorption correction is based on Beer’s Lambert law:

$$I_{(\lambda)} = I_{0(\lambda)} e^{\sum L(-\mu_{(\lambda)}x)} \quad (1)$$

where, $I_{0(\lambda)}$ is the incident intensity at specific wavelength (s); L is the scanning line or line of response; $\mu_{(\lambda)}$ is the attenuation coefficient corresponding to the source energy or fluorescence energy; x is the distance traveled by the incident beam inside the sample.

Whereas the fluorescence energy depends on the material type and on which atomic shell the fluorescence occurs. It is based on Moseley’s law:

$$E_{KeV} = K(Z - 1)^2 \quad (2)$$

where, Z is the atomic number and K is a constant value of 0.01042 for K -shell; 0.001494 for L -shell and 0.0003446 for M -shell [4].

2.2 Fluorescence Quantitative Analysis

The fluorescence quantitative analysis is established to relate the intensity of the emitted fluorescence to the concentration and distribution of the elements inside the sample. The fluorescence and the number of

photons are evaluated at the level of each voxel inside the sample as follows:

$$P_i = q E_i \rho h C_i \int_{\lambda_0}^{\lambda_{end}} \mu_{\lambda i} I_{\lambda} \quad (3)$$

where, P_i is the fluorescence emitted from each voxel; ρ is the sample element density; h is the sample element size; C_i is the sample element concentration; q is a geometrical factor between source, sample and detector. $\int_{\lambda_0}^{\lambda_{end}} \mu_{\lambda i} I_{\lambda}$ is the summation of the attenuation multiplied by the number of photons arrived and attenuated within each voxel; I_{λ} is the incident intensity (number of photons) interacting inside the element. It is represented by

$$I_{\lambda} = flux \times e^{-\sum \mu_{\lambda i} x_1} \quad (4)$$

where, $flux$ is the incident flux from the X-ray source taking a specific tension at all energies; $\mu_{\lambda i}$ is the element attenuation at a specific wavelength or energy of the source; x_1 is the intersection distance within each element in the sample taking the line between source and sample.

E_i is the fluorescence probability noted by the fluorescence yield.

Concerning the number of photons reaching the detector, the function associated with the intensity of the X-rays interacting in the detector is

$$I_{det} = P_i \times \Omega \times e^{-\sum \mu_{\lambda f} x_2} \quad (5)$$

where, I_{det} is the number of photons arriving at each facet's center of the detector; x_2 is the intersection distance within each element in the sample taking the line between sample and detector; $\mu_{\lambda f}$ is the element attenuation at a specific wavelength or energy of the fluorescence; Ω is the solid angle between the sample and the center of detector facets [2].

2.3 Image Reconstruction

The discrete system components used in reconstruction process is $g = A f$. g represents the vector of projection data which is the sinogram; f , the vector of image data that is updated until an acceptable resolution image is obtained; whereas A is the

reconstruction system matrix, also called the probability matrix.

2.4 Sinogram Creation

Sinogram is the measured data collected around the sample. As shown in Fig. 2, for each angle position (Φ) a projection value is saved on each pixel of the detector. These data are stacked together to form the sinogram.

2.5 Probability Matrix Creation

The probability matrix is denoted by A in the reconstruction model $g = A f$. The unknown image that we are looking for is represented by pixels. What the matrix provides are the probabilities of each photon emitted from these pixels to be detected. Practically another effect interferes which is 'the detector dead area'. For all these reasons, not all the emitted photons from a pixel i in the sample are detected by the bin j of the detector. Therefore, the A_{ij} elements included in the reconstruction process are limited only to those that are actually detected. The remaining is considered non-detected counts. This is expressed by

$$A_{ij} = \frac{\text{photons emitted from pixel } i \text{ detected by bin } j}{\text{photons emitted from pixel } i \text{ totally detected}} \quad (6)$$

Before evaluating the probabilities, we have to set the matrix dimension. The matrix is recognized as a transition matrix as it represents the relationship between values in the slice and in the sinogram.

The matrix element computation is done before the reconstruction procedure. Many techniques are used during implementation of the element calculation. Some

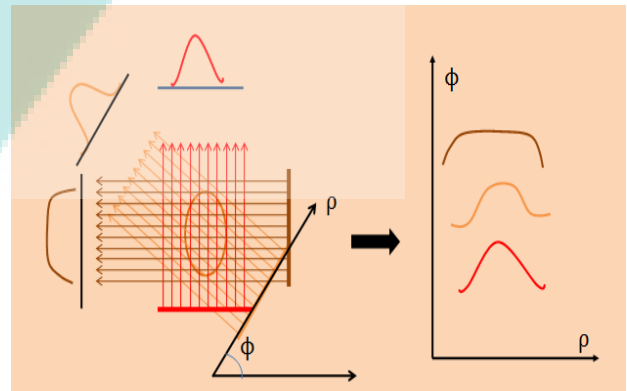


Fig. 2 Sinogram formation.

of them, based on Monte Carlo, require a long computation time. Instead, a technique based on the angle of view and on the geometry of the tomography is used. This is explained in the implementation part [5].

3. Structure of the Code

3.1 The “Ray-Tracing” Technique

“Ray-tracing” technique, which can be considered as an alternative to Monte Carlo, is a deterministic and predictable process. The idea behind is that an image is built by tracing rays of a light beam to a detector and reproduces the path followed by this beam. An amount of computation is needed to express how each ray intersect and interact within an object in its way [6]. Fig. 3 shows an illustration of a ray-tracing application simulated in MATLAB.

3.2 The Stereo-Lithography Format

The “Stereo-Lithography” format or the STL format is used to represent the sample as an object with a 3-dimensional surface geometry.

The surface is decomposed in small triangles called facets. Each facet is described by a normal vector to its surface and by its 3 vertices (points). Twenty numbers are saved to describe each facet. To realize the simulation, all the components (objects) are introduced in STL format [7].

Fig. 4 shows examples of different objects represented in STL format created in C++.

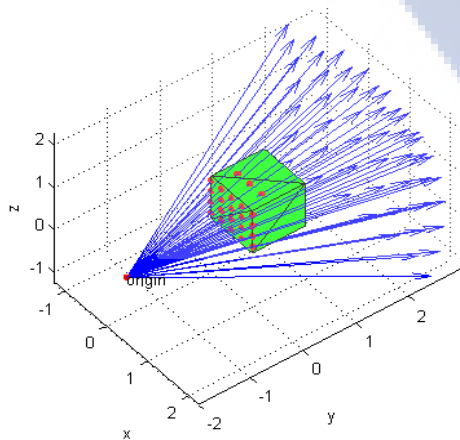


Fig. 3 Ray-tracing technique.

3.3 Implementation

The code is designed such that it starts by reading a data file containing the geometrical characteristics and the technical parameters of all the imaging components: source, sample, collimator and detector. For instance, position, shape, orientation in space and the detector-collimator resolution are all defined during creation. In our experiment the detector and collimator are represented by cubical pixels hence the spatial resolution is the size of the pixels. A 1 hole-collimator or a multi-hole collimator is used by assigning the types of pixel.

It is achieved as stated in Fig. 5.

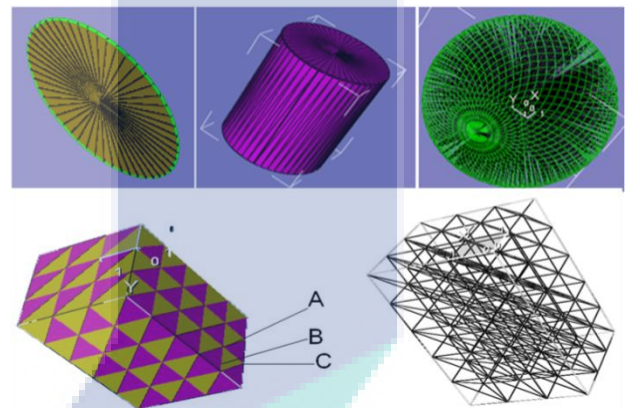


Fig. 4 StL objects showing voxels and facets for a disc, cylinder, sphere and cube.

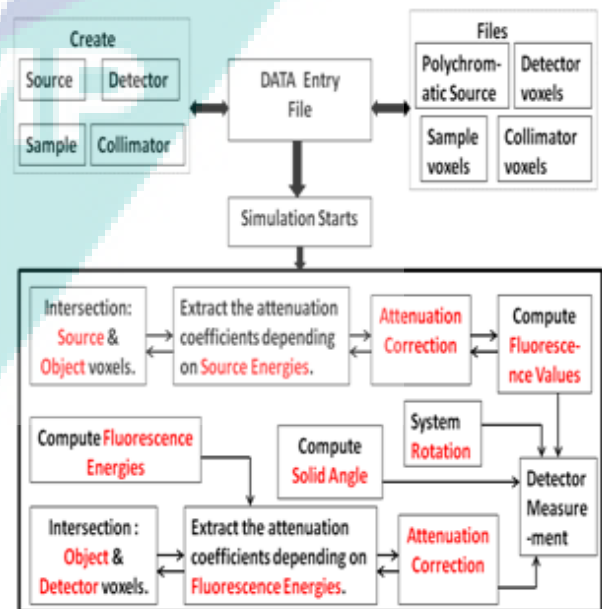


Fig. 5 Simulation code methodology.

The X-ray focal spot is determined by the followed line paths; whereas the intensity and the spectrum loading consist of associating the values at all energies with a specific working tension (ranging between 25 kV to 160 kV).

Besides the definition of tools, the physical phenomenon of X-ray interaction with matter and the data collection are implemented with maximum accuracy.

The simulation code evaluates the intensity of each projection as follows:

- the intensity reaching the voxel;
- the intensity interacting within the voxel;
- the intensity of emitted fluorescence;
- the detected intensity (at the detector level after being collimated) [8].

3.4 Image Reconstruction: Probability Matrix

Once the fluorescence measurements are processed and computed, the probability matrix is established and implemented. Then, a computational reconstruction method is designed to reproduce accurate images.

In the implementation of the probability matrix system, the rows correspond to the detector in all positions angles and the columns depend on the original sample size.

Hence, the system matrix is a large matrix to be stored and manipulated in typical application. Its dimension depends on:

- The number of detector pixels multiplied by the number of projection angles (number of rows);
- The number of pixels which is relevant to the size of the reconstructed image (number of columns).

Note that the sample or the original image is considered as a group of pixels.

For the probabilities general calculation, it is based on the evaluation of the matrix weights. A weight is the probability that a photon emitted in a given voxel contributes to a projection in a given bin on the detector. This principle is illustrated in Fig. 6 where the photons are assumed to be emitted isotropically from each pixel and a linear orbit is considered the path followed by each photon.

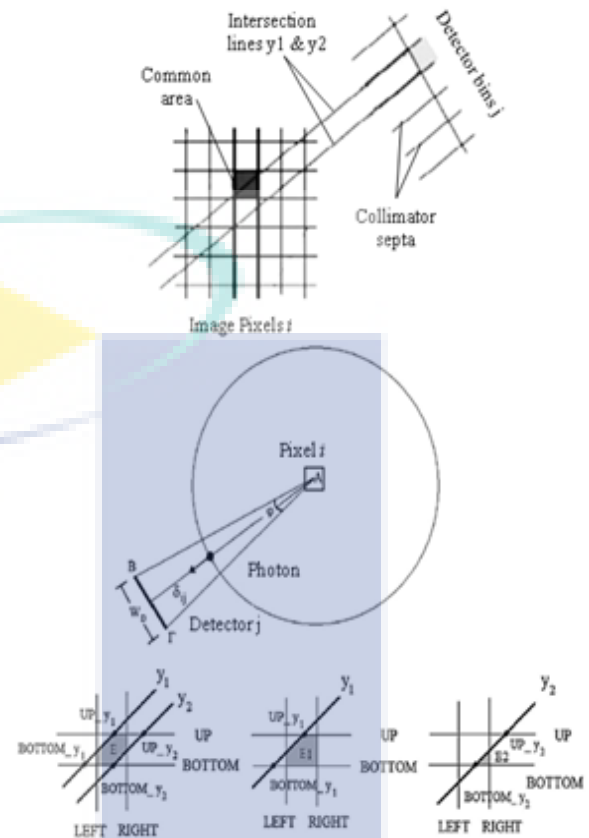


Fig. 6 The geometry of photons emission from pixel i reaching detector bin j [3].

The parameters shown are defined as δ_{ij} : the distance between pixel i and detector j ; W_D : the width of each detector; φ : the solid angle.

As it can be seen in Fig. 6, if a photon is emitted from pixel i the probability that it will be detected by detector j depends on the percentage of the intersection area between this pixel and the “detection zone”.

In order to calculate the elements of this matrix we have to compute the common area.

The arrangement steps are in the Fig. 7.

Note that these steps are done for each pixel of the image with each pixel of the detector at each rotation step.

Based on these geometrical and statistical factors, the probability of fluorescence detection depends on the percentage of the intersection area between each pixel and the detection zone. It is given by

$$E_{\%ij} = \frac{E_1 - E_2}{(W_D Det / \pi \theta \sqrt{N})} \quad (7)$$

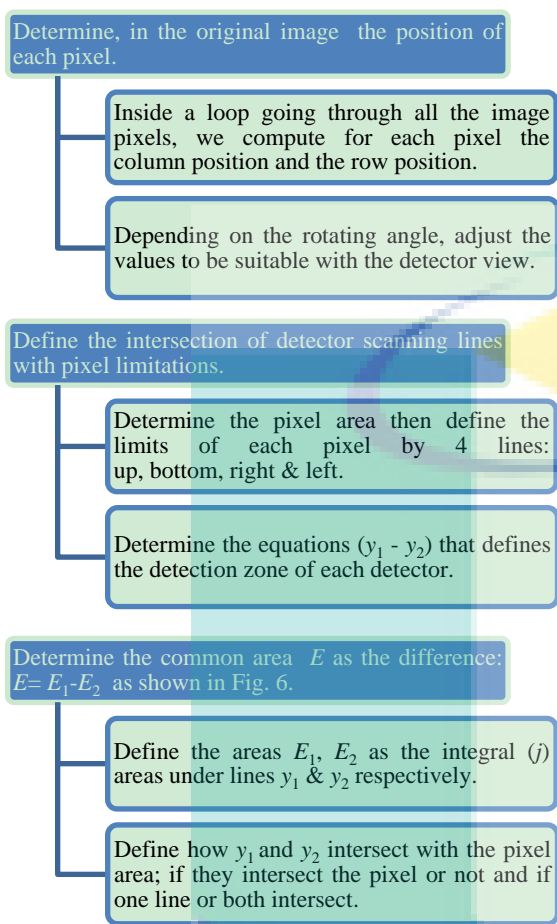


Fig. 7 Implementation steps of a system matrix.

This intersection area is called the emission probability common area $E_{%ij}$. So the probability is derived from what each detector can see.

The term $W_D Det / \pi_\theta \sqrt{N}$ represents “width of the pixel”. It is derived from:

- Det , the total number of detectors in all projections;
- W_D , the detector width;
- π_θ , the number of projection angles;
- N , the total number of image pixels.

The weights or the matrix values are between 0 and 1. It combines the geometrical factor with the probability factor. They are implemented as follows (Fig. 8)

3.5 Implementation

During optimization we find three main settings listed in Fig. 9 to have appropriate fluorescence data and perform the experiments.

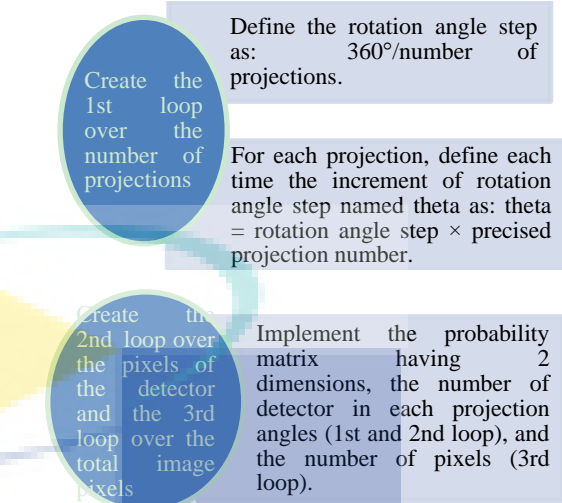


Fig. 8 Simulation steps of a system matrix.

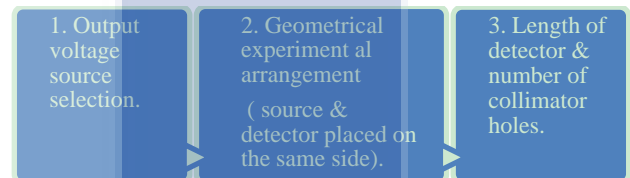


Fig. 9 The most effective settings for optimization.

4. Results and Validation

4.1 Experimental Fluorescence Validation

Using same settings and parameters, “Aluminum”, “Lead” and “Lead immersed in Aluminum” have been used as simulation (the material type is defined by its attenuation coefficient) and as an experimental sample to test the fluorescence emission and attenuation (Fig.10). The experimental fluorescence peaks are displayed in Figs. 11-13. These are the measurements found at certain angles of the detector.

The acquired measurements are compared with simulated results having same settings and parameters.

The results shown in Fig. 14 are close. An error of 8% is estimated; thus the system is reliable and the obtained fluorescence data are able to determine a well-defined image.

4.2 Sinogram Validation

Fig. 15 shows sinograms of 120 projections and of 50 projections for a short detector and long detector simulated in this project.

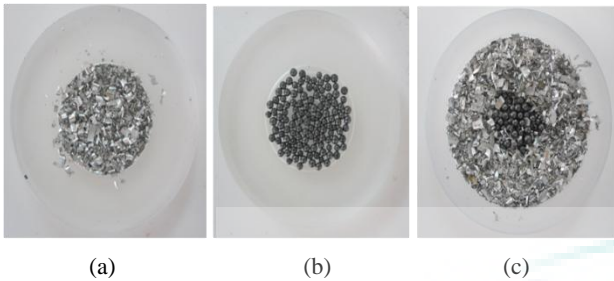


Fig. 10 (a) Aluminum sample; (b) lead sample; (c) lead sample immersed in aluminum.

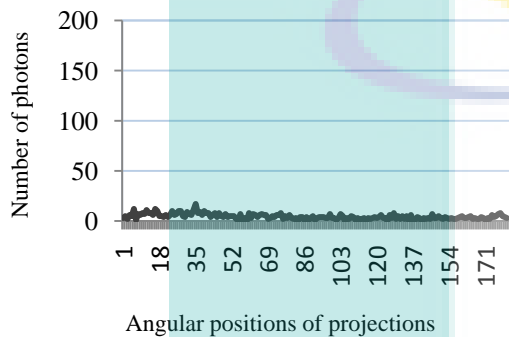


Fig. 11 Fluorescence experimental result of Al sample.

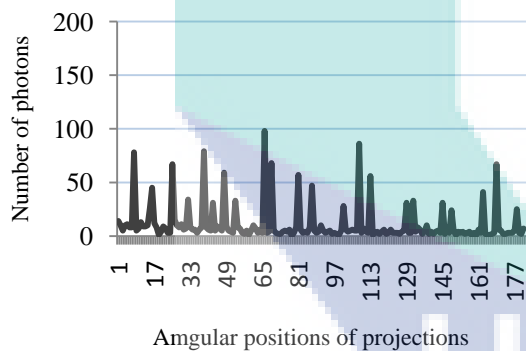


Fig. 12 Fluorescence experimental result of Pb sample.

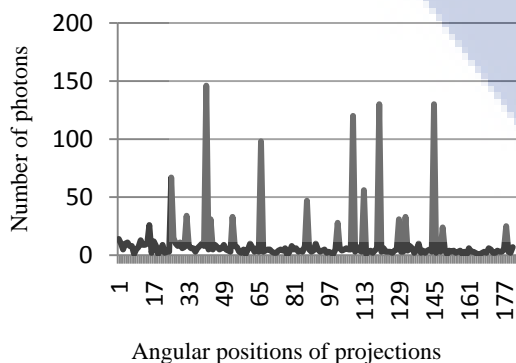


Fig. 13 Fluorescence experimental result of Pb immersed in Al sample.

Fig. 16 displays clearly the accuracy of the generated sinogram when it reflects the number of objects inside the sample.

These two dimensional arrays of projection data are displayed using the MATLAB. The sinogram is considered the input data for image reconstruction.

4.3 Probability Matrix Validation

The first step is to validate “the probability matrix computation” and “the MLEM (maximum likelihood expectation maximization) algorithm implementation”. The procedure is to apply the system on a known shape so that the resulting image is predicted.

The Figs. 17-19 illustrate the obtained result with the implementation steps in below.

A black and white image of known geometrical shapes (sphere and cube) is created in MATLAB.

Radon transform is applied on this image using the Radon function found in MATLAB.

Implement the sinogram resulting from the Radon Transform into the probability matrix function (without collimator) and then in the MLEM function established in the C++ code.

Fig. 17 illustrates the obtained sinogram whereas Figs. 18 and 19 illustrate the obtained reconstructed image by increasing the number of projections and the number of iterations respectively.

4.4 Resolution

In the resolution section, the quality of the reconstructed image is manifested. The spatial resolution is the capability of identifying close objects from each other. The algorithm is applied on three images. The first one is a white square inside a black square (Fig. 20a). In the second image (Fig. 20b) the sides of the white square moved closer to each other then they will be closer to the center. The third image contains squares close to each other (Fig. 20c). The aim is to control how the MLEM algorithm and the applied settings show the center of the square.

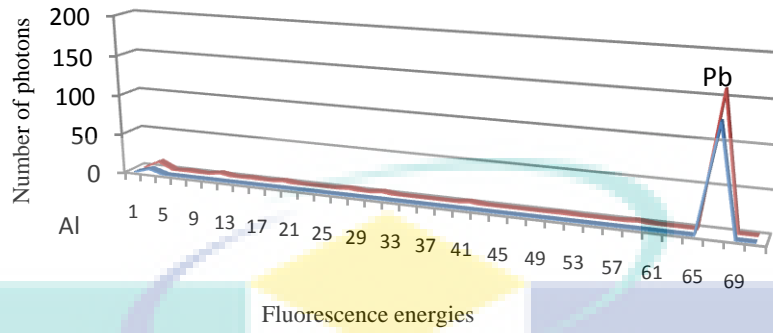


Fig. 14 Comparison between simulated (blue line) and experimental fluorescence (red line).

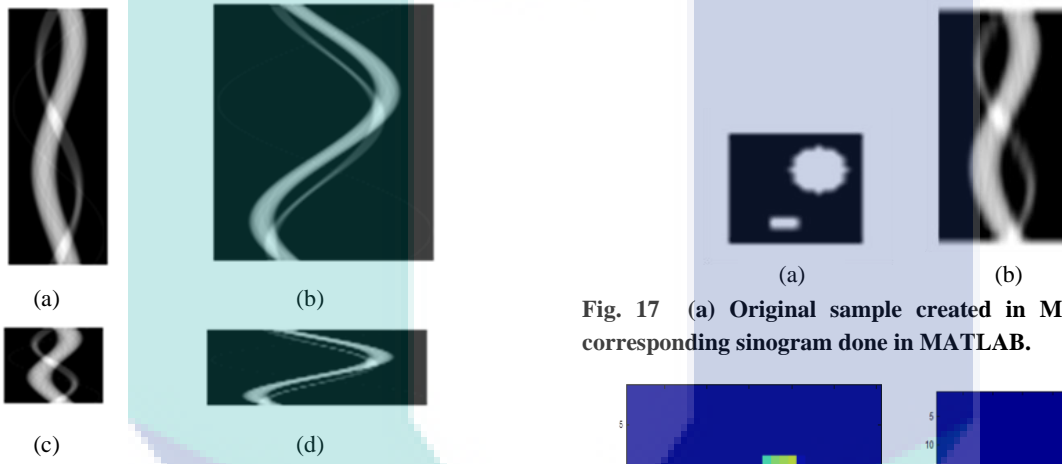


Fig. 15 (a, b) 120 projections; (c, d) 10 projections; (a, d) 20 cm detector; (b, d) 40 cm detector.

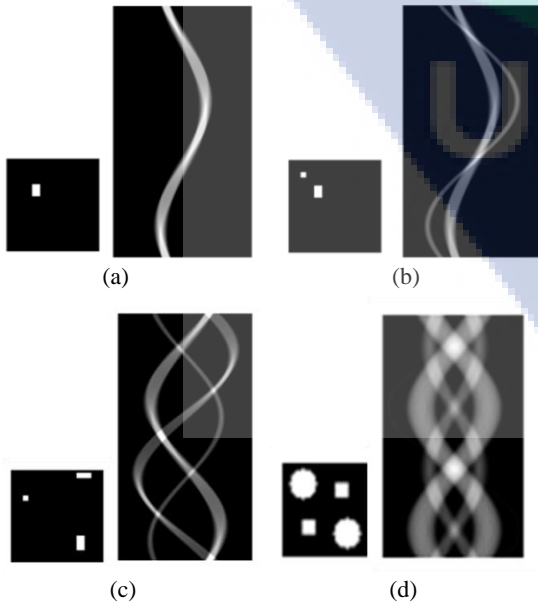


Fig. 16 Sinogram reflecting (a) 1 object; (b) 2 objects; (c) 3 objects; (d) 4 objects.

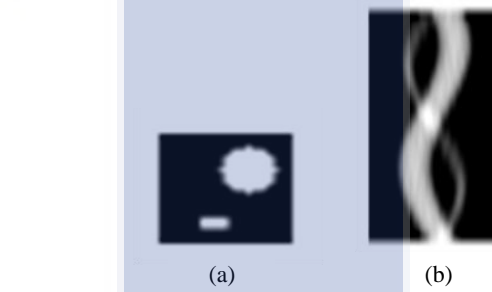


Fig. 17 (a) Original sample created in MATLAB; (b) corresponding sinogram done in MATLAB.

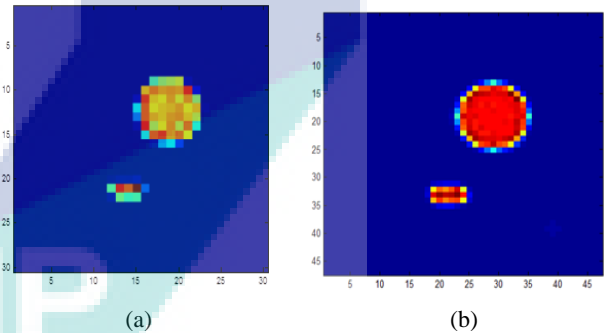


Fig. 18 (a) Reconstructed image in C++ using 18 projections; (b) reconstructed image in C++ using 50 projections.

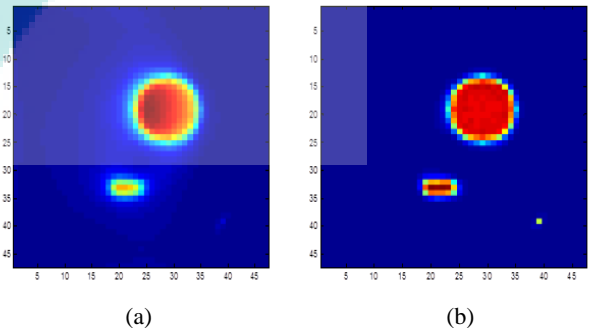


Fig. 19 Reconstructed image using MLEM in (a) 5 iterations are applied; (b) 10 iterations are applied.

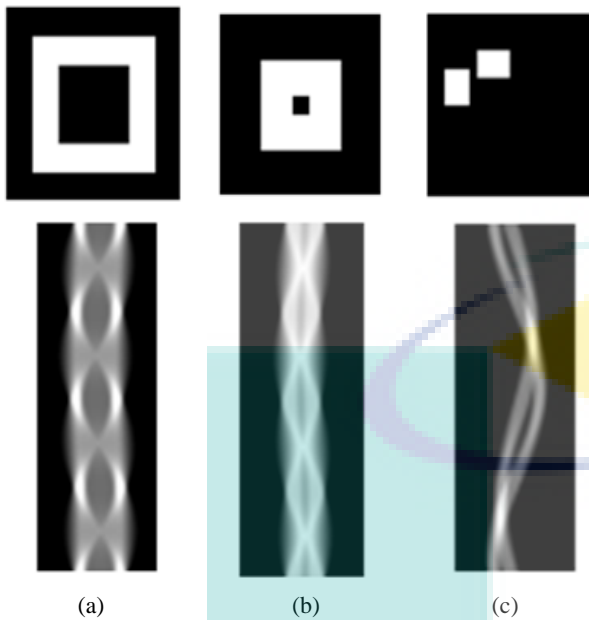


Fig. 20 Original samples and their corresponding sinograms.

The reconstructed image of these boxes, displayed in Fig. 21, is the result of 120 projections and 65 iterations of MLEM. The transition matrix dimensions are of “33 detector pixels \times 120 projections” for the rows and “33 \times 33 as number of pixels” for the columns.

5. Conclusions

Other simulation codes used Monte Carlo technique which is probabilistic and very realistic but it requires longer time and needs powerful computer. On the other hand, even when we have complex samples and in need for multiple interactions, our simulation code based on ray tracing technique has proved effectiveness. At the same time, our resulting images are free of noise.

The developed simulation code extracts from the collected fluorescence measurements the maximum available information. Comparing with experimental data, the obtained results of fluorescence acquisition are reliable. The quality of the reconstructed image relies strongly on the system matrix to be implemented in the chosen reconstruction algorithm. In this work, the sinogram validation proves accuracy and the reconstructed images results have an acceptable resolution of a spatial distribution.

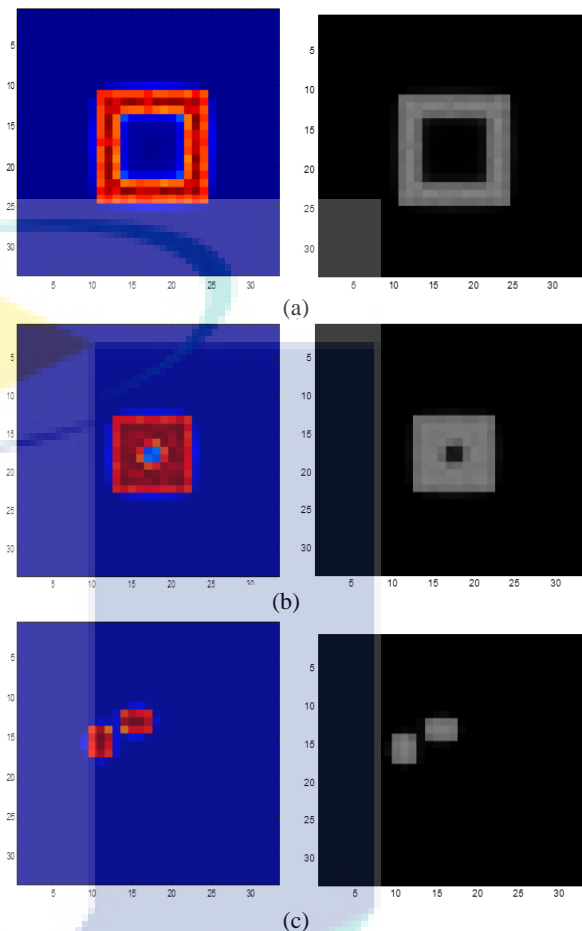


Fig. 21 Reconstructed images through MLEM algorithm.

Acknowledgments

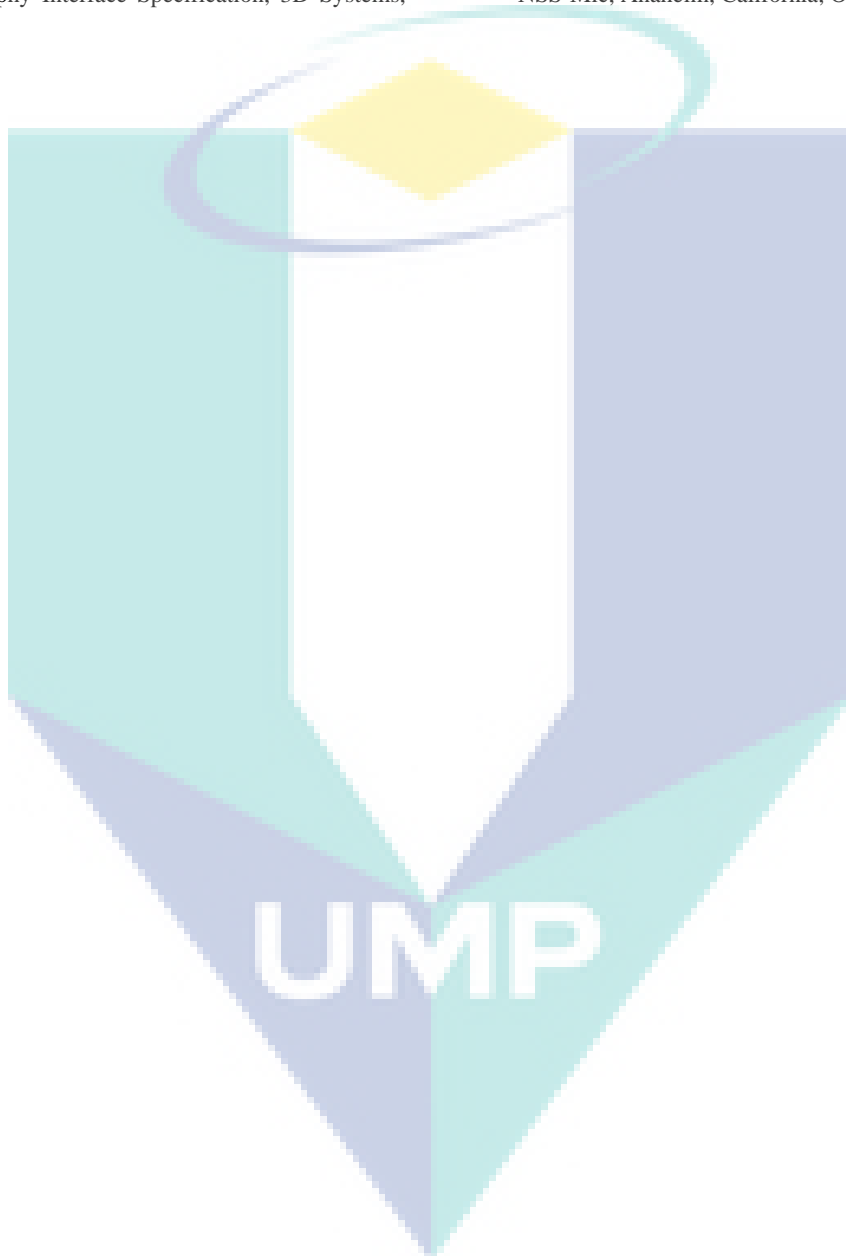
I would like to thank the Lebanese International University (LIU-Lebanon), the Grenoble University (UDG-France) and the Atomic Energy Commission (CEA-Saclay-France) for supporting this project.

References

- [1] P. Duvauchelle, N. Freud, V. Kaftandjian, D. Babot, A computer code to simulate X-ray Imaging technique, Nuclear Instruments and Methods in Physics Research B 170 (2000) 245-258.
- [2] K. Dietzel, On-line X-ray fluorescence analysis applied to industrial processes and environmental monitoring, Ph.D. Dissertation, Dept. Physics, The University of Bergen, Norway, 2000.
- [3] G.K. Loudos, An efficient analytical calculation of probability matrix in 2D SPECT, Comput. Med. Imaging Graph 32 (2) (2008) 83-94.
- [4] P. Sprawls, The physical principles of medical imaging, 2nd ed., Medical Physics Publishing Corporation, USA, 1995.

10 **Development of an Accelerated High Resolution Simulation Code for X-Ray Fluorescence Tomography**

- [5] P. Bruyant, Analytic and iterative reconstruction algorithms in SPECT, *Journal of Nuclear Medicine* 43 (10) (2002) 1343-1358.
- [6] G. Massal, A raytracer in C++, Codermind Team Website, <http://www.codermind.com/articles/Raytracer-in-C++-Introduction-What-is-ray-tracing.html>.
- [7] Stereo lithography Interface Specification, 3D Systems, Inc., Oct. 1989.
- [8] W. Hassan, L. Hamawy, S. Barre, S. Legoupil, Spatial localization of metallic particles in a liquid sample using X-ray fluorescence tomography, in: *IEEE Nuclear Science Symposium and Medical Imaging Conference, High Resolution & Pre-Clinical Imaging Instrumentation, NSS-Mic, Anaheim, California, Oct. 27-Nov. 3, 2012.*



Discussion on New Metrology Issues of Electricity Energy in Power Line

Zuliang Lu

NIM (National Institute of Metrology), Beijing 100013, China

Received: July 21, 2013 / Accepted: September 17, 2013 / Published: December 25, 2013.

Abstract: The existed issues on electricity energy measurement in power line networks are discussed from metrological viewpoint. Several new methods are proposed for verifying the performance specifications of new functions for dynamic measurements and power line communications of smart meters. A concept of “Out Door Communication” is proposed for successful communication in any time. An expectation about high voltage EMC (electromagnetic compatibility) is indicated for quality of electronic transformer.

Key words: Dynamic measurement, power line communication, electronic transformer, smart meter, metrology.

1. Introduction

Smart meter and DR (demand response) as well as advanced system automation are core enabling technologies for Smart Grid. Some important metrological issues for electricity energy have appeared along with rapid development. New important functions have been incorporated in meters for applications in a smart grid system. In the current grid system, a real-time and two-way or multi-layer communication to the meters are essential requirements to PLC (power line communication), for aims of metrology as well as control, e.g., to find out the detailed of consumption in real time and to send out the new price. Some guides or standards have been published [1, 2], in which the power line channel specification has been given. Nevertheless, it would still be an important metrological issue to verify meter’s PLC function. Similar situation exists in the dynamic measurement function of the meters. At present, there is not yet a proper method for verifying this function.

Corresponding author: Zuliang Lu, chief researcher, research fields: electromagnetic metrology, power/energy measurement and impedance measurement. E-mail: luzl@nim.ac.cn.

A proposal to verify the dynamic measurement function and PLC functions of smart meters are discussed further on the base of papers [3, 4]. For the PLC function, the proposal will focus on two aspects, which are the impedance variation and the noise disturbance in the distribution power line network.

These two factors conduct new issue in some place, that this communication approach does not have a successful enough rates, or it is not able to implement communication in any time. Some methods have been presented to overcome this issue. However the author regards it as a metrological issue and puts a proposal in the configuration of meters.

The electronic transforms in voltage and current are also used in power line networks as a kind of new technology. But some of them cannot be applied stably for a long time as their quality. It mainly belongs to duty of manufactures, however, the author likes to discuss them from a viewpoint of metrology, and propose a new selection.

2. Dynamic Measurement Function of Meters

Dynamic current exists in power line because of nonlinear loads, e.g., electrical train. Some new situations appear currently due to distributed energy

resources, such as, plug-in hybrid electric vehicles, solar cell application, etc., where the current drawn will not be stable or even continuous in dynamic/transient condition. The response of meter in such case shall be considered. The test methods as described in IEC standards and other guides, standards or recommendations in level of national or international are for performance verification under stable/static condition only. The dynamic test would be added to insert the existed standard files to verify the new function of the meters.

The high frequency standard equipments existed in metrology field can be adopted to check the response characteristic of meters when imported signal changed rapidly, but kept a periodic repetition in the basic frequency of 50/60 Hz. As far as an in-repetition change we regard it no measurable energy produced as they only exist in a short time. Of course it will impact measuring function of meters. It is a kind of influence quantity, and can be checked in experiment of EMC. Thus a leaved part is repetition change in time interval of more than 20 ms (for 50 Hz) shall be considered specially.

A dynamic current waveform with a sine wave envelope current signal is considered in Ref. [3], as shown in Fig. 1.

$$i = 10\sqrt{2}(0.5 + \sin(2\pi ft/10))\sin(2\pi ft) \quad (1)$$

It is basically a modulated sine wave, in which its rms value is changing from 5 A to 15 A within a relative short time interval (range and the time interval can be controlled). Such a current signal with a test voltage of $220\sqrt{2}\sin(2\pi ft)$ can be used to check the dynamic response of the meter. Its advantage is that the

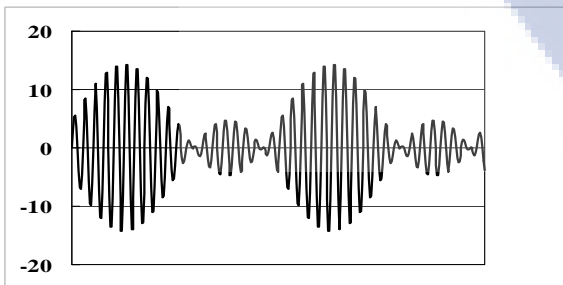


Fig. 1 Dynamic test current waveform.

active power will be $5 \text{ A} \times 220 \text{ V} = 1100 \text{ W}$. The current waveform contains three frequency components: f , $0.9f$, and $1.1f$, in which only the component of f can produce active power. Its disadvantage is that the meter under test may always work only at one range of 20 A. To check and verify possible problems arising from not having a proper response time, or possible errors due to a change in the measurement range, a trapezoidal current waveform envelope can be used with a proper long time interval at a certain level/range and a linear variation between two levels/ranges as the test waveform.

An experiment has been implemented in NIM (National Institute of Metrology), Beijing, China [4]. A measuring system has been developed and evaluated its uncertainty in dynamic condition. Several meters with class 2, 1, 0.5, and 0.2 s in static and inductive principle were selected respectively to test. The results indicated that some meters may not have dynamic measurement performance characteristics, and other meters may only have incorrect but longer measuring time.

As per existing IEC standard, the verification is performed with a stable power source. Some manufacturers take a digital average over a longer time in order to obtain a better accuracy. Under the dynamic testing signals, a negative power will exist in a relative long time. The intrinsic measuring time is in general not to match the testing signals. Therefore the meter will display incorrect positive and negative energy values, even if it can correctly measure the instantaneous power, and correctly display the total energy, i.e., the sum of positive and negative energy. In some places where the positive and the negative energy need to display respectively, e.g., house solar cell system, this kind of meter will not be able to be applied, or we could say, these meters have no dynamic characteristics.

A correct measuring time for energy measurement shall be one period of the industrial frequency. It may be a challenge for the manufacturer to balance the accuracy and dynamic function.

3. PLC Function of Meter

Some test approaches and relative set-ups are introduced in the standard files [1, 2]. They are necessary and reasonable for quality of meter. But they are drafted mainly in communication viewpoint, where the practical application cases are not reflected. The author puts forward two proposals as follows, linked the practical applied condition of meter.

3.1 Impedance Variation Test

To address the PLC function that minimizes the effect for the carried signal arising from the load impedance variations/changes in the distribution power line network, an impedance variation test can be designed to verify the function. In Refs. [1, 2] the equivalent load is simulated simply as a capacitor of 1 μF in series with a resistor of 1 Ω . At power frequencies, it has a relatively high equivalent impedance to allow this test to be done with the distribution power line network voltage directly applied to the meter. It is reasonable because we do not expect a bigger current of power frequency. However it is not a real condition. To achieve the same objective in the real condition, it has been proposed to use a standard power source with a test circuit [3] as shown in Fig. 2. The source output signals, normal voltage and basic current, are connected to the meter under test. The equivalent impedance of the load is connected in series to the current loop. Thus, at power frequencies, the loading effect to the source is practically negligible. The tuned receiver can receive the communication signal produced by the meter under test and measure the sensitivity for the designed load cases. The same type of meter under test can be applied as the receiver. The Isolation Networks minimize the impact of the communication signal frequency to the source.

3.2 Noise Disturbance Test

The meter should also be subjected to a noise disturbance test [3], as shown in Fig. 3. However, the type of the noise according to the Refs. [1, 2] is basically the white noise. The author thinks other noise

disturbance forms would also need to be considered, such as non-uniform and unstable forms. A proposal to include some tests of EMC (applied in voltage of 220 V) will be further investigated. The meters are also subjected to the EMC disturbances in the distribution power line networks. The EMC frequency spectrum shall be wide and will cover the frequency range of the communication signals. The equivalent impedance of the power line networks should include consideration that it would also be subjected to an EMC disturbance test, as shown in Fig. 3. The equivalence impedance connected in parallel to the voltage loop and the signal-to-noise ratio is measured by the receiver. The noise can be conducted or inducted into the pane formed by the dashed. The wide application of new electronic facilities could introduce higher levels of disturbances in the distribution power line networks than as Refs. [1, 2] a new survey/study would be recommended.

The aforementioned two equivalent impedances, either for the load or the power line, need to be further investigated to better reflect the actual practical situation. It should provide the proper relationship between the equivalent impedance and the length of the corresponding transmission network. This experimental data for the meter under test would allow determination of the corresponding transmission distance, through the proposed test using either a toy brick structure or a resistor box structure simulating the equivalent impedance.

For PLC purposes, a standard text message should be incorporated as part of the PLC function which would reflect considerations of all possible cases. This standard text message could also be used to verify the proper function of the communication channel at any time.

4. Out Door Communication of PLC

At some times, PLC is a difficult approach in some place as complexity of the network. The communication signals contained information will be

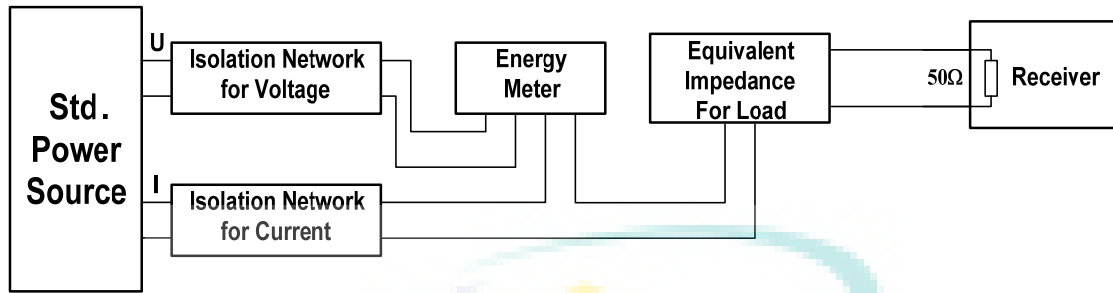


Fig. 2 Impedance variation test.

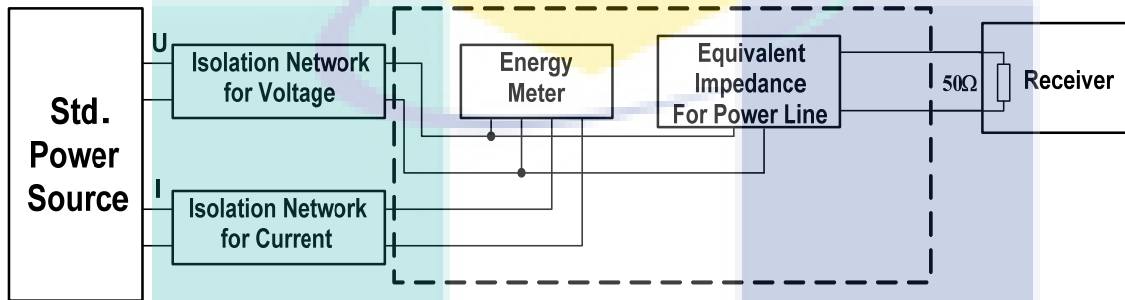


Fig. 3 Noise disturbance test.

attenuated by increased loads, and be disturbed by stronger noises, so that the receiver cannot obtain the effective information.

If we consider the installed point of the meter of every house as “door”, all loads locate the inner of door, and main noises exist inner of door too. But the communication must be implemented out door, and its signal does not be required to go into inner of door. Considering structure of networks of distribution power line, the communication could be apart from the loads and noise sources to avoid their influences. That is the base of an idea “Out Door Communication”.

The key issue is that an Isolation Network must locate at the door, i.e., meter. It has high impedance for high frequency (communication signal), and low impedance for power frequency. Its impedance at 50 Hz shall be so low that the produced consumption can be balance to benefit of communication. Obviously, it shall belong to a kind of inductive element.

For all meters of the distribution power line, we consider that the inductive element shall be installed inside, or aside of meters. Thus the communication signal only can go through “Out Door” for the whole networks. For practical application of all meters, this

element must be different from that is used in laboratory as shown in Figs. 2 and 3, it shall have small dimension (depend on working current) and low price. Of course as material, its permeability must greatly heighten as frequency increases. Currently there is no such element. We wish that a new material with these characteristics will appear in the coming future.

5. Electronic Transformer Quality

Electronic voltage/current transformers improve electricity energy metrology with a series of advantages [5]. But a notable disadvantage is that, they cannot be applied stable for a long time interval, compared with the traditional transformers.

From metrological viewpoint, measuring instruments shall be type evaluation before application for their quality. For example all instruments intended to connect to power line shall through “EMC” experiments, in which some practical disturbances are designed and produced to check the instruments under test, however these disturbances are linked to voltage 220 V only. It can be presumed if no check of these EMC experiments, the instruments under test would not be able to apply stable for a long time interval, as

the present performance of the electronic transformers.

A reasonable consideration is that the existed EMC experiments for the electronic transformers shall be improved. The disturbances in high voltage condition (where the electronic transformers work) shall be further investigated, including their type and strength. The two points shall be paid attention: (1) the distinction between high voltage and low voltage; (2) the difference between electronic (optical) material and ferri-core with copper-winding. A high voltage EMC shall be expected.

6. Conclusions

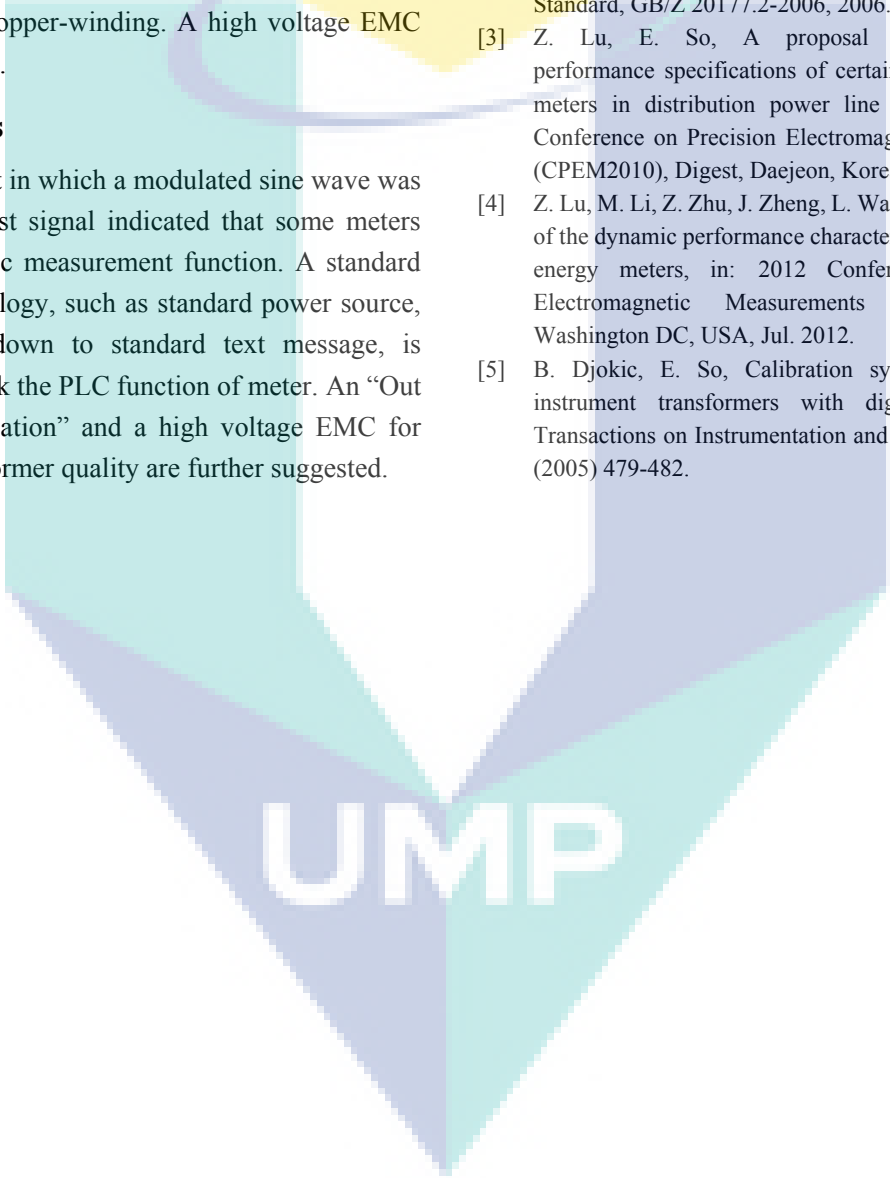
An experiment in which a modulated sine wave was undertaken as test signal indicated that some meters have not dynamic measurement function. A standard concept in metrology, such as standard power source, standard load, down to standard text message, is proposed to check the PLC function of meter. An “Out Door Communication” and a high voltage EMC for electronic transformer quality are further suggested.

Acknowledgments

The author would like to thank Dr. Eddy So of the NRC in Canada for the valuable discussions.

References

- [1] Control Network Power Line (PL) Channel Specification EIA Standard, EIA-709.2-A, Dec. 1999.
- [2] Control Network LONWORKS Technology Specification, Part 2: Power Line Channel Specification, National Standard, GB/Z 20177.2-2006, 2006.
- [3] Z. Lu, E. So, A proposal for verifying the performance specifications of certain functions of smart meters in distribution power line networks, in: 2012 Conference on Precision Electromagnetic Measurements (CPEM2010), Digest, Daejeon, Korea, Jun. 2010.
- [4] Z. Lu, M. Li, Z. Zhu, J. Zheng, L. Wang, E. So, Evaluation of the dynamic performance characteristic of the electrical energy meters, in: 2012 Conference on Precision Electromagnetic Measurements (CPEM), Digest, Washington DC, USA, Jul. 2012.
- [5] B. Djokic, E. So, Calibration system for electronic instrument transformers with digital output, IEEE Transactions on Instrumentation and Measurement 54 (2) (2005) 479-482.

The logo for UMPA (Universiti Malaysia Perlis) is a large, stylized letter 'U' composed of four overlapping triangles in shades of teal and light blue. The letters 'U', 'M', 'P', and 'A' are written in a bold, white, sans-serif font across the bottom of the 'U' shape.

Development of Low Power LED Driver Using LTSpice Software

Muhammad Ikram Mohd Rashid, Aim Izzuddin Hakimi Mohamad Bekri, Suliana Ab Ghani, Mudathir Funsho Akorede and Mohd Herwan Sulaiman

SuPER (Sustainable Energy & Power Electronics Research Group), Faculty of Electrical and Electronics Engineering, University Malaysia Pahang, Pekan 26600, Pahang, Malaysia

Received: August 2, 2013 / Accepted: October 8, 2013 / Published: December 25, 2013.

Abstract: LED driver is regulated power supply designed to match the characteristics of an LED or array of LEDs in our application. The LED current can vary substantially over the battery voltage range even in normal operation device, thus affect the brightness and reduce the life of the lighting device. This project presents a method for the system that provides more efficient solution for driving a low power LED driver by control the LED current and to improve the usage of LEDs in good luminosity, efficiency and long life service. The current mode PWM (pulse width modulation) controlled boost converter for power LEDs application is introduced. According to the characteristic of the power LEDs, they are current controlled devices. Typically, the switching converters are used as the driver for power LED. For this project, the boost topology is selected as the power LEDs driver. Besides, the current mode PWM controller is used to ensure the system is stable. The project used LTC 3783 as PWM control IC and connected to driver circuit to drive low power LED. The calculations are based on design specifications. PSpice software is used for the simulation before the built hardware implementation. The built hardware is tested and finally the waveform and result are recorded.

Key words: Low power LED, PSpice, LTSpice.

1. Introduction

Currently, the advancements in the high-power LED are increasingly finding new application in emergency lights, street lights, traffic lights, automobiles, cars, flashlights and general purpose lighting. Because of their superior longevity, low maintenance requirement, improved luminance, there is no mercury inside the devices. Therefore, they perform an extremely long operating life. LEDs come in two basic categories which are low power LED and high power LED. Low power LEDs commonly come in 3, 5 and 8 mm sizes. These are fractional wattage devices, typically 0.1 W, operate at low current (~ 20 mA) and low voltage (3.2 V DC), and produce a small amount of light, perhaps two to four lumens. For high power LEDs, they commonly

come in 1-3 W packages. They are driven at much higher current, typically 350, 700 or 1000 MA, and with technology can produce 40-80 lumens per 1-W package. High power LEDs come in many different shapes and sizes [1].

LEDs offer many advantages over traditional lighting sources. Exactly which ones are important will depend on the specific application, they include but not limited to: very long life times (50,000 h), lower maintenance cost, more efficient than incandescent and halogen lamps, light up instantly, fully dimmable without filters, directly emit colored light without filters, complete spectrum of colors, dynamic color control tune able white point, total design freedom with hidden light, directed light for more efficient systems, vibration-proof lighting, no mercury, no IR or UV radiation in visible light [2]. LEDs have many advantages such as low power consumption, high efficiency, and long life. They are not only energy

Corresponding author: Muhammad Ikram Mohd Rashid, lecturer, research fields: power electronics, energy conversions, semiconductor devices and renewable energy. E-mail: mikramump@gmail.com.

efficient, but also environmentally friendly [3].

Directional light emission: LEDs are mounted on a flat surface, they emit light hemispherical, rather than spherically. For task lighting and other directional applications, this reduces wasted light.

Low compact size: the small size and directional light emission of LEDs offer the potential for innovative, low-profile, compact lighting design. To produce luminance levels equivalent to high output traditional luminaries requires grouping multiple LEDs, each of which increases the heat sinking needed to maintain light output and useful life.

Breakage resistance: LEDs are largely impervious to vibration because they do not have filaments or glass enclosures. LED's inherent vibration resistance may be beneficial in applications such as transportation (planes, trains, and automobiles), lighting on and near industrial equipment, elevators and escalators, and ceiling fan light kits.

Instant on: LEDs come on at full brightness almost instantly, with no re-strike delay. This characteristic of LEDs is notable in vehicle brake lights, where they come on 170-200 milliseconds faster than standard incandescent lamps, providing an estimated 19 feet of additional stopping distance at highway speeds (65 mph). In general illumination applications, instant on can be desirable for safety and convenience.

Rapid cycling: LED life and lumen maintenance is unaffected by rapid cycling. In addition to flashing light displays, this rapid cycling capability makes LEDs well-suited to use with occupancy sensors or daylight sensors.

No IR or UV emissions: HID lamps can emit significant ultraviolet radiation (UV), requiring special shielding and diffusing to avoid occupant exposure. LEDs emit virtually no IR or UV. Excessive heat (IR) from lighting presents a burn hazard to people and materials. UV is extremely damaging to artwork, artifacts, and fabrics and can cause skin and eye burns in people exposed to unshielded sources [4].

Power LEDs are current controlled devices rather

than voltage. The luminous flux is determined by the forward current. As a result, the power LEDs require a controlled output current. The conventional current control in the LED driver is using the linear regulator. In the linear regulator, BJT (bipolar junction transistor) will be used with the operation in active region. The load current (collector current) is controlled by the value of the base current. In order to produce a large load current, a Darlington pair BJT is used. However, the power dissipation of the BJT is very big due to high current flow. The BJT may be burnt [5].

Due to the high power loss in the BJT, it is replaced by an alternative current controller, called PWM controller. The main advantage of the PWM controller is that it has better efficiency and can be widely applied to LED driver circuit. PWM controller is a control device which can be used as VMC (voltage mode control) and CMC (current mode control). In VMC, the control loop is set up so that the output voltage is compared to a reference voltage by an error amplifier. The output of the error amplifier equals the error. In other words, the amount of feedback voltage is away from the reference voltage. This error voltage is then compared to a wheeling saw-tooth voltage, and a PWM comparator sets the duty cycle for the power switch. The advantages of this topology are that the control loop can be made relatively fast and there is no minimum on time required. However, the disadvantage of this mode is any change in line or load must be first sensed as an output change and then corrected by the feedback loop. Normally it will take a period of time for doing the correction and hence this means slow response. Fig. 1 shows the graphical presentation of the voltage mode control.

In CMC, it is implemented through two control loops, named inner and outer loop, are implemented in CMC. Outer loop monitors the converter's output voltage. It measures the output voltage and provides an error signal to the inner loop. The inner loop monitors the inductor current information and creates the voltage-controlled current source. Inner loop compares

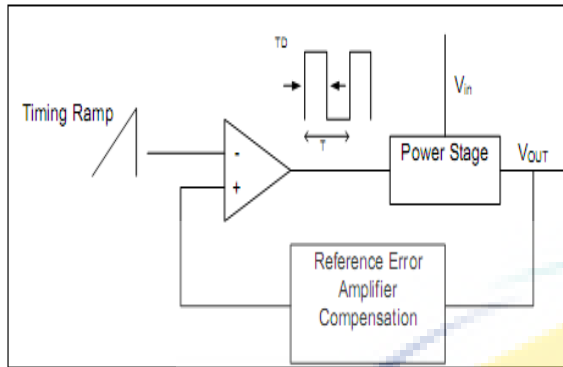


Fig. 1 Voltage mode control [6].

the error signal and an analog of the inductor current to decide when to turn off the switch. The effect is to change the pulse width. The pulse width is a function of the inductor current rather than a function of the error signal. Fig. 2 shows the graphical presentation of the current mode control.

The operation of the current mode controller has advantages over a voltage mode controller. The first is that the inductor current is a direct function of the error voltage, so for small signal analysis the inductor can be replaced by a voltage controlled current source. This removes one order from the transfer function. The control loop is easier to compensate than a voltage mode circuit. Another advantage is that input line voltage changes are removed from the compensation problem. The peak current through the inductor is a function of the voltage across current to rise to the required value and for the comparator to shut off the switch [8].

In this project, boost converter is focused. PWM technique is used to control the density of the LED light in the switching converters. There is one problem faced by the current mode PWM controller. The inner current loop is unconditionally stable as long as the duty cycle is below 50%. However, the output will diverge from stable control when the inner loop is perturbed by noise or transient as the duty cycle is larger than 50%. A current mode controller can be stabilized to maintain control by adding slope compensation. The slope compensation is usually accomplished by feeding some of the voltage from the

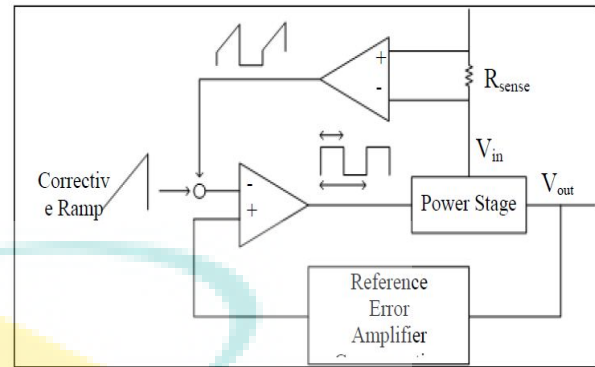


Fig. 2 Current mode controls [7].

oscillator capacitor into either current sense amplifier is the error amplifier. It changes the current trip from a constant voltage to a saw-tooth waveform at the switch frequency.

2. Design Methodology

In this section, the steps to make sure this project was done successfully will be discussed from the beginning until the project was implemented successfully. Firstly, the simulation of LED driver was done by using PSpice software. The main purpose of this result is to determine all the power components values in the boost converter power stage design. This project methodology is to increase the probability of success in hardware development and to avoid any problem from occurring on hardware development. Secondly, the schematics design by refer some information from books, internet, and paper to represent the circuit of boost converter into graphic symbols. After designing the schematic circuit, the components that have been selected in the circuit need to find the value by using specific equation from the previous section to obtain the suitable component value to be used in the analysis. Finally the circuit on proto-board is tested by using several instrument and device at laboratory. Fig. 3 below shows the flow of this project. Basically the steps that have been taken were divided into several parts.

2.1 Software

Before doing the hardware, the simulation part

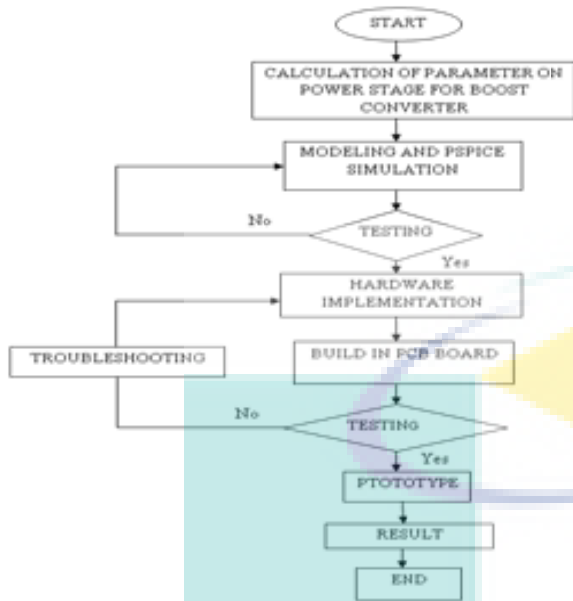


Fig. 3 Flowchart diagram.

should be running in order to make sure that the circuit can operate correctly and achieve the purpose of the project. This part is important because by doing simulation, the fault on the circuit can be safely determined without using the real components. If any failure of the circuit operation occurs, the cause of the failure can be traced by this simulation. If the prototype

is developed without doing the simulation, any failure of the circuit will cause the damage on the components. By doing this simulation, the budget of the project can be minimized and components damage can be avoided.

For this project, the software that has been used:

- (1) PSpice-for simulation;
- (2) LTSpice-for simulation;
- (3) EAGLE (easily applicable graphical layout editor software) for design PCB (printed circuit board).

After performing the PSpice simulation in Fig. 4, this project continues with the LTSpice simulation in Fig. 5 to make sure that the circuit will operate well. For this project, it used LTC 3783 current mode PWM controller as a main controller. The result of the LTSpice simulation will almost be same with the PSpice simulation which by regulating the input of supply in voltage and will get the fixed of output voltage. Before plotting the board, the EAGLE software in Fig. 6 used and convert to Gerber file before import the file to circuit cam to design a PCB layout by using FR4 board. This board plotted by LPKF machine in version S103. The board is plotted in single layer.

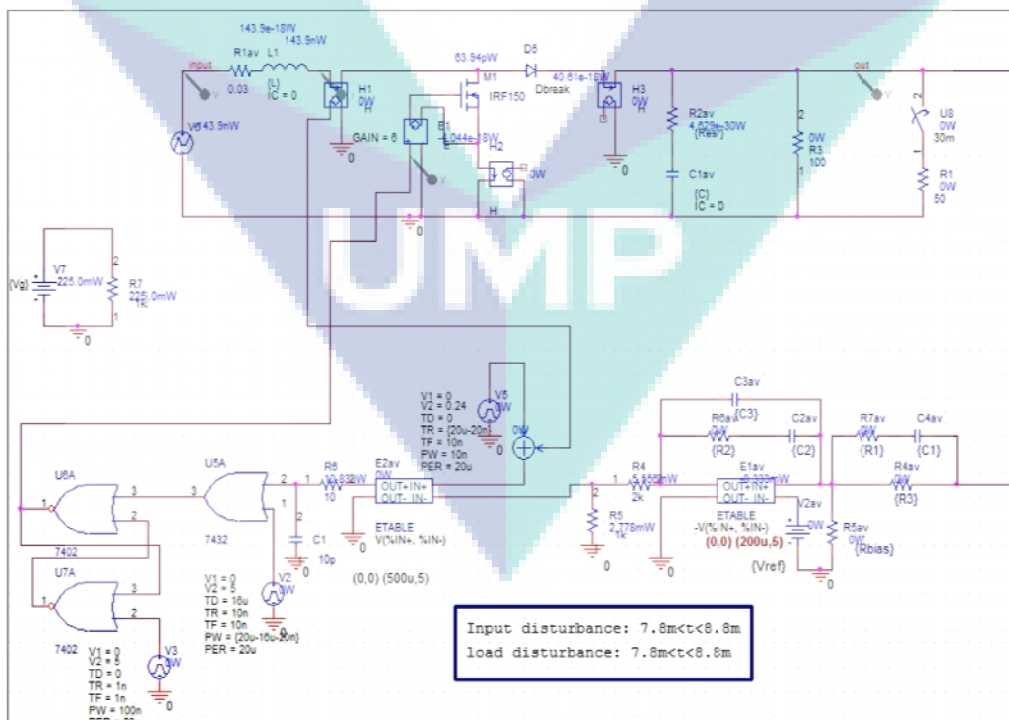


Fig. 4 PSpice simulation circuit.

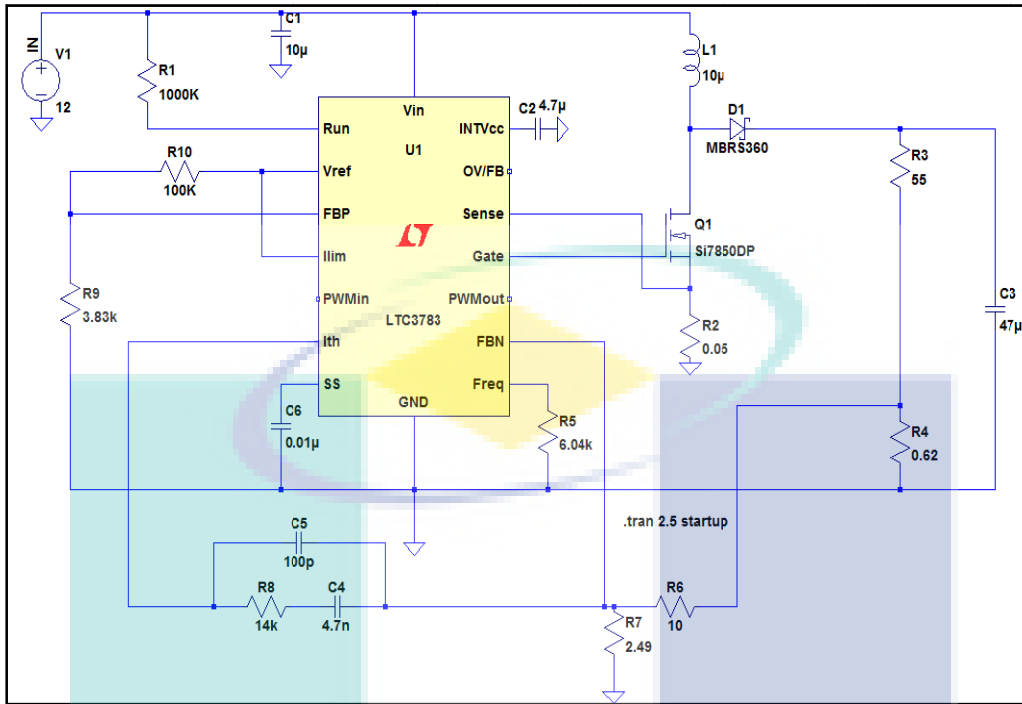


Fig. 5 LTSpice simulation circuit.

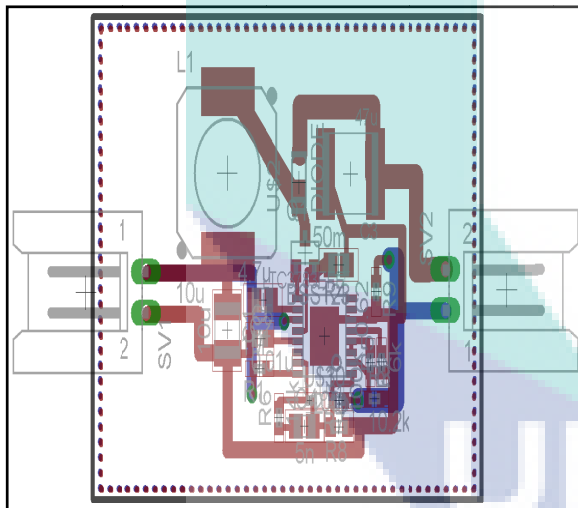


Fig. 6 Circuit design by EAGLE.

2.2 Hardware Implementation

In the hardware implementation, the value of all components that are used for this project must be calculated using the formulas that already derive from basic theory of boost converter as are discussed in introduction. This LED driver circuit consists of various types of electronic components such as inductor, resistor, capacitor, and diode, MOSFET, LED and PWM as a main controller. Basic information about the

component used in this circuit will be described. The component that is an electronic device so made is called a SMD (surface-mount device). Surface mount devices are used in a growing number of commercial and industrial products.

Due to their small size, prototype manufacturing, rework, and repair can be difficult and are best performed by using specialized techniques specific to this technology. Learning these techniques will help you succeed when working with these small components. SMDs have improved performance over through-hole components due to their smaller size, shorter internal leads, and smaller board layouts. These factors reduce the circuit's parasitic inductance and capacitance. SMDs can also be more cost effective than traditional through-hole components due to the smaller board size, fewer board layers, and fewer holes. SMDs can also be easier to replace than through-hole components on multilayer boards. This is because it is very difficult to heat the long hole on a multilayer board, but much easier to heat just the pad and component terminal of an SMD on the surface of a board.

PCB is constructing for this project. Fig. 7 shows the complete PCB layout circuit by using EAGLE software. Then the complete PCB board is shown in Fig. 7 after all processes are done. There are several procedures to produce the PCB which is listed below:

- (1) Construct and design PCB layout using Easily Applicable Graphical Layout Editor Software;
- (2) The arrangement and pad size have to be made carefully in order to prevent the short circuit at the board;
- (3) The complete design for circuit is converting to Gerber file;
- (4) LPKF machine plotter is used to make the complete circuit board.

3. Results and Discussion

Firstly, the input voltage is varying from 12 V to 15 V while switching frequency and duty cycle are set to 1 MHz and 0.5 MHz. Besides that, from the calculation using the equation (2.8), the output voltage is 24 V. Table 1 shows the specification of boost converter.

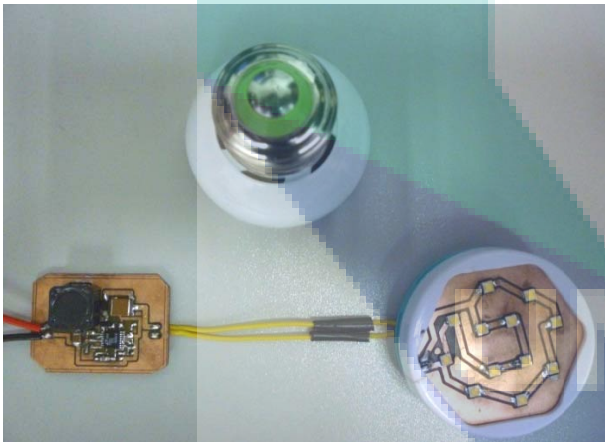


Fig. 7 Complete circuit.

Table 1 Boost converter specification.

Specification	Value
Input voltage	12 V
Output voltage	24 V
Switching frequency	1 MHz
Duty cycle	0.5
Maximum load	400 Ω
Inductor	10 μ H

3.1 PSpice Simulation Results

At the end of this project, the PSpice simulation will be completed and the current mode control for boost converter will be designed into hardware to ensure the stability where the power converter will return to the desired operating point after some disturbances are applied. Table 2 shows the expected result when the input voltage is varying.

The simulation must be done before starting the hardware implementation since this simulation result determines input and output voltage. Duty cycle and switching frequency must be changed to 0.5 kHz and 500 kHz. Fig. 8 shows results for PSpice simulation which the input voltage is varying from 12 V to 15 V and output voltage is 24 V and there is some ripple voltage at the output voltage. Fig. 9 shows the parameter values that obtain from the simulation.

The simulation part should be running in order to make sure that the circuit can operate correctly and achieve the purpose of the project. This part is important because by doing simulation, the fault on the circuit can be safely determined without use the real components. If any failure of the circuit operation occurs, the cause of the failure can be traced by this simulation.

Table 2 Desired output voltage.

Input voltage	Desired output voltage
12 V	24 V
15 V	24 V

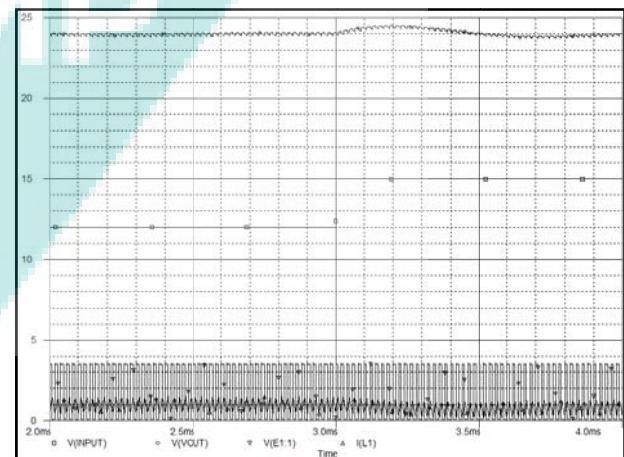


Fig. 8 PSpice simulation results.

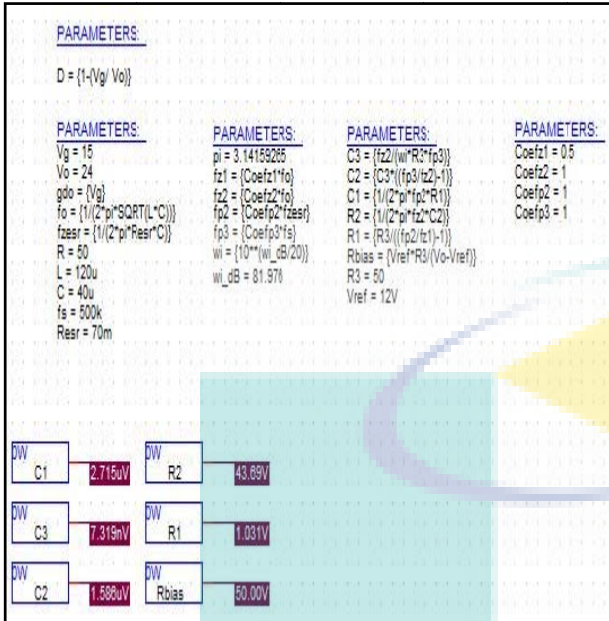


Fig. 9 Parameter obtain from simulation results.

If the prototype is developed without doing the simulation, any failure of the circuit will cause the damage on the components. So more budgets needed to buy the new components. By doing this simulation, the budget of the project can be minimized and components damage can be avoided. For a power LEDs driver, it consists of two main circuits of power stage and PWM controller. In the current mode PWM controller, the loop compensator is the important path in the PWM controller design and overall boost converter design. The loop compensator will stabilize the system when some of the parameters in the design circuit are changed. The list of parameter during PSpice simulation is shown in Table 3. The parameter determined by using calculation and some related formula are used.

3.2 LTspice Simulation Results

The simulation result by LTspice is determined. The parameter that has used in this simulation is used to implement into hardware. From the results that show in Fig. 10, the output current is 0.4 A and the output voltage is 19.5 V. LTspice simulation done and the real parameter implemented into hardware. All the parameter is shown in Table 4.

Table 3 List of parameters in PSpice simulation.

Component	Value
Inductor, L	30 μH
Resistor, R1	0.1 Ω
Resistor, R2	100 Ω
Resistor, R3	50 Ω
Resistor, R4	50 Ω
Resistor, R5	39.2 Ω
Resistor, R6	2 kΩ
Resistor, R7	1 kΩ
Capacitor, C1	33 μF
Capacitor, C2	8.2 nF
Capacitor, C3	1.5 μF

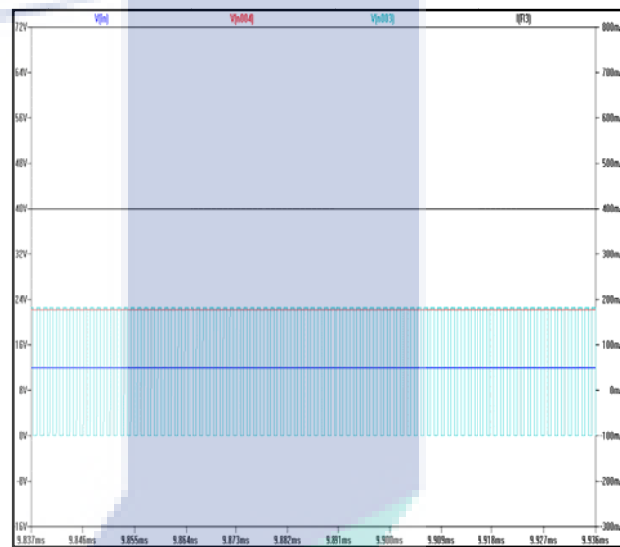


Fig. 10 LTspice simulation.

Table 4 List of parameters in hardware design.

Component	Value
Inductor, L1	10 μH
Resistor, R1	1 MΩ
Resistor, R2	0.05 Ω
Resistor, R3	0.62 Ω
Resistor, R4	6.04 kΩ
Resistor, R5	10 Ω
Resistor, R6	2.49 Ω
Resistor, R7	14 kΩ
Resistor, R8	3.83 kΩ
Resistor, R9	100 kΩ
Capacitor, C1	10 μF
Capacitor, C2	4.7 μF
Capacitor, C3	47 μF
Capacitor, C4	4.7 nF
Capacitor, C5	100 pF
Capacitor, C6	0.01 μF

3.3 Hardware Results

3.3.1 By Using Oscilloscope

The hardware circuit is used to measure the efficiency and power loss on the circuit. The value of frequency in the PWM circuit is 965.3 kHz and the duty cycle is 0.5 as the value in calculation to obtain the equal output voltage which is 24 V. Fig. 11 shows that input voltage is equal to 8 V and Fig. 12 shows that the output voltage is equal to 19.5 V and output current is equal to 0.4 A.

By using oscilloscope, Fig. 13 shows duty cycle waveform, frequency is remain constant between 965 kHz to 966 kHz. Fig. 13 shows the output of PWM with duty cycle is equal to 0.5, input voltage is 8 V, the output voltage is 19.5 V and the frequency is 965.3 kHz.

3.3.2 By Using Multimeter

The output voltage is 19.5 V from the 8 V input voltage and the output current that has measured by multimeter is 0.4 A. There are some losses occur during troubleshooting. The required current that should drive a power LED is about 0.4 A which is 0.2 A for each series. The typical current is selected to make sure that the temperature is suitable for making a long life service. The output current and hardware design is shown in Fig. 14.

4. Conclusions

PSpice and LTspice software are used widely in investigating and design project for boost converter in order to determine if the circuit meets the design criteria. In the current mode PWM controller, the loop compensator is the important path in the PWM controller design and overall boost converter design. The loop compensator will stabilize the system when some of the parameters in the design circuit are changed since the simulation of current mode control for boost converter well done by using PSpice and LTspice during this project. In this project, a current mode PWM controlled boost converter is made for the power LEDs application. The design example can be

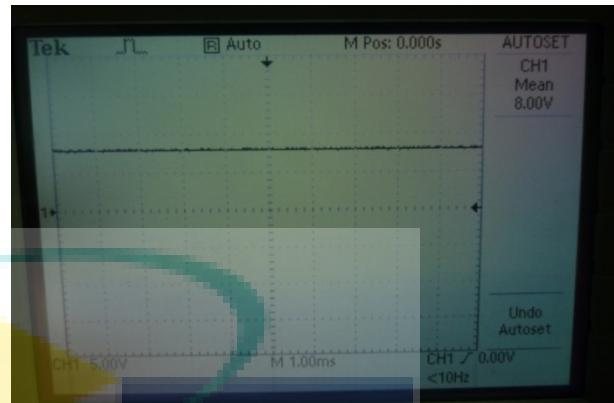


Fig. 11 Input voltage.

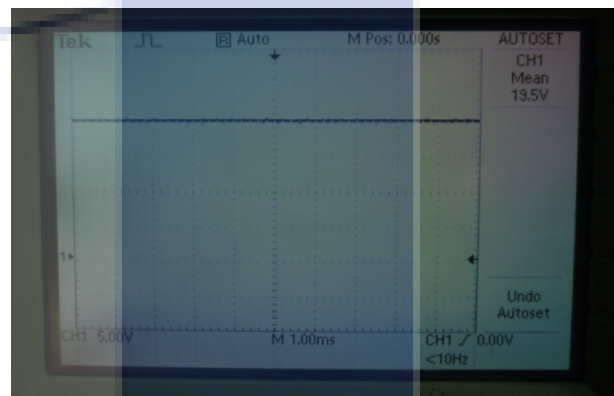


Fig. 12 Output voltage.



Fig. 13 Output of PWM with duty cycle.

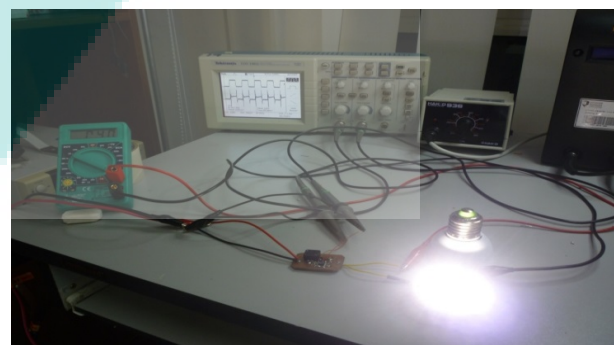
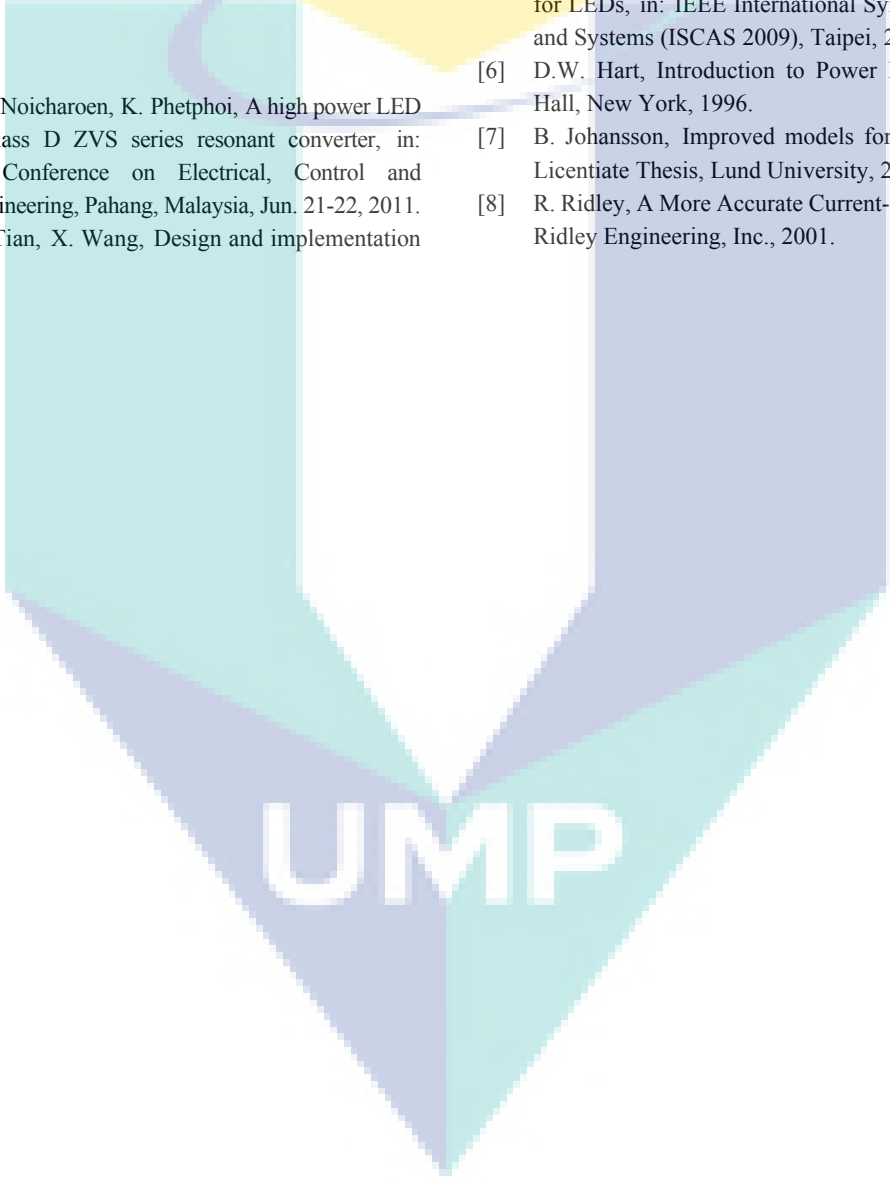


Fig. 14 Hardware testing.

used as a guide in order to build a real hardware design. For a power LEDs driver, it consists of two main circuits which are power stage and PWM controller. For the low voltage application, the boost topology is selected as the driver. There are two modes of control in the PWM controller. They are voltage mode control and current mode control. Due to the more advantages of the current mode control, a current mode PWM controller is designed by using LTSpice software.

References

- [1] P. Chansri, N. Noicharoen, K. Phetphoi, A high power LED driver with class D ZVS series resonant converter, in: International Conference on Electrical, Control and Computer Engineering, Pahang, Malaysia, Jun. 21-22, 2011.
- [2] R. Guen, D. Tian, X. Wang, Design and implementation of LED daylight lamp lighting system, in: International Conference on Electronic Packaging Technology & High Density Packaging, Shanghai, 2008.
- [3] S.W. Lee, R. Zhang, W.L. Leung, Solid state light tube with Periodic Units of Lateral-Emitting LEDs, in: Electronic Components and Technology Conference, USA, 2010.
- [4] L. Dixon, Average Current-Mode Control of Switching Power Supplies, Unit rode Power Supply Design Seminar Handbook, 1990.
- [5] J. Lu, X. Wu, A Novel Multiple Modes PWM Controller for LEDs, in: IEEE International Symposium on Circuits and Systems (ISCAS 2009), Taipei, 2009.
- [6] D.W. Hart, Introduction to Power Electronics, Prentice Hall, New York, 1996.
- [7] B. Johansson, Improved models for DC-DC converters, Licentiate Thesis, Lund University, 2003
- [8] R. Ridley, A More Accurate Current-Mode Control Mode, Ridley Engineering, Inc., 2001.

The logo for UMP (Universiti Malaysia Pahang) is a large, stylized letter 'U' composed of several overlapping geometric shapes in shades of teal, light blue, and purple. The letters 'UMP' are printed in a bold, white, sans-serif font across the bottom center of the 'U' shape.

UMP

Fire Detection in Video Sequences Based on Static and Dynamic Features

Rykhard Bohush¹, Nadeja Brouka¹ and Sergey Ablameyko²

1. Department of Computer Systems and Networks, Faculty of Information Technologies, Polotsk State University, Novopolotsk 211440, Belarus

2. Department of Information Management Systems, Faculty of Applied Mathematics and Computer Science, Belarussian State University, Minsk 220050, Belarus

Received: July 9, 2013 / Accepted: November 28, 2013 / Published: December 25, 2013.

Abstract: In this paper we propose the efficient smoke and flame detection algorithms for intelligent video surveillance systems. Our algorithms consider dynamic and static features of smoke and flame including contrast, color, texture features and motion information. For smoke detection, the approach uses the motion and contrast as the two key features of smoke. Motion is a primary sign and it is used at the beginning for candidate areas extraction from a current frame. Furthermore, the direction of smoke distribution is also considered as an estimated movement based on the optical flow technique. For flame detection, we use the color image segmentation technique. Firstly, the temporal and spatial wavelets are analyzed. Then, color and texture features for candidate flame regions are extracted. Texture features are defined based on the normalized gray level co-occurrence matrix after computation of local binary pattern. Experimental results asserted the advantages of the proposed fire detection in the diversity of test video sequences.

Key words: Flame and smoke detection, background subtraction, contrast analysis, wavelet transform, texture segmentation.

1. Introduction

Early fire detection on open spaces, in buildings, in territories of the industrial enterprises is an important component for making any system of fire safety. Traditional fire detectors which have been widely applied in the buildings are based on infrared sensors, optical sensors, or ion sensors that depend on certain characteristics of fire, such as smoke, heat or radiation. Such detection approaches require a position of sensor in very close proximity to fire or smoke and often give out false alarms. So they may be not reliable and cannot be applied into open spaces and larger areas. Due to the rapid developments in digital camera technology and video processing techniques, intelligent video surveillance systems have been

installed in various public places for monitoring. Therefore, there is a noticeable trend to use such systems for early fire detection with special software applied.

We propose algorithms for smoke and flame detection on color video sequences obtained from a stationary camera. Smoke detection algorithm consists of the following steps: (1) preprocessing; (2) slowly moving areas and pixels segmentation in a current input frame based on adaptive background subtraction; (3) merge slowly moving areas with pixels into blocks; (4) classification of the blobs obtained before. Flame detection algorithm is composed of basic steps: (1) candidate flame regions detection; (2) color and texture features extraction; (3) object classification.

2. Related Work

Generally, the video processing-based fire detection

Corresponding author: Rykhard Bohush, Ph.D., research fields: image processing, intelligent video analysis and pattern recognition. E-mail: rbohush@gmail.com.

algorithms are carried out using two principal characteristics of fire, which are flame and smoke [1]. Video processing based on fire detection still has challenges. This is mainly due to the following reasons: diverse background, lighting and none of the primitive image features such as intensity, motion, edge and texture characterizes smoke and flame.

Motion information provides a key as the pre-condition to locate the possible smoke regions. The algorithm of background subtraction is traditionally applied to movement definition in video sequence [2-5]. Common techniques use the adaptive Gaussian mixture model to approximate the background modeling process such as Refs. [2, 3]. In Ref. [6], optical flow calculation is applied to detection of movement of a smoke. The drawbacks of the given approach are high sensitivity to noise and high computational cost. Algorithms based on color and dynamic characteristics of a smoke are applied for classification of the given moving blocks. In Ref. [7], the algorithm comparative evaluation of the histogram-based pixel level classification is considered. In this algorithm, the training set of video sequences with smoke is applied to the analysis. Methods based on the preliminary training highly depend on the quality of training set classification. It demands much qualitative characteristics of the processed images. The area of decreased high frequency energy component is identified as smoke using wavelet transforms [2, 3]. However, change of scene illumination can be contours degradation reason. Therefore, such approach requires additional estimations. Color information is also used for identifying smoke in video. Smoke color at different stages of ignition and depending on a burning material is distributed in a range from almost transparent white to saturated gray and black. In Ref. [2] decrease in value of chromatic components U and V of color space YUV is estimated.

Phillips et al. [8] use color model based on Gaussian distribution to the color histogram for flame

detection. This algorithm employs information gained through both color and temporal variation to detect fire. In Ref. [9], flame is detected by analyzing the video in the wavelet domain in addition to ordinary motion and color clues. The algorithm checks flicker in flames using 1-D temporal wavelet transform and color variation in fire-colored moving regions using 2-D spatial wavelet transform. Töreyn et al. [10] use the hidden Markov models and the wavelet transform for flickering pixels detection that indicate the presence of flames. The hidden Markov models are used temporally and spatially to determine if flame colored pixels flicker or not. In Ref. [11], video fire detection algorithm based on the covariance texture representation method is considered. The algorithm does not use a background subtraction method and therefore it can be used with moving cameras, but he works well when the fire is clearly visible and in close range so that the flicker and irregular nature of flames are observable. Chenebert et al. [12] use a combined texture and color based feature descriptor as an input to a trained classifier based detection boundary. Feature classification is performed based on isolation of candidate fire pixel regions using a basic color spectroscopy approach and combined color-texture classification of these regions using a trained classification approach.

3. Smoke Detection

The proposed algorithm uses motion and contrast as the two key features for smoke detection. The preprocessing block applies some methods of image processing which increases the performance of the proposed detection algorithm and reduces false alarms. Frame preprocessing block comprises three steps: grayscale transformation, histogram equalization and the discrete wavelet of the current input frame. Cameras and image sensors must usually not only deal with the contrast on a scene but also with the image sensors exposure to the resulting light on that scene. Histogram equalization is a most commonly used

method for improvement of contrast image characteristics. To resize the image and to remove high frequencies on horizontal, vertical and diagonal details, the discrete wavelet transform to Haar basis is applied. Wavelet transform to Haar basis is the simplest and the fastest algorithm that is important for systems of video processing.

In the course of the distribution, a smoke is being gradually blended to the background. Our adaptive algorithm of background subtraction considers this characteristic of a smoke and is based on the ideas stated in works of Refs. [3, 13]. A background image B_t at time instant t is recursively estimated from the image frame I_{t-1} and the background image B_{t-1} of the video as follows [13]:

$$B_t(x, y) = \begin{cases} \alpha B_{t-1}(x, y) + (1-\alpha)I_{t-1}(x, y), \\ \text{if } (x, y) \text{ is moving;} \\ B_{t-1}(x, y), \text{ if } (x, y) \text{ is stationary.} \end{cases} \quad (1)$$

where (x, y) represent a pixel video frame and α is a adaptation parameter between 0 and 1. As the area of a smoke frame by frame grows slowly that the pixels belonging to a smoke, quickly did not fix in a background, value α should be close to 1.

At the initial moment of time $B_0(x, y) = I_0(x, y)$. Pixel (x, y) belongs to moving object if the following condition is satisfied [13]:

$$\begin{aligned} & (|I_t(x, y) - I_{t-1}(x, y)| > T_t(x, y)) \& \\ & (|I_t(x, y) - I_{t-2}(x, y)| > T_t(x, y)) \end{aligned} \quad (2)$$

where $I_{t-2}(x, y), I_{t-1}(x, y), I_t(x, y)$ values of intensity of pixel (x, y) at time instant $t-2, t-1$ and t respectively; $T_t(x, y)$ is adaptive threshold for pixel (x, y) at time instant t calculated as follows:

$$T_t(x, y) = \begin{cases} \alpha T_{t-1}(x, y) + (1-\alpha)(5 \times \\ |I_{t-1}(x, y) - B_{t-1}(x, y)|) - \\ \text{if } (x, y) \text{ is moving;} \\ T_{t-1}(x, y), \text{ if } (x, y) \text{ is stationary.} \end{cases} \quad (3)$$

At the initial moment of time $T_0(x, y) = \text{const} > 0$.

Accurate separating of a foreground object from the background is the main task of digital matting. Porter and Duff [14] introduced the blending parameter (so-called alpha channel) as a solution of this problem

and a mean to control the linear combination of foreground and background components. Mathematically the current frame I_{t+1} is modeled as a combination of foreground F_{t+1} and background B_t components using the blending parameter β :

$$I_{t+1}(x, y) = \beta F_{t+1}(x, y) + (1-\beta)B_t(x, y) \quad (4)$$

For opaque objects value of β is equal to 1, for transparent objects value of β is equal to 0 and for the semitransparent objects, such as smoke, value of β lays in a range from 0 to 1. As it is shown further in this section, we have experimentally established the optimum value for β , to be equal to 0.38.

So, as soon as we have obtained B_t component on background update step, current frame I_{t+1} and set β to 0.38, we can estimate the foreground component F_{t+1} . Then we apply the threshold processing to receive the binary foreground F_{bin} :

$$F_{bin} = \begin{cases} 1, \text{ if } (F_{t+1} > 245) \\ 0, \text{ otherwise} \end{cases} \quad (5)$$

At the current step of algorithm, we have 2 parameters α and β which are necessary to be estimated. Optimum values of α and β can be estimated using ROC (receiver operating characteristic) analysis. For estimation implementation the training set from five video sequences of the 200 frames length which contain and do not contain smoke were used. Using the ground truth regions which have been online marked as a smoke in the training frames, rates of true and false detection were calculated for the whole frame set. We received a background for each value of α within a range of (0, 1). After that we applied a background subtraction and thresholding to each frame from a training set, and then calculated TPR (true positive rate) and FPR (false positive rate). For each value of α , the average TPR and FPR is evaluated on a training frame set and used in the ROC curve. Using the ROC curve, an optimum value for α can be easily selected for the smoke detection algorithm based on a pre-defined correct detection versus false detection rates. It is necessary to choose such value of α that slowly

moving objects will not join a background too quickly, i.e. that a smoke will not fixed in a background too fast. At the given stage of algorithm high TPR is important and high enough FPR is acceptable as it is necessary to receive as much as possible pixels for the analysis and incorrectly classified pixels should be excluded at the following stages. Therefore we have established an α value equals to 0.95. Similarly using the training frame set, receiving a foreground component F_{t+1} and after that the foreground F_{bin} and counting FPR and TPR for all values β from a range (0, 1) with the step 0.001 we build a ROC curve for β . Value of β has been chosen to be equal to 0.38, because at such value of β provides high TPR and low FPR.

On the next step of smoke detection algorithm to clear of noise and to connect of moving blobs the connected components analysis is used. This form of analysis takes in a noisy input foreground. Morphological operations are applied to reduce the noise:

- morphological opening to shrink areas of small noise:

$$S \circ M = (S(-)M) \oplus M \quad (6)$$

where, S is image, M is structuring element 3×3 ;

- morphological closing to rebuild the area of surviving components that was lost in opening:

$$S \bullet M = (S \oplus M)(-M) \quad (7)$$

where, M is structuring element 3×3 .

After that, edge analysis is applied and contours with a small perimeter are removed.

Blocks matching approach for optical flow calculation assumes that the frame is divided into small regions called blocks. It considers a primary direction of smoke propagation. It shows in Ref. [15] that global direction of smoke is $0-45^\circ$. This statement allows to simplify procedure of blocks matching detection and, hence, to considerably reduce number of calculations. Blocks are typically squares and contain some number of pixels. These blocks do not overlap. In our implementation frames in the size 320×240 pixels divided into blocks 2×2 pixels. Block

matching algorithm attempt to divide both the previous and current frames into such blocks and then compute the motion of these blocks. Each block of size 2×2 can move in eight possible directions. Our implementation searches in three directions of the original block $q_{x,y}^{prev}$ (in the previous frame) and compares the candidate new blocks $q_{x-1,y-1}^{curr}$, $q_{x,y-1}^{curr}$ and $q_{x+1,y-1}^{curr}$ (in the current frame) with the original. This comparison is calculated as follows:

$$F(q_{x,y}^{prev}, q_{x+k,y-1}^{curr})_{k \in \{-1,0,1\}} = \left(\frac{\min(I_{i,j}^{prev}, I_{i,j}^{curr})}{\max(I_{i,j}^{prev}, I_{i,j}^{curr})} \right) \quad (8)$$

where, $I_{i,j}^{prev}$ is the intensity value of pixel on the previous frame, belonging to the block $q_{x,y}^{prev}$; $I_{i,j}^{curr}$ is the intensity value of pixel on the current frame, belonging to the block $q_{x,y}^{curr}$; N is count of blocks into which divided the previous and current frame. The block $q_{x,y}^{prev}$ in the previous frame will correspond to the block in the current frame if function F has the maximum value. Optical flow calculation (function F) is done only for the blocks belonging to the foreground (Fig. 1b). The result of this step is the set of vectors c_s having a direction corresponding to primary propagation of smoke (Fig. 1c).

From each blob from the previous steps we calculate percentage ρ of blocks which have moved in primary direction of smoke:

$$\rho = \frac{c_s}{c} \cdot 100 \frac{dy}{dx} \% \quad (9)$$

where c is the total number of blocks on a current frame, and Weber contrast C_w :

$$C_w = \frac{1}{n} \sum_{i=1}^n \frac{F_{t+1}(x,y) - B_t(x,y)}{B_t(x,y)} \quad (10)$$

where, $F_{t+1}(x,y)$ -value of pixel intensity (x,y) at time instant t , belonging to a blob; $B_t(x,y)$ -value of background pixel intensity (x,y) at time instant t under blob; n -number of the pixels belonging to a blob. If the blob has successfully checked out that we classify it as a smoke. Experimentally established values $C_w > 0.5$ and $\rho > 20\%$ allow efficient distinguishing a smoke from objects with similar

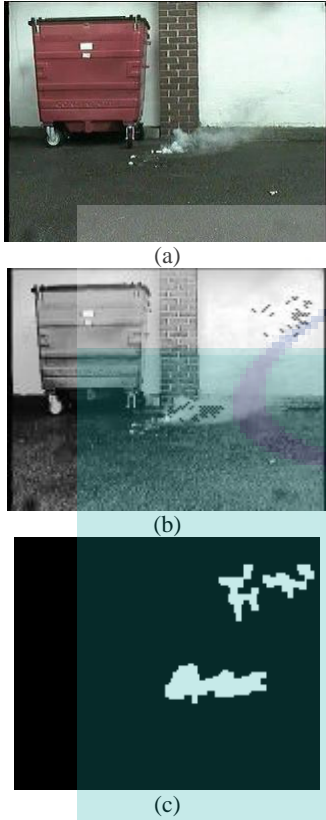


Fig. 1 (a) The current frame, (b) the clean up foreground by the connected components analysis and (c) the results of optical flow calculation.

behavior: a fog, shadows from slowly moving objects and patches of light.

4. Flame Detection

CFR (candidate flame regions) are initially isolated based on color image segmentation, wavelet analysis and post-processing for binary mask of CFR. For image segmentation and flame-colored pixels we use RGB space and rule-set [16]:

$$\begin{cases} R(x, y) > R_{mean} \\ R_{mean} = \frac{1}{K} \sum_{i=1}^K R(x_i, y_i) \\ R(x, y) > G(x, y) > B(x, y) \\ 1.1403g - 0.0759 \leq r \leq -0.9889g + 0.9913 \\ 0.8459b + 0.0482 \leq g \leq -0.4608b + 0.4954 \end{cases} \quad (11)$$

where, $R(x, y)$, $G(x, y)$, $B(x, y)$ are Red, Green and Blue values of pixel respectively; K is the total number of pixels in image; R_{mean} is the mean of Red channel of pixels where a change is not detected and rgb are normalized color space for RGB. The rgb



Fig. 2 (a) The input frame and (b) binary mask after image segmentation.

space can be represented:

$$\begin{cases} r = R / R + G + B \\ g = G / R + G + B \\ b = B / R + G + B \end{cases} \quad (12)$$

We set a binary mask with include fire-colored pixels (Fig. 2).

After that, we use one-dimensional temporal wavelet transform for analysis of checks flicker in flames and two-dimensional spatial wavelet transform for analysis of color variation in flame-colored regions. For temporal wavelet analysis each red component of RGB space fire-colored pixel is fed to a two stage-filter bank. If the pixel is part of a flame boundary at some time, then there will be several spikes in one second due to transitions from background colors to flame colors and vice versa [3]. In contrast to work on fire detection [3], for reducing the time we do not use moving region detection.

Spatial wavelet analysis using low-high (SI_{lh}), high-low (SI_{hl}) and high-high (SI_{hh}) wavelet sub-images are added to obtain these images for parameter calculation of pixel (x, y) [3]:

$$v = \frac{1}{M \times N} \sum_{x,y} \left((SI_{lh})^2 + (SI_{hl})^2 + (SI_{hh})^2 \right) \quad (13)$$

where $M \times N$ is the number of pixels in the fire-colored moving region.

As a result we receive a mask for CFR. On a final steps clearing of noise based on morphological opening and closing, area filtering by size for mask is used. If the area perimeter is equal or more than 1/8 perimeters of a frame, this area is CFR.

After that, texture features for candidate flame regions are extracted. Haralick [17] suggested the use

of GLCM (grey level co-occurrence matrices) to extract second order statistics from an image. This method is based on the joint probability distributions of pairs of pixels. Textural features are calculated with use of co-occurrences matrix:

$$P_d^\theta(i, j) = \{((r, s), (t, v)) : I(r, s) = i, I(t, v) = j\} \quad (14)$$

where, $(r, s), (t, v) \in N_x \times N_y; (t, v) = (r + d, s + d);$ d -distance between two next pixels in a direction θ .

In our work, we will use a set of offsets sweep through 180 degrees ($0^\circ, 45^\circ, 90^\circ$ and 135°) and $d = 1$, obtaining four GLCM matrices. From the co-occurrence matrices, nine Haralick texture descriptors (entropy, energy, contrast, sum average, variance, correlation, maximum probability, inverse difference moment, and cluster tendency) are computed [17]. We use five such summary statistics based on normalized GLCM N_d^θ :

$$\text{Entropy: } E = -\sum_i \sum_j N_d^\theta(i, j) \log_2 N_d^\theta(i, j) \quad (15)$$

$$\text{Energy: } En = \sum_i \sum_j (N_d^\theta(i, j))^2 \quad (16)$$

$$\text{Contrast: } C = \sum_i \sum_j (i - j)^2 N_d^\theta(i, j) \quad (17)$$

Inverse difference moment

$$IDM = \sum_i \sum_j \frac{N_d^\theta(i, j)}{1 + |i - j|} \quad (18)$$

$$\text{Correlation } Cor = \frac{\sum_i \sum_j (i - \mu_i)(j - \mu_j) N_d^\theta(i, j)}{\sigma_i \sigma_j} \quad (19)$$

where $\mu_i = \sum_j i \cdot N_d^\theta(i, j)$, $\mu_j = \sum_i j \cdot N_d^\theta(i, j)$,
 $\sigma_i = \sum_j N_d^\theta(i, j)(i - \mu_i)$, $\sigma_j = \sum_i N_d^\theta(i, j)(j - \mu_j)$.

In contrast to work on fire detection [12], texture features are calculated for a gray-scale CFR after applying a local binary pattern operator. Ojala et al. [18] introduced the LBP (local binary pattern) operator in 1996 as a means of summarizing local gray-level structure. It should be noted that the basic LBP features have performed very well in various applications, including texture classification and segmentation, image retrieval and surface inspection [19]. The operator takes a local neighborhood around each pixel, the pixels of the neighborhood at the value

of the central pixel and uses the resulting binary valued image patch as a local image descriptor. It was originally defined for 3×3 neighborhoods, giving 8 bits codes based on the 8 pixels around the central one. LBP code for center pixel p is defined as equation:

$$LBP_p = \sum_{i=0}^7 2^i S(g_i - g_c) \quad (20)$$

where, g_c is gray value of p , g_i is gray value of i pixels.

$S(x)$ is the threshold function that can be defined as equation:

$$S(x) = \begin{cases} 1, & \text{if } x \geq 0, \\ 0, & \text{otherwise.} \end{cases} \quad (21)$$

For color features CFR, we use HSV space which allows us to isolate the illumination component of the scene. Hue and Saturation channels are quantized as 20 element normalized histograms for input as features for classification [12].

In the first step, the classifier is trained by using 50 positive and 50 negative flame images. Sample images from the training set are shown in Fig. 3. Calculated texture features (entropy, energy, contrast, inverse difference moment and correlation) after applying a LBP operator and color features in HSV space were used for object classification.

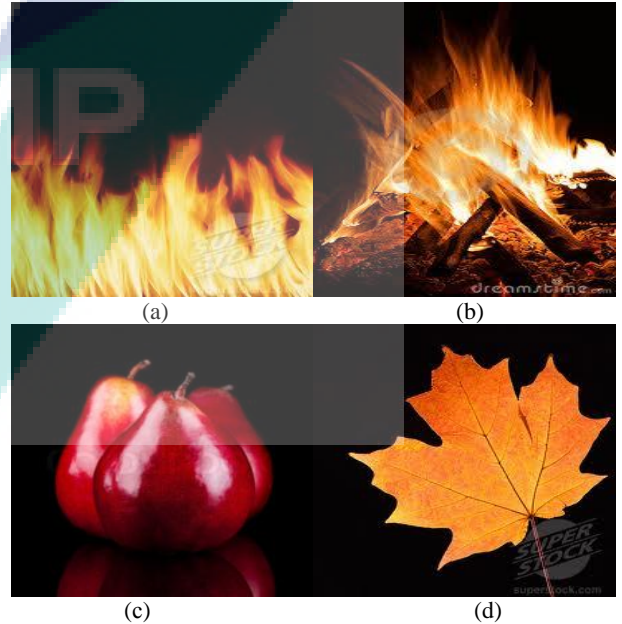


Fig. 3 Examples for (a, b) positive and (c, d) negative flame images.

For objects classification k-nearest neighbor algorithm is used. This algorithm is a method for classifying objects based on closest training examples in the feature space. In the second step, it is performed to assess the quality of training based on test sample images. There are no overlap between training and testing images. Training and testing phases are performed once for classifier configuration.

5. Experimental Results

The developed algorithms were tested on the real cases. Test were run on a PC (AMD Athlon (tm) II X2 245, 2.91 GHz, RAM 2 GB). Our program was implemented using Visual C++ and an open source computer vision library Open CV. The proposed algorithm has been evaluated using data set publicly available at the web address <http://signal.ee.bilkent.edu.tr/VisiFire/Demo/SampleClips.html>, <http://www.openvisor.org> and <http://cvpr.kmu.ac.kr>. Test video sequences contain a smoke, moving people, moving transport, a complex dynamic background, and also a number of video sequences without any smoke/flame. Fig. 4 shows some examples for smoke and flame detection. Detection results for some of the test sequences are presented in Table 1.

For smoke detection processing time of a current frame depends on the block sizes and frequency of changes occurring in a background. If the background is stable and few blocks are detected then processing time decreases. The smoke has been found successfully out on all test video sequences with a smoke.

Therefore in this case, we cannot directly find out a smoke and detection time is increasing. The performed experiments have shown that the algorithm quickly finds out a smoke on a complex dynamic scene. Smoke detection is achieved practically in real time. The processing time per frame is about 15 ms. for frames with sizes of 320 by 240 pixels. The algorithm considers both dynamic and static features of

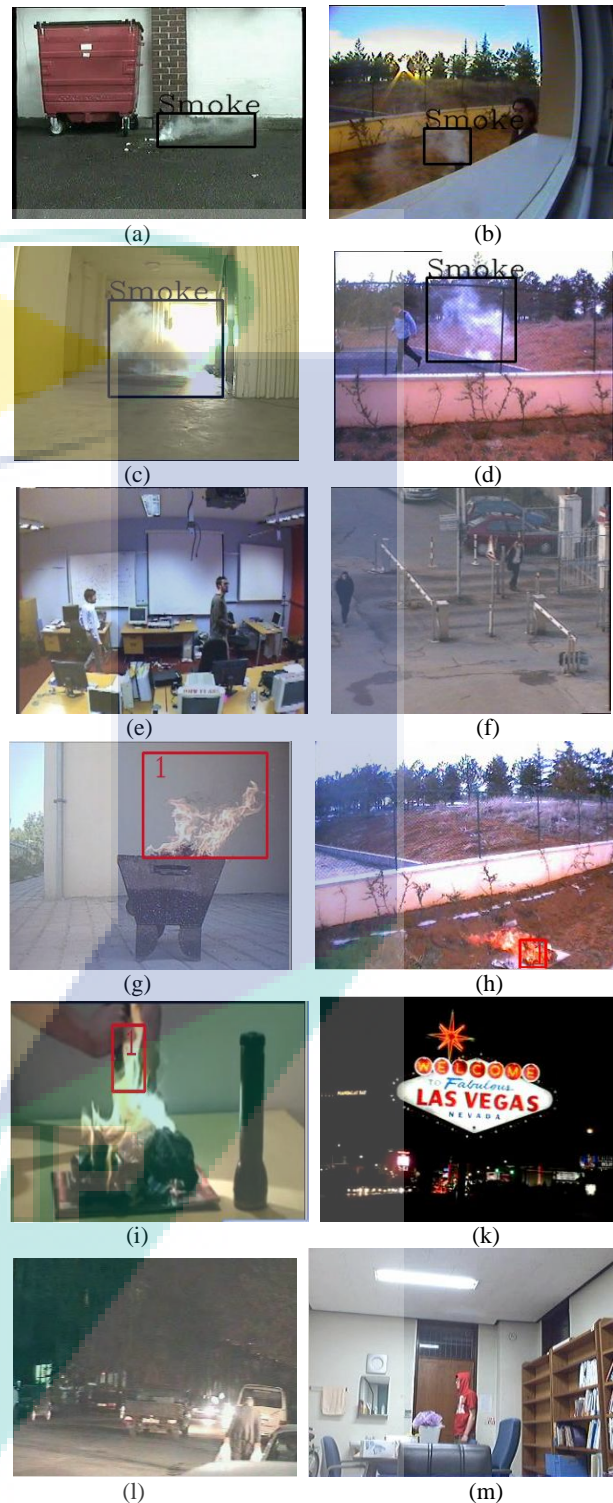


Fig. 4 Smoke and flame detection in video.

a smoke. The algorithm has a low false alarm level. False alarms on objects with properties similar to a smoke are sometimes possible. Tracing of smoky properties during some frames can solve this problem.

Table 1 Detection results for some of the test video sequences.

Video sequences (Fig. 4)	The processing time per frame (ms)	The flame or smoke was present with / is found with (number of frame)	The number of frames on which there was false alarm / Total of frames
(a)	12.67	10 / 12	0 / 900
(b)	14.79	20 / 112	0 / 244
(c)	14.97	80 / 87	0 / 483
(d)	15.00	30 / 117	0 / 630
(e)	16.35	-	0 / 1073
(f)	14.57	-	0 / 1179
(g)	63.00	1 / 125	0 / 439
(h)	56.00	1 / 223	0 / 1201
(i)	45.00	1 / 123	0 / 411
(k)	48.00	-	0 / 530
(l)	42.00	-	0 / 160
(m)	47.00	-	0 / 171

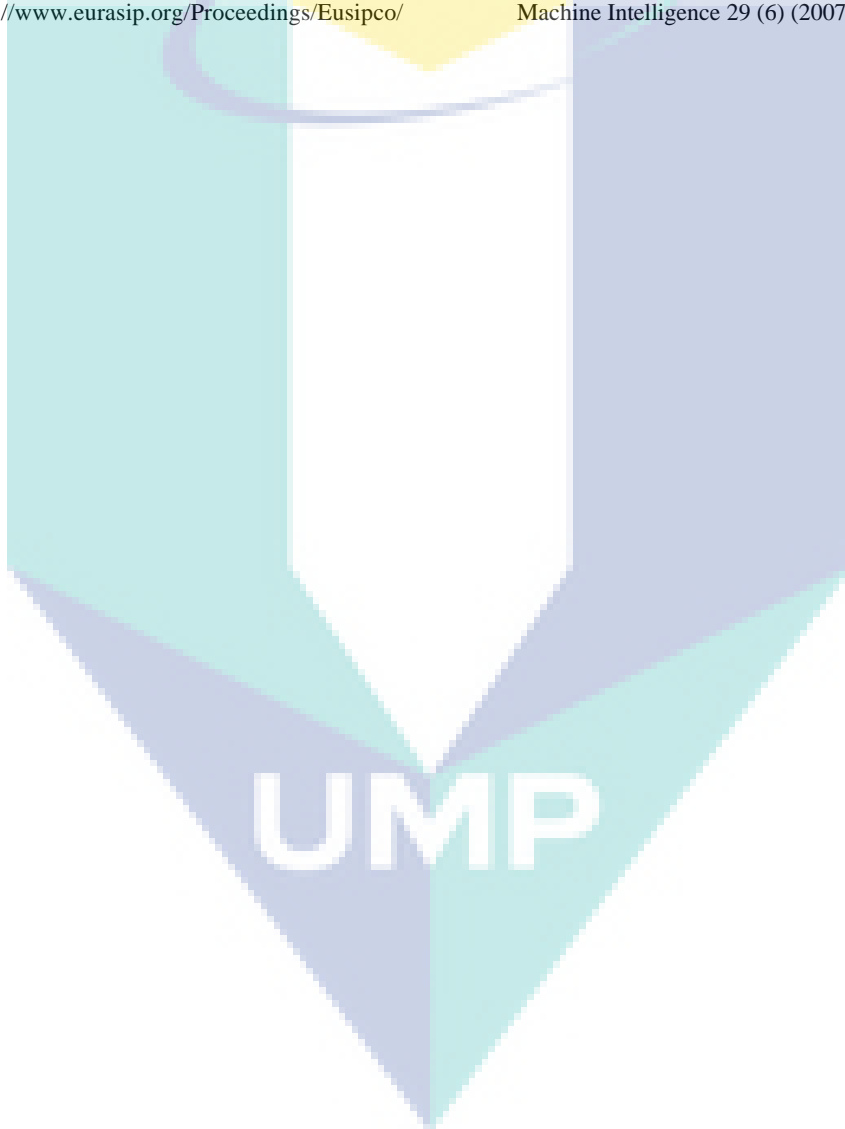
6. Conclusions

We have presented in this paper algorithms for smoke and flame detection in video sequences. Our algorithms consider dynamic and static features of smoke and flame: contrast, color, texture features and motion. For smoke detection the algorithm uses motion and contrast as the two key features of smoke. Motion is a primary sign and is used at the beginning for extraction from a current frame of candidate areas. In addition to consider a direction of smoke distribution the movement estimation based on the optical flow is applied. For flame detection we use color image segmentation, temporal and spatial wavelet analyses on the first step. After that color and texture features for candidate flame regions are extracted. Texture features are defined based on normalized gray level co-occurrence matrix after computation of local binary pattern. We use Hue and Saturation channels HSV space for color features.

References

- [1] M. Garcia Leonardo, G. Sanchez Perez, M. Nakano, K. Toscano Medina, H. Perez Meana, L. Rojas Cardenas, An early fire detection algorithm using IP cameras, *Sensors* 12 (5) (2012) 5670-5686.
- [2] P. Piccinini, S. Calderara, R. Cucchiara, Reliable smoke detection system in the domains of image energy and color, in: *ICIP*, San Diego, CA, 2008.
- [3] B.U. Toreyin, Y. Dedeoglu, A. E. Cetin, Wavelet based real-time smoke detection in video, *Signal Processing: Image Communication* (20) (2005) 255-256.
- [4] D. Kim, Y. Wang, Smoke Detection in Video, in: *WCCSIE*, Los Angeles, CA, 2009.
- [5] B.U. Toreyin, Y. Dedeoglu, A. Cetin, Contour based smoke detection in video using wavelets, in: *14th European Signal Processing Conference (EUSIPCO 2006)*, Florence, Italy, 2006.
- [6] F. Comez Rodriuez, B.C. Arrue, A. Ollero, Smoke monitoring and measurement using image processing, application to forest fires, in: *Proc. of SPIE ATR*, 2003, pp. 404-411.
- [7] D. Kristinić, T. Jakovcevic, D. Stipanicev, Histogram-based smoke segmentation in forest fire detection system, *Information Technology and Control* 38 (3) (2009) 237-244.
- [8] W. Phillips III, M. Shan., V. Lobo, Flame recognition in video, *Pattern Recognition Letters* 23 (1-3) (2002) 319-327.
- [9] B.U. Toreyin, Y. Dedeoglu, U. Gudukbay, A.E. Cetin, Computer vision based method for real-time fire and flame detection, *Pattern Recognition Letters* 27 (1) (2006) 49-58.
- [10] B.U. Toreyin, Y. Dedeoglu, Y. Enis-Çetin, Flame detection in video using hidden markov models, in: *Proceedings of IEEE International Conference on Image Processing*, 2005, pp. 1230-1233.
- [11] Y. Habiboglu, O. Gunay, A.E. Cetin, Flame detection method in video using covariance descriptors, in: *2011 IEEE International Conference on Acoustics, Speech and Signal Processing (ICASSP)*, Prague, 2011.
- [12] A. Chenebert, T.P. Breckon, A. Gaszczak, A non-temporal texture driven approach to real-time fire detection, in: *ICIP*, Brussels, Belgium, 2011.

- [13] R.T. Collins, A system for video surveillance and monitoring, in: 8th TMRRS, USA, 1999.
- [14] T. Porter, T. Duff, Compositing digital images, *CG* 18 (3) (1984) 253-259.
- [15] R. Yasmin, Detection of Smoke Propagation Direction Using Color Video Sequences, *International Journal of Soft Computing* 4 (1) (2009) 45-48.
- [16] T. Celik, H. Demirel, H. Ozkaramanli, Automatic fire detection in video sequences, in: 14th European Signal Processing Conference [online], Florence, Italy, Sept. 4-8, 2006, [http://www.eurasip.org/Proceedings/Eusipco/](http://www.eurasip.org/Proceedings/Eusipco/Eusipco2006/papers/1568981622.pdf)
- [17] R. Haralick, Statistical and structural approaches to texture, in: *Proceedings of the IEEE*, 1979, pp. 786-804.
- [18] T. Ojala, M. Pietikainen, D. Harwood, A comparative study of texture measures with classification based on feature distributions, *Pattern Recognition*. 29 (1) (1996) 51-59.
- [19] G. Zhao, M. Pietikainen, Dynamic texture recognition using local binary patterns with an application to facial expressions, *IEEE Transactions on Pattern Analysis and Machine Intelligence* 29 (6) (2007) 915-928.



Conductivity and Thermal Properties of PAN Based Polymer Electrolytes for Possible Application in Photo Electrochemical Solar Cells

Warakawe Jayasundara Mudiyansele Jayabahugedara Saumya Rajinie Jayasundara^{1,2}, Tennakoon Mudiyansele Wijendra Jayalath Bandara³, Pierisge Sadeesha Leonard Fernando³, Hewage Dhanushka Naleen Sampath Fernando³, Malavi Achchi Kankanamge Lakshman Dissanayake¹, Lekam Ralalage Anura Kalinga Bandara⁴ and Bengt-Erik Mellander⁵

1. Institute of Fundamental Studies, Kandy 20000, Sri Lanka

2. Postgraduate Institute of Science, University of Peradeniya, Peradeniya 20404, Sri Lanka

3. Department of Physical Sciences, Rajarata University of Sri Lanka, Mihinthale 50300, Sri Lanka

4. Department of Physics, University of Peradeniya, Peradeniya 20404, Sri Lanka

5. Department of Applied Physics, Chalmers University of Technology, Goteborg 41296, Sweden

Received: November 13, 2013 / Accepted: December 4, 2013 / Published: December 25, 2013.

Abstract: Two gel or quasi-solid-state electrolyte complexes based on PAN (polyacrylonitrile) host polymer and salts Hex₄NI (tetrahexylammonium iodide), MgI₂, LiI were prepared by incorporating plasticizers EC (ethylene carbonate) and PC (propylene carbonate). These are: PAN/EC/PC/I₂/Hex₄NI:MgI₂ and PAN/EC/PC/I₂/Hex₄NI:LiI. A clear glass transition was observed around -100 °C for all the electrolyte complexes. In the PAN/EC/PC/I₂/Hex₄NI:MgI₂ system, a decrease in conductivity was observed with the addition of MgI₂ and the electrolyte with Hex₄NI alone as the iodide salt gave the maximum ionic conductivity of 2.51×10^{-3} S·cm⁻¹ at 25 °C. In the PAN/EC/PC/I₂/Hex₄NI:LiI system, an increase in conductivity was observed with the addition of LiI. Consequently the electrolyte with LiI as the only iodide salt gave the maximum ionic conductivity of 3.14×10^{-3} S·cm⁻¹ at 25 °C. The diffusion coefficient (*D*), the mobility (*μ*) and the density of charge carriers (*n*) in the electrolytes were calculated using complex impedance data and equations obtained for dielectric loss tangent. The measured data for dielectric loss tangent were fitted to the model equation. Calculated, *n*, *μ* and *D* values are around $\sim 10^{24}$ m⁻³, $\sim 10^{-7}$ m²·V⁻¹·s⁻¹ and $\sim 10^{-9}$ m²·s⁻¹ respectively for the two electrolyte systems. This type of iodide ion conducting electrolytes could be suitable materials for PEC (photo electrochemical) solar cells.

Key words: Quasi-solid-state, polyacrylonitrile, photoelectrochemical, dielectric.

1. Introduction

Fast ion conductors or electrolytes have many applications in the field of electrochemistry. Polymer electrolytes [1] have attracted much attention because of their use in practical application such as batteries, fuel cells, PEC solar cells, sensors and displays. Anion

conducting PAN based polymer electrolytes are good candidate materials for the fabrication of photo-electrochemical solar cells [2]. Even though the PEC cell efficiencies are better with liquid type electrolytes, the usage of liquid type electrolytes in the cells meets durability issues. Use of polymer electrolytes in solar cell applications shows many advantages such as compatibility, no leakage, easy to prepare in different forms, chemical and physical

Corresponding author: Warakawe Jayasundara Mudiyansele Jayabahugedara Saumya Rajinie Jayasundara, Ph.D. student, research fields: polymer electrolytes and dye sensitized solar cells. E-mail: sjayasundara@yahoo.com.

stability and easy to process [2, 3]. A large number of studies were so far carried out by several groups using variety of single salt systems as electrolyte with the aim of enhancing cell efficiency [3-5]. The present study compares the novel polymer electrolyte different systems with double salts intended for PEC solar cells by analyzing electrical and thermal properties. Especially, the density of charge carriers and mobility in electrolytes were calculated by analyzing complex dielectric measurements.

2. Experiments

2.1 Materials

PAN, LiI, MgI₂, Hex₄N⁺I⁻, iodine (I₂), PC and EC all with purity greater than 98%, all from Aldrich were used as starting materials. Prior to use Hex₄N⁺I⁻ and PAN were vacuum dried for 24 h at 50 °C and LiI was vacuum dried for 4 h at 150 °C in a vacuum oven.

2.2 Gel Electrolyte Preparation

Two gel electrolyte complexes were prepared by keeping the mass fractions of PAN (0.10 g), PC (0.40 g), EC (0.40 g) unchanged and varying the amount of salt according to Table 1. The amount of iodine added was fixed at 0.1 times of the total number of moles of salts in the electrolyte.

Initially the relevant weights of EC, PC and salts were mixed in a closed glass bottle by continuous stirring at 50 °C for about 3 h. Then PAN was added to the mixture which was stirred further keeping it at 40 °C for about 2 h. Finally, iodine was added to the mixture and heated to ~100 °C along with continuous stirring for a few more minutes until a homogeneous viscous solution was obtained. The resulted hot viscous gel was pressed between two glass plates (laboratory microscope glass slides) in order to obtain a quasi-solid-state polymer electrolyte film of a thickness of about 0.5 mm.

2.3 Measurements

The complex impedance measurements were

performed using a HP 4292A RF impedance analyzer in the 10 Hz-10 MHz low frequency range to evaluate the samples. The temperature of the sample varied from 0 °C to 60 °C and the measurements were taken at 5 °C intervals.

DSC (differential scanning calorimetric) thermograms were obtained using a Mettler Toledo DSC 30 differential scanning calorimeter to understand the thermal behavior of the sample. The glass transition temperature (T_g) was extracted from DSC thermograms. Each sample was scanned between -130 °C and 100 °C with a rate of 10 °C min⁻¹. Thermal measurements were carried out with several consequent heating and cooling cycles with the same sample. A flow of nitrogen gas was maintained over the perforated pan to avoid any contact with atmospheric moisture.

3. Theory

The conductivity (σ) of a single ion conducting electrolyte is given by the equation

$$\sigma = ne\mu \quad (1)$$

In order to characterize the electrolyte, it is important to calculate mobility (μ) and charge carrier density (n).

According to the Refs. [5, 6] the effective dielectric constant of an electrolyte sandwiched between two blocking electrodes can be represented by

$$\varepsilon^* = \varepsilon'_\infty \left\{ \left(1 + \frac{\delta}{1 + (\omega\tau)^2 \delta} \right) - i \left(\frac{\omega\tau\delta^{3/2}}{1 + (\omega\tau)^2 \delta} \right) \right\} \quad (2)$$

where, ε'_∞ is the high frequency permittivity, ε^* is the effective complex dielectric constant, ω is the angular frequency of the signal, δ is a constant and τ is the dielectric relaxation time corresponding to the maximum dielectric loss tangent. Therefore, $\tan(\phi)$, the dielectric loss tangent can be obtained by equation

$$\tan(\phi) = \frac{\omega\tau\sqrt{\delta}}{1 + \omega^2\tau^2} \quad (3)$$

The δ is given by

$$\delta = \frac{d}{(D\tau)^{1/2}} = \frac{d}{\lambda} \quad (4)$$

Table 1 Electrolyte composition, where the amount of PAN, PC and EC were kept at 0.10 g, 0.40 g and 0.40 g respectively.

System (1)	PAN/EC/PC/I ₂ /Hex ₄ NI:MgI ₂						
Electrolyte	A1	B1	C1	D1	E1	F1	G1
MgI ₂ / g	0.00	0.02	0.04	0.06	0.08	0.10	0.12
Hex ₄ N ⁺ I ⁻ / g	0.12	0.10	0.08	0.06	0.04	0.02	0.00
I ₂ / g	0.0063	0.0071	0.0078	0.0086	0.0094	0.0102	0.0109
System (2)	PAN/EC/PC/I ₂ /Hex ₄ NI:LiI						
Electrolyte	A2	B2	C2	D2	E2	F2	G2
LiI / g	0.00	0.02	0.04	0.06	0.08	0.10	0.12
Hex ₄ N ⁺ I ⁻ / g	0.12	0.10	0.08	0.06	0.04	0.02	0.00
I ₂ / g	0.0063	0.0090	0.0118	0.0145	0.0173	0.0200	0.0227

$$D = \frac{d^2}{\delta^2 \tau} \quad (5)$$

where, $2d$ and λ are sample length and the Debye length. The Nernst-Einstein relation gives the relationship between the mobility (μ) and the diffusion coefficient (D).

$$\mu = \frac{eD}{k_B T} \quad (6)$$

Charge carrier density (n) is given by Eq. (5), where, k_B is the Boltzmann constant, σ is the conductivity and T is the absolute temperature.

$$n = \frac{\sigma k_B T}{e^2 D} \quad (7)$$

The conductivity (σ) can be calculated using

$$\sigma = \frac{l}{RA} \quad (8)$$

where, l is the sample length ($2d$), R is the resistance and A is the area of the sample.

4. Results and Discussion

Two different quasi-solid-state electrolyte systems were compared in this study. System 1 is PAN/EC/PC/I₂/Hex₄NI:MgI₂ electrolyte and system 2 is PAN/EC/PC/I₂/Hex₄NI:LiI electrolyte. The conductivity variation as a function of $1,000/T$ is shown in Fig. 1 for system 1. Eq. (8) was used to calculate the conductivity. Hex₄NI alone as the iodide salt (sample A1) gave the maximum ionic conductivity, $2.51 \times 10^{-3} \text{ S cm}^{-1}$ at 25 °C out of samples in system 1. In this PAN/EC/PC/I₂/Hex₄NI:MgI₂ system, a reduction in conductivity is observed with added amount

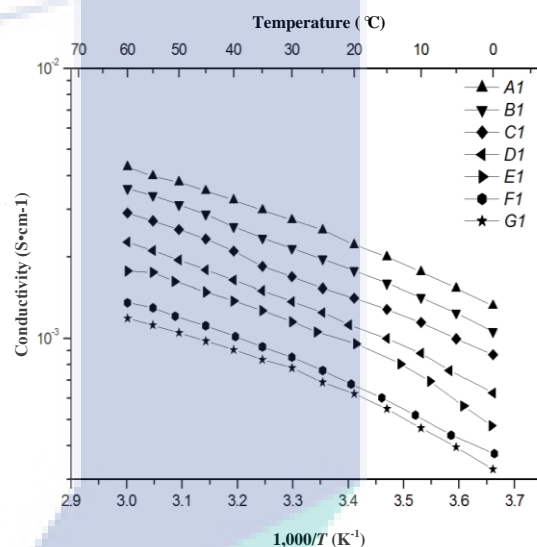


Fig. 1 Conductivity vs. $1,000/T$ for PAN/EC/PC/Hex₄NI: MgI₂ electrolytes containing different Hex₄NI and MgI₂ compositions as given in Table 1.

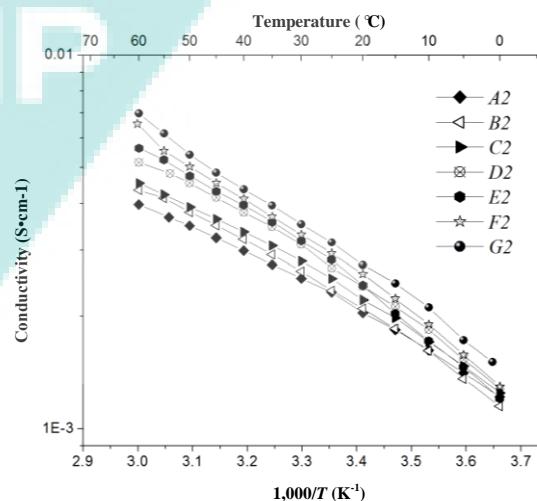


Fig. 2 Conductivity vs. $1,000/T$ for PAN/EC/PC/Hex₄NI: LiI electrolytes containing different Hex₄NI and LiI compositions as given in Table 1.

of MgI_2 (Fig. 1) which may be a result of cross link formation of Mg^{2+} ions with CN groups in PAN chains [4]. Hence, the lowest conductivity is given by sample G1. Higher flexibility in polymer chains is necessary to obtain higher conductivity. The higher the cross links the lower the polymer flexibility, leading to lower the conductivity.

In system 2 (PAN/EC/PC/I₂/Hex₄Ni:LiI), an increase in conductivity is observed with added amount of LiI (Fig. 3). The maximum ionic conductivity of $3.14 \times 10^{-3} \text{ S}\cdot\text{cm}^{-1}$ at 25 °C is shown by the sample which contained only the LiI salt (sample G2). In system 1, neither Hex₄N⁺ nor Mg²⁺ is moving since Hex₄N⁺ is a bulky cation and Mg²⁺ can form cross links [2-4]. In the present system, Li⁺ ion can be considered as a moving ion and contributes to the conductivity [7, 8]. The mobility of Li⁺ ion is higher than that of Hex₄N⁺ and Mg²⁺. The increasing trend in T_g observed with added amount of LiI reveals the reduction of flexibility of polymer chains with LiI amount. This may be a result of ionic complexes and undissolved solutes at higher LiI concentrations.

Eqs. (5)-(7) were used to calculate D , μ and n . The parameters δ and τ were obtained by fitting measured data to Eq. (3).

Calculated values D , μ , n for system 1 (in Table 2) also show minimum at the sample G1 (sample which contained only the salt MgI_2) providing evidence for

the observed lower conductivity. Highest mobility value of $6 \times 10^{-7} \text{ m}^2\cdot\text{V}^{-1}\cdot\text{S}^{-1}$ observed for the system 1 containing only the Hex₄Ni salt (sample A1) may be an effect of presence of large Hex₄N⁺ ion where large cations can place within the polymer network making polymer chains more separated and flexible. Diffusion coefficient values also shows maximum at sample A1 by giving $2 \times 10^{-8} \text{ m}^2\cdot\text{s}^{-1}$. In general electrolyte containing LiI has shown higher mobilities than that of containing MgI_2 . This can be due to the ability of Mg^{2+} ions to make stronger interactions with ionic species in the electrolyte than Li⁺ ions.

Fig. 3 shows the DSC thermograms of electrolyte systems 1 and 2. All the samples have shown clear glass transition at around 100 °C. The T_g (glass transition temperature) also can be related to the flexibility of the polymer chains [9, 10] and the highest T_g is observed for the electrolyte containing only the MgI_2 salt (sample G1). Low T_g values were observed for the samples which contained salt mixtures and this may be a result of increased flexibility in polymer chains due to structural disorders imposed by small and large cations. Lower T_g values are shown for the electrolytes containing MgI_2 and then that of sample containing LiI. For electrolyte sample preparation the weights ratio of the salts were kept fixed. Since LiI has lower molar weight than other iodides in these electrolytes, the

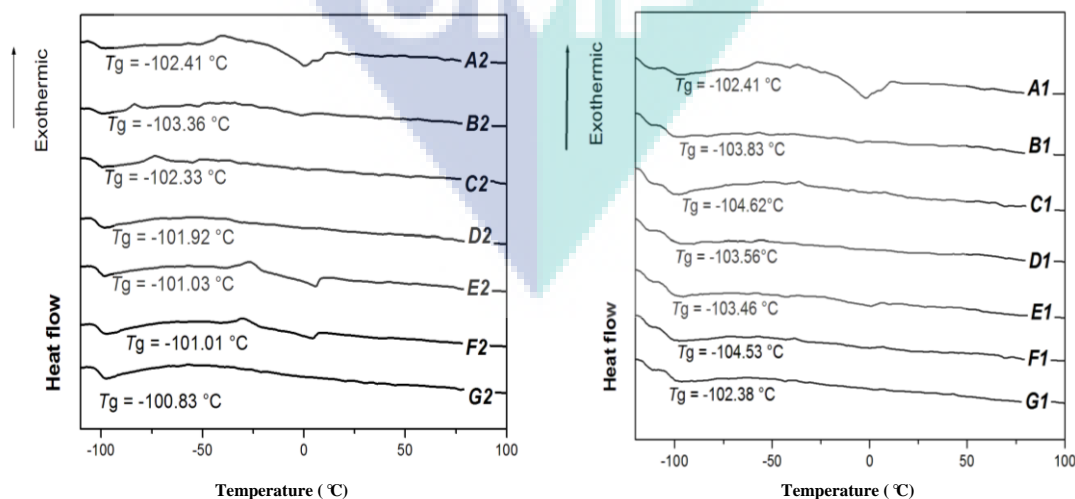


Fig. 3 DSC thermograms of electrolyte samples given in Table 1 under heating rate of $10 \text{ }^\circ\text{C min}^{-1}$.

Table 2 The diffusion coefficient (D), the mobility (μ) and the density of charge carriers (n) of some electrolyte samples at 25 °C.

Sample	D ($\text{m}^2 \cdot \text{S}^{-1}$)	μ ($\text{m}^2 \text{V}^{-1} \cdot \text{S}^{-1}$)	n (m^{-3})
System 1	PAN/EC/PC/I ₂ /Hex ₄ NI :MgI ₂		
A1	2×10^{-8}	6×10^{-7}	2×10^{24}
B1	6×10^{-9}	5×10^{-7}	5×10^{24}
E1	5×10^{-9}	2×10^{-7}	3×10^{24}
F1	6×10^{-9}	2×10^{-7}	2×10^{24}
G1	8×10^{-10}	3×10^{-8}	9×10^{23}
System 2	PAN/EC/PC/I ₂ /Hex ₄ NI :LiI		
A2	2×10^{-8}	6×10^{-7}	2×10^{24}
B2	1×10^{-8}	4×10^{-7}	3×10^{24}
E2	4×10^{-8}	2×10^{-6}	2×10^{24}
F2	3×10^{-8}	2×10^{-6}	2×10^{24}
G2	7×10^{-9}	3×10^{-7}	7×10^{24}

number of ions in LiI containing electrolytes are higher. Hence, number of intermolecular interactions is higher for the electrolytes in system 2 leading higher T_g .

5. Conclusions

Two gel type or quasi solid state electrolyte systems namely PAN/EC/PC/I₂/Hex₄NI:MgI₂ and PAN/EC/PC/I₂/Hex₄NI:LiI were prepared and complex impedance measurements and differential scanning calorimetric measurements were carried out. The diffusion coefficient, the mobility and the density of charge carriers in the electrolytes were calculated using complex impedance data and equations obtained for dielectric loss tangent. In the PAN/EC/PC/I₂/Hex₄NI:MgI₂ system a decrease in conductivity was observed with the increasing of MgI₂ amount while an increase in conductivity was observed with the increasing of LiI amount in the system PAN/EC/PC/I₂/Hex₄NI:LiI. All the samples show clear glass transition temperature around -100 °C. The resulted values for the density of charge carriers, the mobility and the diffusion coefficient are around 10^{24} m^{-3} , $10^{-7} \text{ m}^2 \cdot \text{V}^{-1} \cdot \text{s}^{-1}$ and $10^{-9} \text{ m}^2 \cdot \text{s}^{-1}$. These types of iodide ion conducting electrolytes are suitable to use in photoelectrochemical solar cells.

Acknowledgments

Research support from The National Research

Council Sri Lanka (Grant 11-196), as well as from the Swedish Research Council is gratefully acknowledged.

References

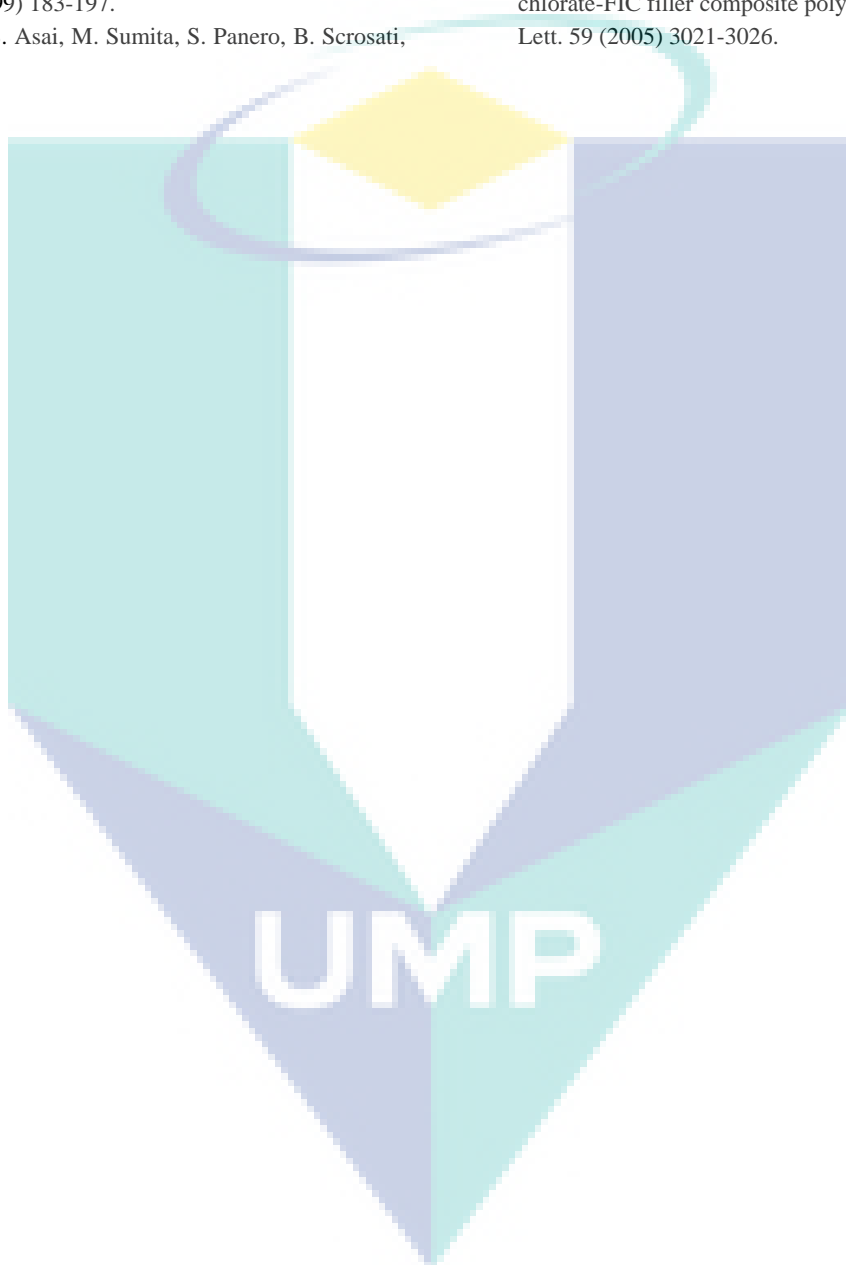
- [1] M.B. Armand, M.J. Chabagno, M.J. Duclot, Fast ion transport in solids, Elsevier North Holland, New York, 1979, pp. 131-136.
- [2] T.M.W.J. Bandara, M.A.K.L. Dissanayake, W.J.M.J.S.R. Jayasundara, I. Albinsson, B.E. Mellander, Efficiency enhancement in dye sensitized solar cells using gel polymer electrolytes based on a tetrahexylammonium iodide and MgI₂ binary iodide system, J. Physical Chemistry Chemical Physics 14 (2012) 8620-8627.
- [3] T. Svensson, T.M.W.J. Bandara, E. Lundell, I. Svensson, M. Furlani, I. Albinsson, B.E. Mellander, Estimation of ion transport parameters by modeling space charge relaxation in PEO based solid polymer electrolyte intended for photoelectrochemical solar cells, in: Proceedings of Solar Asia 2011 Int. Conf., Institute of Fundamental Studies, Kandy, Sri Lanka, 2011, pp. 221-227.
- [4] T.M.W.J. Bandara, M.A.K.L. Dissanayake, I. Albinsson, B.E. Mellander, Dye-sensitized nono-porus TiO₂ solar cell with Polyacrylonitrile: MgI₂ plasticized electrolyte, J. Power Sources 195 (2010) 3730-3734.
- [5] T.M.W.J. Bandara, M.A.K.L. Dissanayake, I. Albinsson, B.E. Mellander, Mobile charge carrier concentration and mobility of a polymer electrolyte containing PEO and Pr₄N⁺T using electrical and dielectric measurements, Solid State Ionics 189 (2011) 63-68.
- [6] T.M.W.J. Bandara, B.E. Mellander, Evaluation of mobility, diffusion coefficient and density of charge carriers in ionic liquids and novel electrolytes, In: Alexander Kokorin (Ed.), Ionic Liquids: Theory,

Properties, New Approaches, In Tech, Rijeka, Croatia, 2011, pp. 383-406.

- [7] A.M. Stephan, Review on gel polymer electrolytes for lithium-ion batteries, *Eur. Polym. J.* 42 (2006) 21-42.
- [8] J.Y. Song, Y.Y. Wang, C.C. Wan, Review of gel-type polymer electrolytes for Lithium-Ion batteries, *J. Power Sources* 77 (1999) 183-197.
- [9] Y. Tominaga, S. Asai, M. Sumita, S. Panero, B. Scrosati,

A novel composite polymer electrolyte: Effect of mesoporous SiO₂ on ionic conduction in poly (ethylene oxide)-LiCF₃SO₃ complex, *J. Power Sources* 146 (2005) 402-406.

- [10] Y.J. Wang, Y. Pan, L. Wang, M.J. Pang, L. Chen, Conductivity studies of plasticized PEO-Lithium chlorate-FIC filler composite polymer electrolytes, *Mater. Lett.* 59 (2005) 3021-3026.



The Use of EKF to Estimate the Transient Thermal Behaviour of Induction Motor Drive

Mellah Hacene^{1,2} and Hemsas Kamel Eddine^{1,2}

1. *Electrical Engineering Department, Faculty of Technology, Ferhat Abaas Setif 1 University, Maabouda 19000, Algeria*

2. *LAS (Setif Automatic Laboratory), Faculty of Technology, Ferhat Abaas Setif 1 University, Maabouda 19000, Algeria*

Received: July 24, 2013 / Accepted: October 8, 2013 / Published: December 25, 2013.

Abstract: In this paper, a survey is conducted to examine the problem of estimating the states and parameters of an asynchronous machine when some of these measures are not available or the estimation approach is the best solution. The modeling is based on the theory of power dissipation; heat transfer and the rate of temperature increase the stator and the rotor, taking into account the effect of speed on trade. The first purpose of this article is displayed the effect of variable losses depending on the load and constant losses on the thermal behavior of asynchronous motor. According to the sensor's problems and the obtaining of the thermal information about the rotor, the second goal is the use of a sensorless method like the use of the EKF (extended Kalman filter), some simulation results are given and commented.

Key words: Induction machines, electrical machine losses, thermal models, thermal study, Kalman filter.

1. Introduction

Nowadays, the asynchronous machine is used more and more in the industrial domain. Indeed, it is appreciated for its standardization, its great robustness and its low costs of purchase and maintenance. For several years, we have noticed the widening of the scientific and manufacturer works concerning the drive of these machines [1]. The research of the electromechanical devices more and more flexible supported the appearance of the new particularly powerful systems. These systems generally rest on the association of an electronic device, allowing the control of the global system, and a rotating machine ensuring electromechanical conversion [1], however the increase in the specific powers and the use of novel control modes induce the harmonics of time [2] with frequencies beyond the audible aria, even with square wave voltages [1], the adaptation of our machines to

this new applications generates more important internal heating. A rigorous study of the thermal behavior of the electric machines is increasingly necessary [2].

Many authors describe the use of sensor as solution to the thermal problems of the induction machine [3] like infra-red sensor [4, 5], thermocouple [4, 6-9], on the other hand, the first one gives a surface temperature measurement so the measurement is not accurate [3], and the second one can require some machining for a correct placement, but it has the merit to be able to provide internal temperatures in exiguous places of the machine [3].

The problem of obtaining the rotors thermal information gene the sensor measurement procedure to be successful, however some solutions in the specialized literature can be cited, an optical link between the stator and the rotor proposed in Refs. [4, 6, 10, 11] proposes an industrial rotary transformer, using a rings and brushes [4], a high frequency or infrared modules, all these methods are discussed in Ref. [3]. In addition to the stator and the rotor, the use of sensors

Corresponding author: Mellah Hacene, Ph.D. student, research fields: electrical machines, state estimation, wind energy and finite element. E-mail: has.mel@gmail.com.

increases the installation cost and practically all sensors are fragile and render the installation most complex. Access to the rotor flux, current, speed and temperature which eliminate all out sensors and make our installation less complex, these states estimates can be used for the sensorless control. In addition, the resistances values derived from the corresponding estimated temperatures resolve the weak observability of the stator resistance at high speed and rotor resistance at low torque, so we will have a more robust control in all operating modes. The estimated temperatures may be used in the monitoring processes and avoid overheating of our machine therefore increased its operational life. Finally the advantages of this approach motor are reduced hardware complexity and lower cost, reduces size of the drive machine, elimination of the speed, current and thermal sensors.

2. Thermal Modeling Methods

In the specialized literature we can gather the thermal modeling methods of the electrical machines under the following three types.

2.1 Simple Modeling

We find many simple approaches in the literature in order to give bonds between the stator temperature and the rotor temperature. Beguenane and Benbouzid [12, 13] thus present an electrical rotor resistance identification method, which is unfortunately unable to identify the stator resistance; however these articles propose two thermal approaches to bind two resistances of the electric model:

(1) The first method is based on the EDF (French Electricity Board) experiment. It considers that the rotor has a temperature higher of 10 °C than that the stator temperature;

(2) The second method is based on work of Kubota. It gives a simple relation of proportionality between two resistances calibrated on the face values of the maker badge. We find the proportionality method in other articles like Ref. [14]. On the other hand, later

works were realized on EDF model and put a flat as for its validity for all the operating processes, especially NEMA design D machines with 8-13% slip [15].

2.2 Fine Modeling

It is based on the use of the finite element method with a detailed model geometric and mechanics.

This makes it possible to obtain a complete cartography of the machine temperatures (Fig. 1). These results are very interesting since they make it possible to give an idea of the places where the temperature becomes critical according to the operations and answer the problems of the hot points [16, 17].

2.3 Electrical Equivalent Supply Networks (NODAL Method) [18, 19]

Those generally model the whole of the machine with nodes of temperature associated with each material used in Ref. [10]. The identification of this model is thus carried out either by finite elements, or by a great number of points of temperature measurement within the machine. These models are generally very detailed (Fig. 2) and thus too complex for our application in real time [10].

As our goal principal is the use of Kalman filter, these two types of models are not exploitable, because these methods do not give the formalism of state.

2.4 Simplified Models

Other researchers sought to simplify the models by gathering the losses in subsets and by approximating the temperature in an unspecified point with a simple exponential answer that one can simply represent by a resistance and a heat capacity (Fig. 3) [7, 20].

3. Thermal Modeling of the IM in the State Space

In many cases, the model is the familiar steady-state equivalent circuit, but for high performance drives, a full transient model of the motor is required. Effective

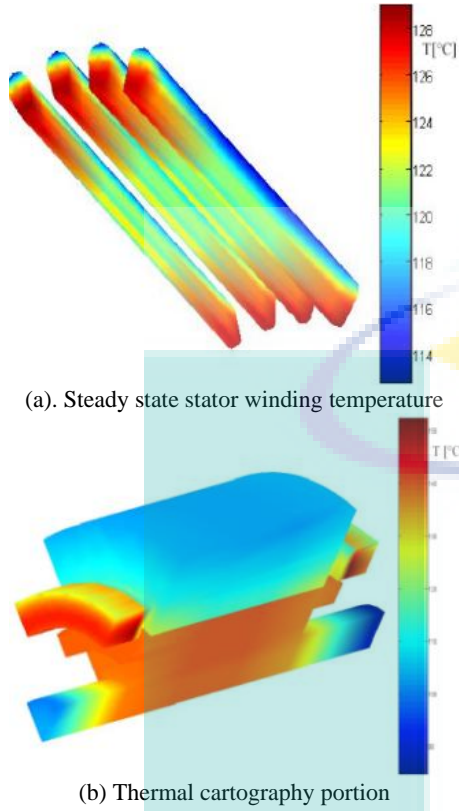


Fig. 1 Thermal cartography portion of an asynchronous machine, obtained by finite elements [11].

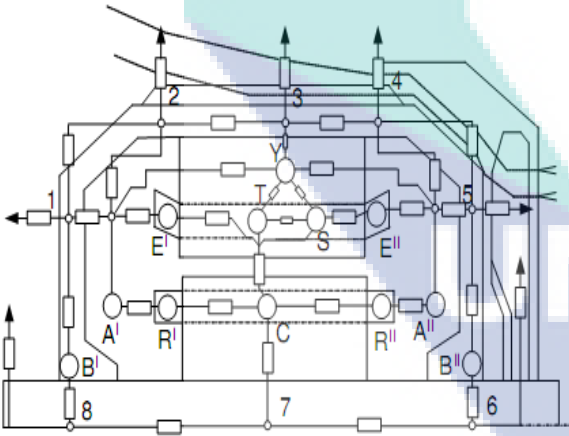


Fig. 2 Equivalent thermal models of the asynchronous machine [10].

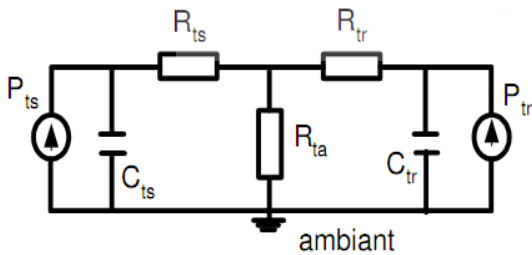


Fig. 3 Thermal model of the asynchronous machine [7].

modeling, and therefore the effectiveness of drive control and estimation, is limited by the complexity of the physical processes occurring within the motor. Frequency dependence of the rotor electrical circuit, nonlinearity of the magnetic circuit, and temperature dependence of the stator and rotor electrical circuits all impact on the accuracy with which the motor can be modeled [21]. The modeling of the IM taking all the real behaviors without hypothesis simplifications will be very difficult or impossible. For that, one will suppose a model with simplifying assumptions. This paper addresses the third of these effects (temperature dependence) by incorporating a thermal model of the motor in the estimation process. The frequency dependence of the rotor electrical circuit and nonlinearity of the magnetic circuit are not included.

Temperature estimation in the induction motor has been dealt with by many authors [11, 19], but most of these publications describe either a very complex lumped-parameter network or the finite-element method.

A state-variable model of the induction motor is required for the EKF algorithm. The twin-axis stator reference frame [21] is used to model the motor's electrical behavior, because physical measurements are made in this reference frame; the well-known linear relationship between resistance and temperature must be taken into account for the stator and rotor resistances:

$$\begin{aligned} R_s(\theta_s) &= R_{s0}(1 + \alpha_s \theta_s) \\ R_r(\theta_r) &= R_{r0}(1 + \alpha_r \theta_r) \end{aligned} \quad (1)$$

where, R_{s0} , R_{r0} stator and rotor resistance at the ambient temperature, α_s and α_r them coefficients thermal, respectively. In the IM traditional models, one replace R_s and R_r by $R_s(\theta_s)$ and $R_r(\theta_r)$ respectively, what can be rearranged in space of state on the format:

$$p \delta i_{qr} = -L_1 L_m \omega_r i_{ds} - R_s(\theta_s) L_2 i_{qs} - L_1 L_2 \omega_r i_{dr} + R_r(\theta_r) L_1 i_{qr} + L_m V_{qs} \quad (2)$$

$$p \delta i_{ds} = -R_s(\theta_s) L_2 i_{ds} + L_m^2 \omega_r i_{qs} + R_r(\theta_r) L_m i_{dr} + L_2 L_m \omega_r i_{qr} + L_2 V_{ds} \quad (3)$$

$$p \delta i_{dr} = R_s(\theta_s) L_m i_{ds} - L_1 L_m \omega_r i_{qs} - R_r(\theta_r) L_1 i_{dr} - L_1 L_2 \omega_r i_{qr} + L_2 V_{qs} \quad (4)$$

$$p \delta i_{qs} = -L_m^2 \omega_r i_{ds} - R_s(\theta_s) L_2 i_{qs} - L_2 L_m \omega_r i_{dr} + R_r(\theta_r) L_m \omega_r i_{qr} + L_2 V_{qs} \quad (5)$$

where $\delta = L_1 L_2 - L_m^2$.

The mechanical behavior can be modeled by

$$T = b \omega_r + j p \omega_r + T_L \quad (6)$$

However, the electromagnetic torque of the motor T can be represented in term of stator and rotor current components:

$$T = p_n L_m (i_{qs} i_{dr} - i_{ds} i_{qr}) \quad (7)$$

By equality of these two preceding equations, the equation speed of rotor in the space of state is

$$p \omega_r = p_n L_m (i_{qs} i_{dr} - i_{ds} i_{qr}) - \frac{b}{j} \omega_r + \frac{T_L}{j} \quad (8)$$

The thermal model is derived by considering the power dissipation, heat transfer and rate of temperature rise in the stator and rotor. The stator power losses include contributions from copper losses and frequency-dependent iron losses [21].

$$p L_s = (i_{qs} i_{dr} - i_{ds} i_{qr}) R_s(\theta_s) + k_{ir} \omega_r \quad (9)$$

where K_{ir} is it constant of iron loss.

The rotor power losses are dominated by the copper loss contribution if the motor is operated at a low value of slip so

$$p L_r = (i_{dr}^2 - i_{qr}^2) R_r(\theta_r) \quad (10)$$

where, H_s , H_r are the stator and the rotor heat capacity respectively.

A simple representation of the assumed heat flow is given in Fig. 1. Heat flow from the rotor is either directly to the cooling air with heat transfer coefficient k_2 , or across the air gap to the stator with heat transfer coefficient k_3 .

$$p L_r = k_2 \theta_r + H_r p \theta_r + k_3 (\theta_r - \theta_s) \quad (11)$$

Heat flow from the stator is directly to the cooling air, with heat transfer coefficient k_1 :

$$p L_s = k_1 \theta_s + H_s p \theta_s - k_3 (\theta_r - \theta_s) \quad (12)$$

For an induction motor with a shaft mounted

cooling fan, the heat transfer coefficients are dependent on the rotor speed. This dependence has been modeled approximately by a set of linear relationships:

$$k_1 = k_{10} (1 + k_{1\omega} \omega_r) \quad (13)$$

$$k_2 = k_{20} (1 + k_{2\omega} \omega_r) \quad (14)$$

$$k_3 = k_{30} (1 + k_{3\omega} \omega_r) \quad (15)$$

where, k_{10} , k_{20} and k_{30} thermal power transfer coefficients at the zero speed. $k_{1\omega}$, $k_{2\omega}$ and $k_{3\omega}$ variation of thermal power transfer with speed.

The following equations are found with simple mathematical manipulations:

$$p \theta_s = \frac{R_s(\theta_s)}{H_s} (i_{ds}^2 + i_{qs}^2) + \frac{k_{ir}}{H_s} \omega_r^2 - \frac{k_{10} (1 + k_{1\omega} \omega_r)}{H_s} \theta_s + \frac{k_{30} (1 + k_{3\omega} \omega_r)}{H_s} (\theta_s - \theta_r) \quad (16)$$

$$p \theta_r = \frac{R_r(\theta_r)}{H_r} (i_{dr}^2 + i_{qr}^2) - \frac{k_{20} (1 + k_{2\omega} \omega_r)}{H_r} \theta_r + \frac{k_{30} (1 + k_{3\omega} \omega_r)}{H_r} (\theta_s - \theta_r) \quad (17)$$

The whole of preceding Eqs. (2), (5), (8), (16), and (17) give us the model of following state:

$$\begin{aligned} p \delta i_{qr} &= -L_1 L_m \omega_r i_{ds} - R_s(\theta_s) L_2 i_{qs} - L_1 L_2 \omega_r i_{dr} \\ &\quad + R_r(\theta_r) L_1 i_{qr} + L_m V_{qs} \\ p \delta i_{ds} &= -R_s(\theta_s) L_2 i_{ds} + L_m^2 \omega_r i_{qs} + R_r(\theta_r) L_m i_{dr} \\ &\quad + L_2 L_m \omega_r i_{qr} + L_2 V_{ds} \\ p \delta i_{dr} &= R_s(\theta_s) L_m i_{ds} - L_1 L_m \omega_r i_{qs} - R_r(\theta_r) L_1 i_{dr} \\ &\quad - L_1 L_2 \omega_r i_{qr} + L_2 V_{qs} \\ p \delta i_{qs} &= -L_m^2 \omega_r i_{ds} - R_s(\theta_s) L_2 i_{qs} - L_2 L_m \omega_r i_{dr} \\ &\quad + R_r(\theta_r) L_m \omega_r i_{qr} + L_2 V_{qs} \\ p \omega_r &= p_n L_m (i_{qs} i_{dr} - i_{ds} i_{qr}) - \frac{b}{j} \omega_r + \frac{T_L}{j} \\ p \theta_s &= \frac{R_s(\theta_s)}{H_s} (i_{ds}^2 + i_{qs}^2) + \frac{k_{ir}}{H_s} \omega_r^2 - \frac{k_{10} (1 + k_{1\omega} \omega_r)}{H_s} \theta_s \\ &\quad + \frac{k_{30} (1 + k_{3\omega} \omega_r)}{H_s} (\theta_s - \theta_r) \\ p \theta_r &= \frac{R_r(\theta_r)}{H_r} (i_{dr}^2 + i_{qr}^2) - \frac{k_{20} (1 + k_{2\omega} \omega_r)}{H_r} \theta_r \\ &\quad + \frac{k_{30} (1 + k_{3\omega} \omega_r)}{H_r} (\theta_s - \theta_r) \end{aligned} \quad (18)$$

4. Simulation Results of the State Space Thermal Model

Eq. (18) is resolved by Matlab using the Runge-Kutta algorithm.

(1) Case of the temporary mode or a complete thermal cycle of the asynchronous machine (duty type S2):

This mode is characterized by the application of a constant load on a finite time interval followed by a rest leading to return to the ambient temperature. For this, a resistive torque of 5 Nm is applied, then we made a stop at $t = 300$ min.

In a general way, in transient and steady state modes, the temperature limit is reached in the stator before the rotor in the case of low power machines (< 37 kW) [14, 22].

At the starting the stator and rotor windings temperature is equal to the ambient temperature (0°C), the thermal transient is very slow over the thermal dynamics of the stator is faster than the rotors dynamics [23].

The interval of time ($t = 0$ min at $t = 300$ min) is an induction motor heating cycle, for against the time interval ($t = 300$ min to $t = 650$ min) is a time of deenergization to allow the motor to cool down before the next startup as presented on in Fig. 4.

(2) Slow continuous-operation periodic duty cycles: this operation mode can be identified by specification of the load period tp , no-load period tv and cycle duration Te , but also by the relative duty cycle tr in % write like this:

$$tr\% = tp/Te \times 100 \quad (19)$$

In this case the load torque is equal to 10 Nm.

For this application $tp = 350$ min, $tv = 100$ min and $Te = 450$ min, so $tr\% = 77.77\%$.

(3) Case of intermittent operation (duty type S3):

This cyclic regime is characterized by the application of a constant load over periods tp separate rest period tv without returning to ambient temperature, in our case we take the values $Te = 150$ min, $tp = 100$ min and $tv = 50$ min, so, $tr = 66.66\%$.

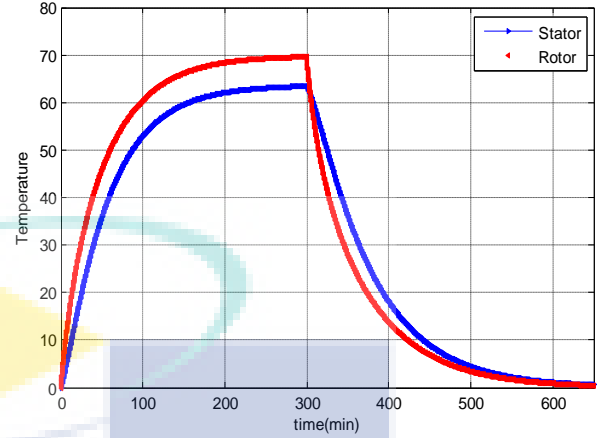


Fig. 4 Case of the temporary mode or duty type S2.

By comparison between the two duty operations mode slow (Fig. 5) and fast (Fig. 6), we can see that the IM in the slow operation mode is naturally itself cooled at Δtv (100 min), but in the second mode the Δtv is small (50 min) so the IM cannot cool naturally.

5. Application of the EKF

A reconstructor of state or estimator is a system having like entry, the entries and the exits of the real process, and whose exit is an estimate of the state of this process (Fig. 7). The extended Kalman filter algorithm takes account of process and measurement noise in a general nonlinear system:

$$\begin{cases} x(k+1) = Ax(k) + Bu(k) + w(k) \\ y(k) = Cx(k) + v(k) \end{cases} \quad (20)$$

where, $w(k)$, $v(k)$ represents the process and measurement noise respectively.

(1) The prediction stage is

$$\hat{x}(k+1) = f(\hat{x}(k), u(k)) \quad (21)$$

$$P(k+1) = F(k)P(k)F^T + Q \quad (22)$$

(2) The correction stage is

$$K(k+1) = P(k+1)C^T (CP(k+1)C^T + R)^{-1} \quad (23)$$

$$P(k+1/k) = P(k+1) + K(k+1)CP(k+1) \quad (24)$$

$$\begin{aligned} \hat{x}(k+1/k) &= \hat{x}(k+1) + \\ &K(k+1)\{y(k+1) - C\hat{x}(k+1)\} \end{aligned} \quad (25)$$

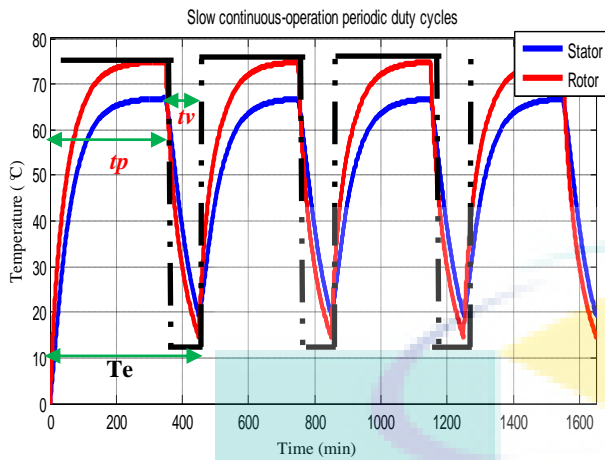


Fig. 5 Case of slow intermittent operation or duty type S3.

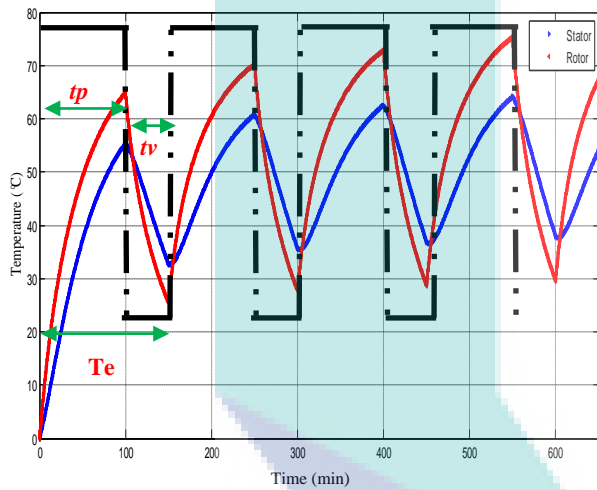


Fig. 6 Case of fast intermittent operation or duty type S3.

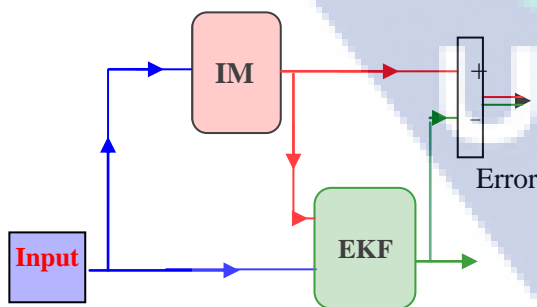


Fig. 7 Application of EKF in IM.

(3) Covariance matrices initial values

The matrix of covariance of error in estimation P and square of 7×7 , translated the confidence that we can have in the adopted model [21] gives it:

$$p(0) = \text{diag} [5 \ 5 \ 5 \ 5 \ 2 \ 1 \ 1] \quad (26)$$

The matrix of covariance of the noise of state Q quantifies the precision of the model and allows the dynamic adjustment of the parameters. It is generally difficult to determine because the direct observation of the state of the system is impossible. It is given in Ref. [21] by

$$Q\% = \text{diag}([1.2 \ 1.2 \ 0.3 \ 0.01 \ 10^{-5} \ 10^{-4}]) \quad (27)$$

The matrix of covariance of noise of measurement R translated the level of noise to the measure is given in Ref. [21] by

$$R\% = 0.22 \begin{bmatrix} 1 & 0 \\ 0 & 1 \end{bmatrix} \quad (28)$$

6. Simulation Results

6.1 Constant Load

The two temperatures thermal model and estimation vary at different rates because of the differences in the losses, thermal capacities and the power transfer coefficients between the stator and rotor.

The stator and rotor temperature in the established mode reached the value $65 \text{ }^\circ\text{C}$, $72 \text{ }^\circ\text{C}$ respectively but their value considered to reach $62.3 \text{ }^\circ\text{C}$ and $69.6 \text{ }^\circ\text{C}$.

Fig. 8 shows that deference between the rotor and the stator temperature is about $10 \text{ }^\circ\text{C}$ verified EDF experiment (The EDF experiment which considers that the rotor has a temperature higher of $10 \text{ }^\circ\text{C}$ than that of the stator) [15].

6.2 Variable Load

In order to verify the model performance for variable load, some step of load variations are applied ($100\% \rightarrow 120\% \rightarrow 50\% \rightarrow 75\%$ of the rated load).

Figs. 9 and 10 show the simulation result of EKF and thermal model temperature of stator and rotor winding under the variable load condition, the deference between the thermal model temperature and EKF is about $2.4 \text{ }^\circ\text{C}$ and $2.7 \text{ }^\circ\text{C}$ for the stator and the rotor, respectively.

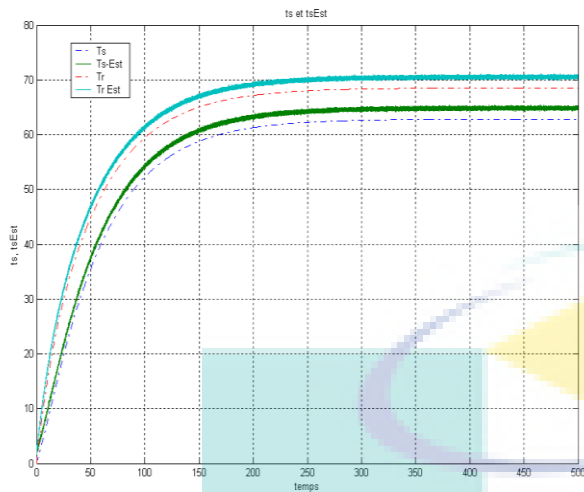


Fig. 8 Stator and rotor temperatures under constant load condition.

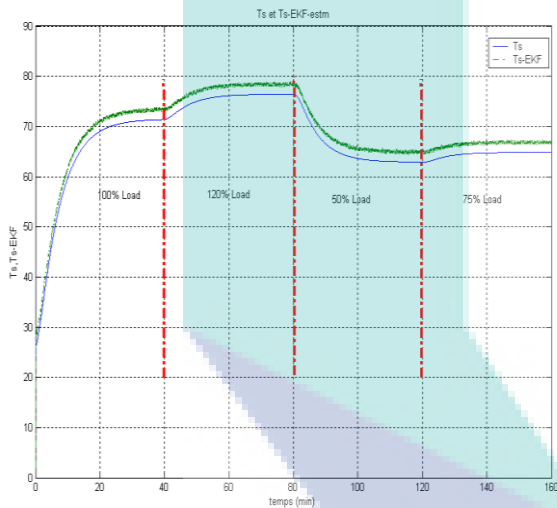


Fig. 9 Stator temperature under variable load condition.

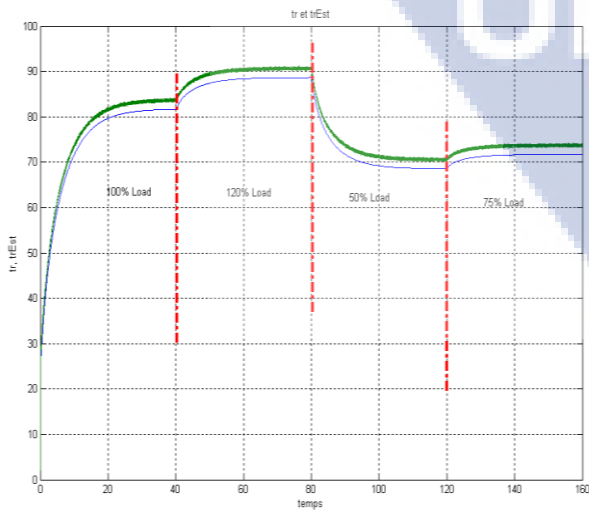


Fig. 10 Rotor temperature under the variable load condition.

7. Conclusions

In this article, we presented a thermal model of a cage induction machine. This model is based on the theory of power dissipation, heat transfer and the rate of temperature increase in the rotor and stator, taking into account the effect of speed on the exchange, simulation tests (duty type S2 and duty type S3) was done up to the validity of the thermal model.

Since the sensors can be not very reliable or expensive, in addition, the problems of the extraction to thermal information about the rotor are difficult or very expensive. The use of a sensorless approach is strongly recommended. The EKF makes it possible to achieve this goal, and the EKF enables to estimate simultaneously the rotor currents, speed, stator and rotor temperature using only the measurable states, a Gaussian noise has been added to take into account the stator current and voltage sensor noises to make a robust estimate.

The simulation study demonstrating that the temperature rise calculation with proposed simplified thermal model in this paper is feasible compared with similar researches. According to our results, the simplified thermal model can be used to estimate both steady state and transient state temperature. In the future, our works will be focused to the thermal monitoring by using EKF.

References

- [1] J.P. Bellomo, Th. Lebey, Fr. Peltier, J.M. Oraison, Consequences of the new drive forms on materials of the stator insulation, *J. Phys. III France* 7 (1997) 993-1008.
- [2] R. Glises, G. Hostache, J.M. Kauffmann, Simulation of the thermal behavior of an asynchronous motor in steady state has external cooling: Study by finite elements, *J. Phys. III France* 4 (1994) 1723-1735.
- [3] H. Mellah, Estimate of the intrinsic quantity of an asynchronous machine, Master Thesis, Ferhat Abaas de Setif University, Algeria, 2009.
- [4] L. Michalski, K. Eckersdorf, J. Kucharski, J. McGhee, *Temperature Measurement*, John Wiley & Sons Ltd., USA, 2001.
- [5] E. Foulon, Extended Kalman Filter for the thermal monitoring of the asynchronous machine, in: Sixth

- Conference of the Young Researchers in Electronic Engineering, Saint-Nazaire, 2003.
- [6] H. Yahoui, G. Grellet, Measurement of physical signals in rotating part of electrical machine by means of optical fiber transmission, in: Proceedings of IEEE Instrumentation and Measurement Technology Conference (IMTC-96), Jun. 4-6, 1996, pp. 591-596.
- [7] K.D. Hurst, T.G. Habetler, A thermal monitoring and parameter tuning scheme for induction machines, in: IEEE Industry Applications Conference, Thirty-Second IAS Annual Meeting, New Orleans, USA, 1997.
- [8] E. Chauveau, E.H. Zaim, D. Trichet, J. Fouladgar, A statistical approach of temperature calculation in electrical machines, *IEEE Transactions on Magnetics* 36 (4) (2000) 1826-1829.
- [9] S.B. Lee, T.G. Habetler, An on-line stator winding resistance estimation technique for temperature monitoring of line-connected induction machines, in: IEEE Industry Applications Conference, Thirty Sixth IAS Annual Meeting, Chicago, Illinois, USA, 2001.
- [10] Z. Lazarevic, R. Radosavljevic, P. Osmokrovic, A novel approach for temperature estimation in squirrel-cage induction motor without sensors, *IEEE Transactions on Instrumentation and Measurement* 48 (3) (1999) 753-757.
- [11] E. Chauveau, Contribution to the electromagnetic and thermal calculation of the electric machines-Application to the study of the harmonics influence on the heating of the asynchronous motors, Ph.D. Thesis, Nantes University, 2001.
- [12] R. Beguenane, M.E. Benbouzid, Induction motors thermal monitoring by means of rotor resistance identification, *IEEE Transactions on Energy Conversion* 14 (3) (1999) 566-570.
- [13] R. Beguenane, M.E.H. Benbouzid, Induction motors thermal monitoring by means of rotor resistance identification, in: IEEE International Conference on Electric Machines and Drives, Milwaukee, 1997.
- [14] L.S. Bin, T.G. Habetler, R.G. Harley, D.J. Gritter, A stator and rotor resistance estimation technique for conductor temperature monitoring, in: IEEE Industry Applications Conference, Rome, 2000.
- [15] M.S.N. Sadid, M.E.H. Benbouzid, H-G diagram based rotor parameters identification for induction motors thermal monitoring, *IEEE Transactions on Energy Conversion* 15 (1) (2000) 14-18.
- [16] M. Schöning, E. Lange, K. Hameyer, Development and validation of a fast thermal finite element solver, in: 18th International Conference on Electrical Machines, Vilamoura, Portugal, 2008.
- [17] D. Sarkar, P.K. Mukherjee, S.K. Sen, Use of 3-dimensional finite elements for computation of temperature distribution in the stator of an induction motor, in: IEE Proceedings B Electric Power Applications, 1991, pp. 75-86.
- [18] A. Boglietti, A. Cavagnino, D. Staton, M. Shanel, M. Mueller, C. Mejuto, Evolution and modern approaches for thermal analysis of electrical machines, *IEEE Transactions on Industrial Electronics* 56 (3) (2009) 871-882.
- [19] O.I. Okoro, Dynamic and Thermal Modeling of Induction Machines With Non Linear Effects, Kassel University Press GmbH, Kassel, 2002.
- [20] J.F. Moreno, F.P. Hidalgo, M.D. Martinez, Realisation of tests to determine the parameters of the thermal model of an induction machine, in: IEE Proceedings-Electric Power Applications, 2001, pp. 393-397.
- [21] J.K. Al-Tayie, P.P. Acarnley, Estimation of speed, stator temperature and rotor temperature in cage induction motor drive using the extended Kalman filter algorithm, in: IEE Proceedings-Electric Power Applications, 1997, pp. 301-309.
- [22] L.S. Bin, T.G. Habetler, R.G. Harley, D.J. Gritter, An evaluation of model-based stator resistance estimation for induction motor stator winding temperature monitoring, *IEEE Transactions on Energy Conversion* 17 (1) (2002) 7-15.
- [23] Z. Gao, Sensorless stator winding temperature estimation for induction machines, Ph.D. Dissertation, Georgia Institute of Technology, 2006.



Journal of Electrical Engineering

Volume 1, Number 1, December 2013

David Publishing Company

3592 Rosemead Blvd #220, Rosemead, CA 91770, USA

Tel: 1-323-984-7526, 323-410-1082; Fax: 1-323-984-7374, 323-908-0457

<http://www.davidpublishing.com>

electrical@davidpublishing.com, electrical@davidpublishing.org

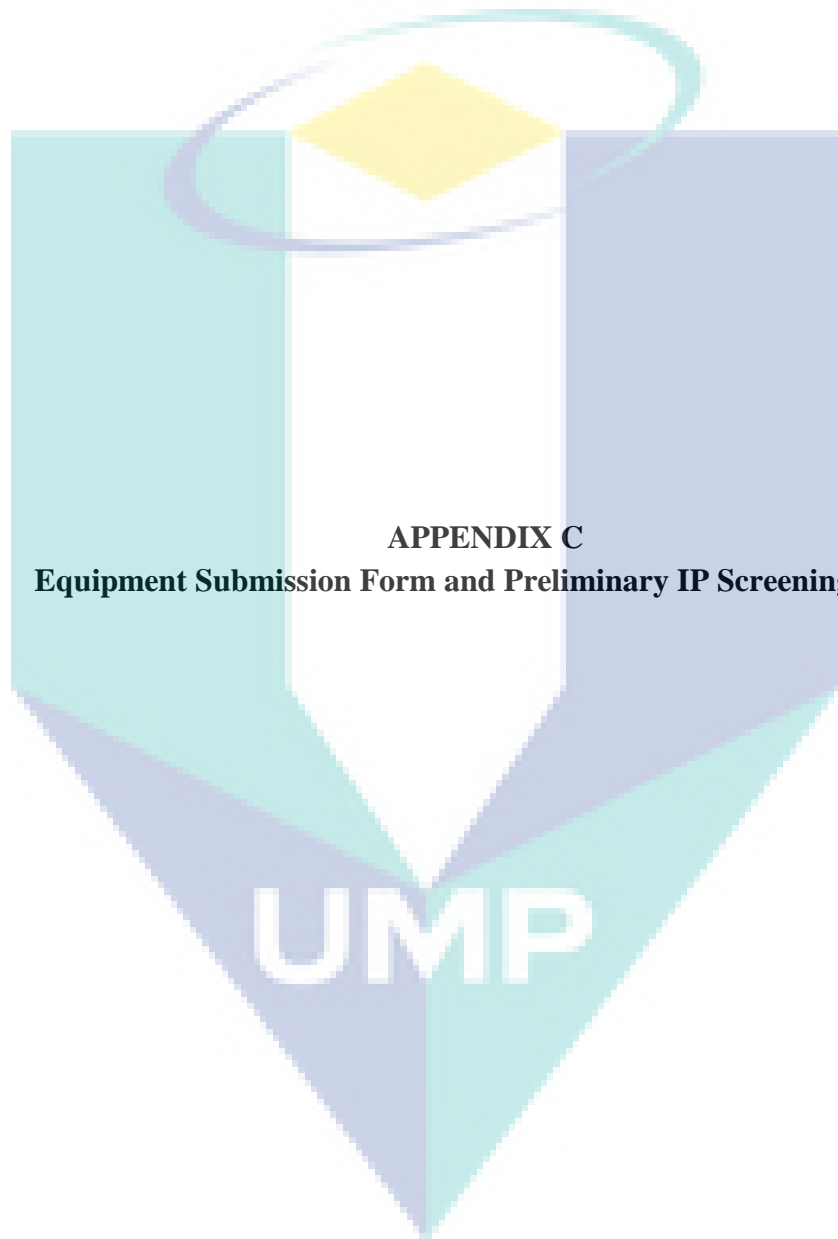
UMP

ISSN 2328-2223



9 772328 222136

12



APPENDIX C
Equipment Submission Form and Preliminary IP Screening Form